DEVELOPMENT OF FRINGE ANALYSIS TECHNIQUES IN WHITE LIGHT INTERFEROMETRY FOR MICRO-COMPONENT MEASUREMENT

LI MINGZHOU

NATIONAL UNIVERSITY OF SINGAPORE

2008

DEVELOPMENT OF FRINGE ANALYSIS TECHNIQUES IN WHITE LIGHT INTERFEROMETRY FOR MICRO-COMPONENT MEASUREMENT

BY

LI MINGZHOU

(M. Eng.)

A THESIS SUBMITTED

FOR THE DEGREE OF DOCTOR OF PHILOSOPHY

DEPARTMENT OF MECHANICAL ENGINEERING

NATIONAL UNIVERSITY OF SINGAPORE

2008

ACKNOWLEDGEMENTS

The author would like to thank his supervisors Assoc. Prof. Quan Chenggen and Assoc. Prof. Tay Cho Jui for their advice and guidance throughout the research. He would like to take the opportunity to express his appreciation for their constant support and encouragement which have ensured the completion of this work.

The author would like to express his sincere gratitude to Dr. Wang Shi Hua for his invaluable suggestions which have contributed greatly to the completion of this work.

Very special thanks to all research staff, visiting staff, lab officer and research scholar in Experimental Mechanics Laboratory. The crossbreeding of results and exchange of ideas in this group create a perfect research environment.

Finally, the author would like to thank his family for all their support.

TABLE OF CONTENTS

Acknowledgements i
Table of contents ii
Summary iv
List of tables vi
List of figures vii
Nomenclature xi

CHAPTER 1 INTRODUCTION **1**
1.1 Background 1
1.2 Objective of thesis 6
1.3 Scope of work 7
1.4 Thesis outline 7
CHAPTER 2 REVIEW OF RELEVANT WORK **9**
2.1 Optical techniques for 3-D measurement 9
2.1.1 Non-interferometric techniques 9
2.1.2 Interferometric techniques 12
2.2 White light interferometry 15
2.2.1 Applications of white light interferometry 15
2.2.2 Fringe analysis techniques 17
2.2.2.1. Maximum intensity of a recorded interferogram 20
2.2.2.2. Envelope peak detection 21
2.2.2.3. Spatial domain analysis 27
2.2.2.4. Phase-shifting technique 29
2.2.2.5. Direct quadratic polynomial fit 31
2.3 Wavelet applications in optical fringe analysis 34
2.4 Color fringe analysis in optical measurement 36
CHAPTER 3 DEVELOPMENT OF THEORY **39**

3.1 Vertical scanning white light interferometric measurement 39

3.1.1 Micro-cantilever inspections 43

3.1.2 Inspection of layered structures 45

3.2 Fringe analysis using continuous wavelet transform 47

3.2.1 Selection of mother wavelet 48

3.2.2 Data analysis in white light interferometric measurement 51

3.3 Color fringe analysis in white light interferometry 56

CHAPTER 4 EXPERIMENTATION AND SIMULATION 62

4.1 Experimental system 62

4.2 Software algorithms used for experiments 65

4.2.1 Image recording 65

4.2.2 Gray fringe analysis 66

4.3 Simulations on color fringe analysis 68

CHAPTER 5 RESULTS AND DISCUSSION 72

5.1 3-D surface profiling 72

5.2 Inspection of dual-layer structures 84

5.3 Micro-cantilever inspection 90

5.4 Surface quality evaluation 94

5.5 Measurement uncertainty analysis 99

5.6 Color fringe analysis 104

5.7 Discussion on time consumption of algorithms 107

CHAPTER 6 CONCLUSIONS AND RECOMMENDATIONS 110

6.1 Concluding remarks 110

6.2 Recommendations for future work 112

REFERENCE 113

APPENDICES 123

A. Imaging recording program by Microsoft Visual C++ 6.0 123

B. Subroutine of gray fringe processing 126

C. Subroutine of color fringe processing 129

D. Interferometry objective 133

E. List of publications 134

SUMMARY

White light interferometric technique is able to carry out accurate 3-D profile measurements of micro-components without phase ambiguity. In this thesis, different fringe analysis methods for white light interferometry were studied. Based on the discussion of current methods, new techniques based on continuous wavelet transform (CWT) as a signal processing tool are developed in this thesis.

A new algorithm based on CWT was developed for gray fringe analysis, and experiments using the developed vertical scanning white light interferometer were conducted for different micro-structures. These include the profiling of surface with step height, the investigation of dual-layer structures and the reconstruction of 3-D profile of obstructed surfaces. Compared with current methods, wavelet transform is able to analyze a single frequency component of a signal, thus decreasing the influence of various noises and hence significantly increasing the resolution of measurements. The results show that the new algorithm is able to improve the measurement accuracy and perform very well in noisy fringe analysis.

Another new algorithm based on color fringe analysis was also proposed in the thesis. Color fringe pattern is able to be decoded into three channels R, G and B. The three channels are used together to reconstruct the 3-D profile of a test sample. CWT was used as a data processing tool in the new technique for color fringe analysis. The phases of each color component are retrieved by CWT, and then the phase function in

terms of vertical scan position is constructed using a least square fit. A least square method is utilized to accurately determine where the optical path difference (OPD) becomes zero. In this method, a new technique based on absolute values of phase difference between different channels was developed to determine zero-order fringe. It is proven by simulations that the new algorithm is able to achieve very high accuracy, and hence is feasible for white light interferometric fringe analysis in micro and even nano-level applications.

In the study, a unique measurement system using white light interferometric technique was developed to verify the proposed algorithm. The system includes both hardware and control software. The hardware part is easily to be interchanged between two types of interferometers: Michelson and Mirau interferometers. A vertical scanning accuracy of 1 nm has been achieved using a PZT nano-positioning stage. The control software was developed using Microsoft Visual C++ 6.0.

It could be concluded that two new algorithms based on CWT for white light interference fringe analysis have been developed. One is for gray fringe analysis, which was proven by experiments to be a good approach for 3-D surface profiling. Another one is for color fringe analysis, the potential of which was verified by simulations, which could also be proved experimentally if necessary equipment was provided. Besides the new algorithms, several special applications, such as layered-structure inspection and hidden surface inspection, were also implemented with the developed measurement system in this study.

LIST OF TABLES

Table 4.1	Parameters of the illumination source in simulations	69
Table 5.1	Sources of alignment deviation and their contributions	75
Table 5.2	A summary of standard uncertainty components	103
Table A.1	Key parameters of interferometry objectives	133

LIST OF FIGURES

Figure 2.1	A typical fringe projection measurement system	10
Figure 2.2	(a) A typical one-dimensional laser interferogram (b) wrapped phases of the signal	13
Figure 2.3	Basic layout of a vertical scanning white light interferometer	18
Figure 2.4	(a) Intensity response of white light interferometry (b) cosinoidal signal (c) visibility function	19
Figure 2.5	(a) Recorded intensity (b) spectrum of Fourier transform (c) filtering out DC and negative frequencies and centralizing (d) extracted coherence envelope by inverse Fourier transform	23
Figure 3.1	Schematic diagram of a white light interferometer	39
Figure 3.2	Side view of a micro-cantilever structure	43
Figure 3.3	Model of underneath surface measurement	44
Figure 3.4	Schematic of a layered structure	46
Figure 3.5	A intensity response of a layered structure	46
Figure 3.6	Illustration of a continuous wavelet transform	49
Figure 3.7	Illustration of zero-order fringe peak determination	52
Figure 3.8	Wavelet transform scalogram of a white light interferometric signal	54
Figure 3.9	(a) A white light interferometric signal (b) coherence envelope defined by the ridge (c) phases on the ridge	55
Figure 3.10	Phases of channels R, G and B	58

Figure 3.11	Absolute values of phase differences between channels R and B and that between channels G and B	59
Figure 4.1	Schematic layout of the experimental system using Michelson interferometer	62
Figure 4.2	Schematic layout of the experimental system using Mirau interferometer	63
Figure 4.3	Actual experimental set-up for 3-D measurement	64
Figure 4.4	Flowchart of fringe pattern recording	66
Figure 4.5	Procedure of the fringe analysis using CWT	67
Figure 4.6	Algorithm structure for color fringe analysis	70
Figure 5.1	(a) Top view of standard step specimen A (b) top view of standard step specimen B	72
Figure 5.2	(a) A 3-D plot of a step height standard 1785.9 ± 3.8nm (b) a 3-D plot of a step height standard 23474 ± 14.1nm	73
Figure 5.3	(a) Misalignment (b) relative tilt of reference plane	74
Figure 5.4	A 2-D top view of a portion of a lamellar grating	76
Figure 5.5	A 3-D plot of a reconstructed lamellar grating	76
Figure 5.6	Comparison of cross-sections obtained by different methods	77
Figure 5.7	(a) A prescribed surface (b) reconstructed 3-D plot of the surface using CWT method (c) reconstructed 3-D plot of the surface using envelope method	79
Figure 5.8	Errors introduced by the algorithm	80
Figure 5.9	Comparison of errors due to different noise levels	81
Figure 5.10	Comparison of errors introduced by scanning increment	82
Figure 5.11	Phase error plot in terms of noise level	82

Figure 5.12 (a) A reconstructed micro-gear surface using CWT method (b) a reconstructed micro-gear surface using envelope method 83

Figure 5.13 White light interferometric fringe patterns of a micro-gear 84

Figure 5.14 (a) Intensity response of a point on a coated wafer (b) Wavelet transform spectrum of the intensity response 85

Figure 5.15 Optical thickness of a coating layer on a wafer 85

Figure 5.16 (a) 3-D plots of top surface of coating (b) interface between coating and substrate 86

Figure 5.17 A top view image of a transparent micro-gear 87

Figure 5.18 A transparent layer on an opaque substrate 87

Figure 5.19 Intensity response of a point on the micro-gear 88

Figure 5.20 (a) 3-D profile of a transparent micro-gear (b) the apparent thickness due to the refractive index 89

Figure 5.21 Top view of a micro-cantilever structure 90

Figure 5.22 Intensity response of a point on a micro-cantilever 91

Figure 5.23 A reconstructed 3-D top profile of micro-cantilevers 92

Figure 5.24 (a) 3-D underneath profile obtained by proposed system (b) 3-D underneath profile obtained by WYKO NT11001 93

Figure 5.25 A comparison of cross-sections of the underneath surface at 125 μm from the fixed end of the micro-cantilever 94

Figure 5.26 (a) A 3-D surface reconstructed by CWT (b) a 3-D surface reconstructed by envelope method 95

Figure 5.27 (a) A cross-section of the surface by CWT (b) a cross-section of the surface by envelope method 96

Figure 5.28 (a) A 3-D plot of a mirror surface using CWT (b) a 3-D plot of a mirror surface using envelope method 98

Figure 5.29	Cross-section of a standard mirror surface at y = 271.25 μm	99
Figure 5.30	Difference between the retrieved and prescribed phase values	101
Figure 5.31	(a) 3-D plot by proposed method (b) 3-D plot by gray fringe analysis (c) 3-D plot by phase-crossing method	105
Figure 5.32	Cross-section of reconstructed step profile	106
Figure 5.33	Influence of noise level on mean step height	106
Figure 5.34	Influence of noise level on standard deviation of surface variation	107

NOMENCLATURE

a	Scaling parameter in wavelet transform
b	Shift parameter in wavelet transform
c	Speed of wave front
$\hat{C}$	Estimated number
E	Complex form of superposed wave
E_o	Complex form of object wave
E_r	Complex form of reference wave
f_k	Approximated sampled values
h	Surface variation
I	Recorded fringe intensity
I_0	Background intensity
I_m	Modulation intensity
i	Vertical sampling order
j	$\sqrt{-1}$
k	Wave number
k_0	Mean wave number of a white light source
N	Total amount of vertical samplings
V	Visibility function
v	Wave frequency

v_0	Central frequency of a light source
z	Vertical scan position
Z	Optical path difference (OPD)
z_i	Discrete vertical scan position
λ	Wavelength of light source
λ_0	Mean wavelength of a white light source
λ_{eq}	Equivalent wavelength
φ	Phase
φ_0	Initial phase offset
$\Delta\varphi$	Phase-shift
Δ	Vertical scanning increment
τ	Time delay
*	Complex conjugate operator
$\mathrm{Im}[\ ]$	Imaginary part of a complex-valued argument
$\mathrm{Re}[\ ]$	Real part of a complex-valued argument
$\langle\ \rangle$	Time average operator

CHAPTER ONE

INTRODUCTION

1.1 Background

In recent years, Micro-electro-mechanical system (MEMS) has been developed rapidly and can be found in many applications. Consequently, the measurement of micro-components used in micro-electro-mechanical systems has become a popular research topic. Owing to the advantages of non-contact, high-resolution and high-accuracy, optical techniques have played and are still playing an important role in the micro-component measurements. Recently, the miniaturization of the micro-components used in MEMS has become a trend. It is important to know features, such as dimensions and surface quality in order to study the static and dynamic characteristics. Consequently, it is necessary to find a reliable method to measure three-dimensional (3-D) geometric dimensions and inspect their surface quality.

Stylus is normally used in profile measurements in engineering, but it is a contact method and it may scratch the surface of the test samples. Hence, laser probe was introduced in applications such as CNC machining (Shiou and Chen, 2003) and rapid prototyping (Shiou and Gao, 2003). An optical probe is not in contact with a sample, but it is a point-wise method resulting in low testing speed. In order to improve the testing speed, it is necessary to implement whole field measurement. Fringe projection technique (Sirnivasan et al, 1984) is a way to implement whole field optical

measurement. However, low resolution limits its application in miniaturized structures. Confocal technique (Sheppard and Wilson, 1981) based on lateral scanning was developed for measurements with high accuracy. Although non-scanning confocal technique (Tiziani and Uhde, 1994) was proposed, the micro-lens array used is complex and difficult to fabricate with high accuracy which is necessarily required in high-accuracy measurements using a micro-lens array. However, Laser probe, fringe projection and confocal microscopy are non-interferometric techniques. Optical interferometric techniques are able to be applied to whole field 3-D measurement with high resolution and accuracy, and hence they are more applicable to a micro-component at the level of micron or even nanometer.

Optical interferometry possesses the virtues of high resolution and accuracy at micro-level, or even nano-level, making optical interferometric techniques good for micro-component measurement. Monochromatic interferometry (Wyant and Creath, 1992) is a common technique mostly used in measurement, because monochromatic light is able to produce high quality fringe patterns, which can be easily recorded and processed. In monochromatic interferometric fringe processing using phase-shifting or Fourier transform technique, the phase is first calculated. However, all the calculated phases (wrapped phases) are between $-\pi$ and $+\pi$. In order to obtain the actual phases, which are directly related to the profile of the measured surface, a phase unwrapping technique is needed. However, if the phase difference between two adjacent points is larger than 2π, the actual phases cannot be extracted. Thus, classical monochromatic interferometry is not suitable for a rough surface and

sharp-step structures. This problem is regarded as a phase ambiguity problem, which is unavoidable in monochromatic interferometric measurements. Two-wavelength interferometric technique (Wyant, 1971) was an alternative way to overcome the problem of phase ambiguity. Therefore, it is possible to measure rough surface with this technique. Multiple-wavelength interferometric technique (Cheng and Wyant, 1985) and wave-length scanning interferometric technique (Suematsu and Takeda, 1991; Kuwamura and Yamaguchi, 1997; Tiziani et al, 1997) have also been introduced to resolve the problem of phase ambiguity. However, the equipment for the measurement system becomes more complicated, because a wavelength-tuning light source is needed to produce different wavelengths. White light interferometry was then implemented in 3-D profiling without phase ambiguity and complicated equipment. Due to its properties of being non-destructive, high resolution and accuracy, white light interferometric technique was widely applied to many measurements, such as machined steel surface (Caber, 1993), and end surface of an optical fiber (Quan et al, 2006).

White light interferometric technique can also be found in many other applications. Groot and Deck (1995) applied white light interferometric technique in the measurement of a bio-structure. In this application, a moth's eye was tested and its 3-D surface profile was plotted. Whereas, Windecker and Tiziani (1999) proposed a method based on white light interferometer to measure a machined surface in engineering, in which the roughness of a machined surface was obtained by analyzing white light interferometric fringe patterns, and then the surface quality was evaluated.

In order to enlarge the lateral measurement range, Olszak (2000) proposed a lateral scanning white light interferometer to obtain large field of view. Stitching technique was used in this application to get a whole field 3-D surface profile. A sample of lettering was measured using the proposed method, and the results showed that it was effective for large view measurements. White light interferometric technique was also widely used in the inspection of micro-mechanical structures. Among these applications, O'Mahony *et al* (2003) studied a micro-cantilever beam using white light interferometry. The above applications focus on retrieving characteristics on the top surfaces of samples, and few studies were done to investigate multiple-layer structures, in which both the top surface and interface between different layers are inspected.

In interferometric measurements, interferograms (fringe patterns) are firstly recorded by a charge-coupled device (CCD) and then the recorded fringe patterns are processed to obtain the features of interest. Thus, it is crucial to apply an appropriate algorithm to interferogram analysis for reliable and satisfactory results. One of the simplest algorithms (Balasubramanian, 1980) was to identify the maximum recorded intensity to determine the position of zero-order fringe, which indicates the height of a corresponding point on a tested surface. This method is fast and saves data storage, but it is sensitive to noise with low resolution and accuracy. Hence, coherence envelope extraction method was used to analyze white light interferograms. Chim (1992), Caber (1993) and Larkin (1996) respectively proposed several methods to retrieve coherence envelope from a white light interferogram. These kinds of methods

improved the measurement accuracy, but they are still sensitive to the noise which has frequency close to the mean frequency of a light source. Furthermore, Fourier transform is usually used to extract the envelope, but the result is highly dependant on filter window selection. Analysis of white light interferograms in spatial frequency domain was proposed by Groot and Leck (1997). This method uses the slope of a phase-frequency curve obtained by Fourier transform to determine the zero-order fringe position along a vertical scanning direction. However, it is still sensitive to the noise with frequencies close to the signal's frequency. Sandoz (1996, 1997) proposed a phase-shifting algorithm, which is normally used in monochromatic interferometry, for data processing of white light interferometry. The algorithm is able to obtain high resolution and high accuracy in phase calculation because it directly solves the interferometric functions to obtain theoretical solutions. However, if highly accurate result of a 3-D profile is required, the exact mean wavelength of the light source has to be known, which is difficult for some non-uniform surfaces. Recently, Park and Kim (2000) proposed a direct quadratic polynomial fitting algorithm, which is able to obtain high accuracy with relative simplicity. However, the exact mean wavelength of the light is still needed if an accurate 3-D profile is required. The above reviews have shown that the current methods are either sensitive to noise or highly dependent on the mean wavelength of an illumination source. Moreover, these algorithms were all developed for top surface profiling. So far, no methods satisfy the requirements for more accurate measurements, which are immune to noise and non-dependent on wavelength. Moreover, no algorithms have been developed for measurement of

layered structures.

1.2 Objective of thesis

The main task of the thesis is to develop new algorithms for fringe analysis in vertical scanning white light interferometric measurement. In current algorithms, Fourier transform is widely used for white light fringe analysis, which has a good performance in many applications. However, manual selection of Fourier transform filter will introduce uncertainty in final results. In addition, due to the bandwidth of filter window, noise close to the signal in frequency cannot be removed in the data processing. Phase-shifting technique is also introduced in white light fringe analysis based on an assumption that a fringe is locally linear, which itself would add error on the results. Furthermore, a precise mean wavelength of the lighting was also required for accurate results. As mentioned in the previous section, a newly-developed quadratic fitting algorithm also required a precise mean wavelength of the lighting. Hilbert transform was also employed in white light interference fringe analysis, in which a precise mean wavelength was required again to implement $\pi/2$ phase-shift for each scan step. However, it may not be easy to get a precise mean wavelength of the reflected light from a test surface which is adsorptive for light. As reviewed, the main drawbacks of current algorithms include error due to the noise close to the signal in frequency, uncertainty due to the manual selection of filter window, and error due to an imprecise mean wavelength. Therefore, the main objective of the thesis is to develop new algorithms, which is independent of the mean wavelength and is able to

eliminate the impact of noise with frequencies close to the signal’s frequency and the uncertainty due to the manual filter window selection in Fourier transform.

1.3 Scope of work

The main objective of the study is to investigate new measurement techniques in the evaluation of micro-components using vertical scanning white light interferometry and to develop appropriate algorithms for analysis of resulting interferograms. This study includes development of a unique measurement system using vertical scanning white light interferometry, which is easily able to be transformed between Michelson and Mirau interferometers in order to adapt to different applications. This thesis investigates top surface profiling as well as inspections of layered and obstructed structures at micron and sub-micron levels. CWT is applied in the analysis of the gray fringe patterns for denoising and mean wavelength self-calibration. This study also includes analysis of color fringe patterns using CWT to provide more accurate and satisfactory results.

1.4 Thesis outline

The thesis is organized into six chapters. This section outlines the thesis.

Chapter 1 provides an introduction of this thesis.

Chapter 2 reviews related works in three parts. Firstly, optical techniques for 3-D measurement are reviewed, which include non-interferometric and interferometric techniques. The second part provides a literature survey of vertical scanning white

light interferometry: its applications and fringe analysis techniques. Finally, current applications of wavelet transform and color fringe analyses in optical measurement are reviewed.

Chapter 3 focuses on theory. The concept of vertical scanning white light interferometric measurement is discussed and then the inspections of obstructed surface and multi-layer structure using vertical scanning white light interferometry are investigated. Fringe analysis using CWT is introduced. Selection of mother wavelet, sampling peak identification and phase retrieval are then discussed. This chapter also describes determination of zero-OPD position using sampling peak and its phase. Color fringe analysis for vertical scanning white light interferometry is also discussed in this chapter.

Chapter 4 describes the development of the experimentation. Simulation procedure of color fringe analysis is also described in this chapter.

Chapter 5 presents results of different applications of vertical scanning white light interferometric technique. The applications include sharp-step surface profiling, dual-layer structure inspection, detection of obstructed surface, and surface quality inspection. Measurement uncertainty is also included. Finally, simulated results of color fringe analysis are discussed.

Chapter 6 summarizes the project and future research directions are recommended.

CHAPTER TWO
REVIEW OF RELEVANT WORK

2.1 Optical techniques for 3-D measurement

Due to the advantages of non-contact, high resolution and accuracy, optical techniques are used for 3-D surface profiling in both research and industry. This section provides a review of optical techniques in 3-D measurement.

2.1.1 Non-interferometric techniques

A simple way to retrieve 3-D shape of an object is to replace a contact stylus with an optical beam to scan the object surface (Kakino et al, 1997). In optical stylus profiling, point laser triangulation (Ji and Leu, 1989) was used to obtain the 3-D shape. Defocus of a laser beam (Mignot and Gorecki, 1983) caused by variation of an object surface, was also used to retrieve 3-D shape of an object. In order to increase the speed of measurement, a knife edge lighting (Fukatsu and Yanagi, 2005) was used to scan the surface of interest in one direction to obtain the 3-D profile.

To improve measurement speed and simplify complex scanning mechanism, a whole field measurement technique was required. Consequently, fringe projection technique (Chen et al, 2000), which now is very popular in 3-D surface profiling, was introduced. A typical fringe projection measurement system, which normally consists of a projection unit and an imaging unit, is shown in Fig. 2.1. The projection unit projects a predefined fringe pattern on an object and an imaging unit records the

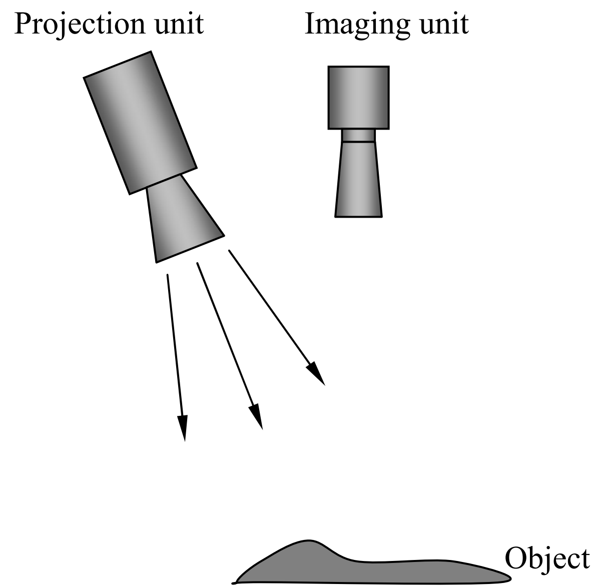

Fig. 2.1 A typical fringe projection measurement system

fringe pattern, which is deformed due to variation of the object surface. Traditionally, a fringe pattern is normally generated by shining a physical grating, which produces square (Takeda and Mutoh, 1983) or sinusoidal pattern (Li et al, 1990). The development of digital devices (Sitnik et al, 2002) provides fringe projection technique more flexibility than physical gratings. Fang and Zheng (1997) used sawtooth-like fringe pattern on an object for surface profiling. Sjödahl and Synnergren (1999) used random pattern in 3-D surface fringe projection. A digital LCD projector may also reduce errors caused by physical gratings.

The principle of triangulation is applied in data processing in fringe projection measurement. Based on the principle of triangulation, the surface profile is able to be determined by a relationship between surface height and phase of the deformed fringe pattern. Fourier transform analysis (Quan et al, 1995) and phase-shifting technique

(Quan et al, 2001) are two traditional ways to map the phase distribution. Fourier transform can be applied to one fringe pattern to filter out unwanted frequencies and obtain phases due to the surface shape, while phase-shifting technique directly calculates the phases using several fringe patterns. Recently, new data processing methods were also proposed. Temporal digital speckle photography was used in data processing of fringe projection measurement (Sjödahl and Synnergren 1999). Quan et al (2004) applied digital correlation to fringe projection for 3-D deformation measurement. Color image processing was also applied to fringe projection measurement using color-encoded fringes to improve the measurement speed (Huang et al, 1999; 2003).

Although fringe projection measurement is relatively simple and easy to implement, its accuracy is difficult to match the sub-micron requirement in many applications. Confocal technique (Wilson and Sheppard, 1984) is another non-interferometric way for the measurement with high accuracy. In confocal 3-D measurement, an optical beam is focused on an object and intensity is recorded. During scanning along optical axis, the maximum intensity is recorded when a beam is focused on an object surface and a 3-D profile can be obtained by scanning the object. Normally, the confocal technique requires 3-D scanning for 3-D surface profiling (Massig et al, 1994). Thus, the measurement speed is slow though with high resolution. Micro-lens and pinhole arrays (Fujita et al, 2000) reduced 3-D scanning to one-directional scanning and hence reduced much measurement time.

2.1.2 Interferometric techniques

Optical interferometry, which possesses the merits of high resolution and accuracy, has been widely applied to 3-D shape measurement. Laser (Viswanathan et al, 1980) is generally utilized as an illumination source. Figure 2.2 (a) shows a one-dimensional laser interferogram. The intensity recorded is generally expressed as

$$I = I_0 + I_m \cos\varphi \tag{2.1}$$

where I_0 and I_m are the background and the modulation intensity respectively. φ is a random phase. The surface profile of an object is determined by the phase recorded. In reflective interferometric measurement, the surface variation h is given by

$$h = \frac{\varphi}{4\pi}\lambda \tag{2.2}$$

where λ is the wavelength of a light source.

Data processing of laser interferometry is to retrieve the phase values of interferograms and to calculate the surface profiles or deformations. Among the different methods, Fourier transform (Takeda et al, 1982) and phase-shifting technique (Creath, 1985) are generally used for phase extraction. But the extracted phases are usually wrapped within $-\pi$ to π with sudden jumps as shown in Fig. 2.2 (b). In order to reconstruct a correct 3-D shape of the object, phase unwrapping

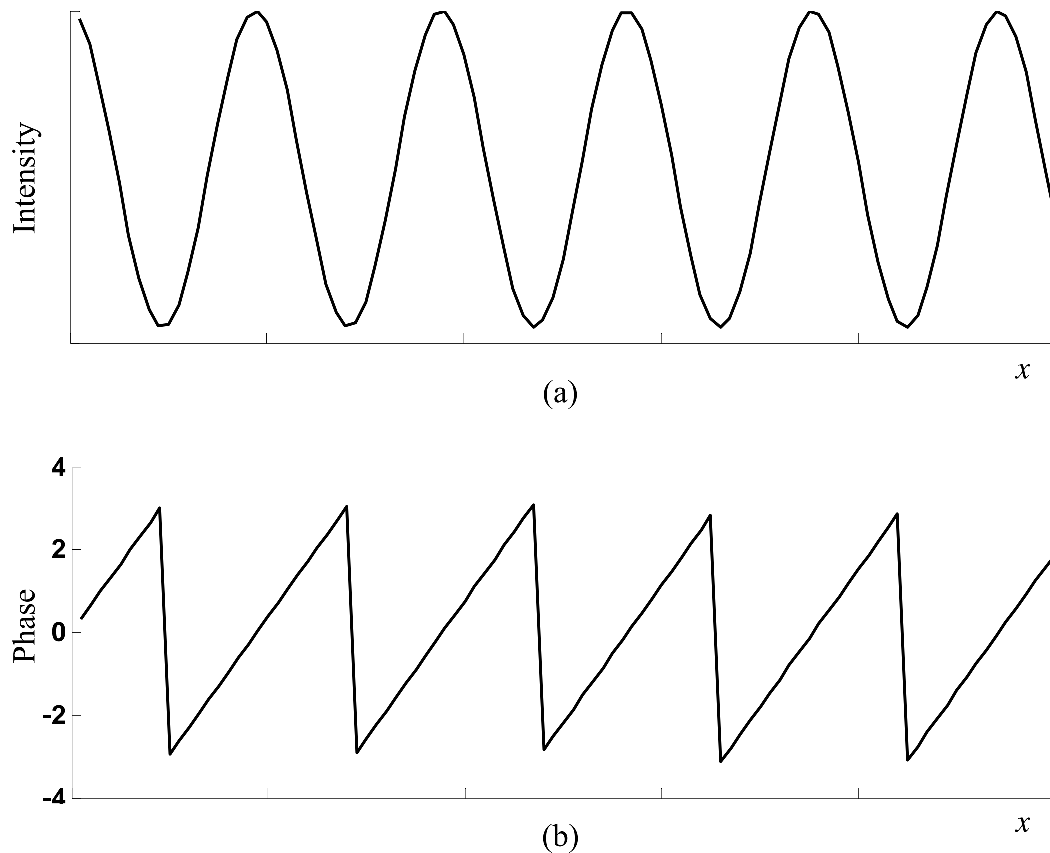

Fig. 2.2 (a) A typical one-dimensional laser interferogram;
(b) wrapped phases of the signal

(Malacara et al, 1998) is needed to obtain a continuous phase map. However, if the phase difference between two adjacent point is more than 2π ($\lambda/2$), a correct phase map still cannot be plotted even with phase unwrapping techniques. This is a common problem of phase ambiguity encountered in monochromatic interferometry.

Phase ambiguity limits the range of measurement using monochromatic interferometric techniques. Thus, two-wavelength interferometry (Polhemus, 1973) was introduced to extend the measurement range in 3-D measurement. Two light sources with wavelength of λ_1 and λ_2 were used in the method. An equivalent wavelength of the measurement system is expressed as (Cheng and Wyant, 1984)

$$\lambda_{eq} = \frac{\lambda_1 \lambda_2}{\lambda_1 - \lambda_2} \tag{2.3}$$

So, the system could be considered as a monochromatic interferometry with a single-wavelength of λ_{eq}. Thus, the measurement range was extended to $\lambda_{eq}/2$ from $\lambda/2$. The closer the two wavelengths are, the larger the measurement range of a two-wavelength interferometric instrument is.

To improve the performance for high frequency structures, a third wavelength was included in the measurement system leading to multi-wavelength interferometry (Cheng and Wyant, 1985). In fact, further corrections could be applied if one has more phase data from other wavelengths. Wavelength-shifting/scanning interferometry is possible with a wavelength-tunable laser diode. Fourier transform is commonly used to extract phases of interferograms. One way to obtain surface profile is based on phase change in terms of wavelength (Kuwamura and Yamaguchi, 1997; Tiziani et al, 1997). Yamamoto and Yamaguchi (2002) also derived surface height from a peak position of Fourier transform of the interference signals arising from wavelength scanning of a dye laser at each point of a surface. Wavelength-scanning interferometry was also applied to displacement measurement by Ruiz et al (2004). Wavelength-scanning interferometry was combined with confocal microscope for layered structure measurement by Watanabe and Yamaguchi (2002). Following wavelength-scanning interferometry, white light interferometry was introduced for 3-D measurement.

2.2 White light interferometry

This section reviews applications of vertical scanning white light interferometric technique. Current data processing methods are also reviewed.

2.2.1 Applications of white light interferometry

Vertical scanning white light interferometry has been widely used for surface profile measurement without problem of phase ambiguity. White light interferometric measurement has come a long way since Hooke observed in 1665 that colors in white light interference pattern are sensitive to the thicknesses between reflecting surfaces. White light interferometry has also been used in many optical instruments for gauge block calibration. Although the basic principles of white light interferometry are fundamental concepts of optics and has been studied for a long time, 3-D measurement using vertical scanning white light interferometry appeared in recent times. One of the first practical white light interferometric systems for automated 3-D surface profile topography was proposed by Balasubramanian (1982). In the system, the relative height of each point on a surface was obtained by a scanning position on an interferogram where its contrast reached a maximum. Davidson (1987) used white light interferometric technique to measure the profile of micro-components such as integrated circuits by detecting the peak contrast of a fringe pattern. Lee and Strand (1990) had also proved that lateral resolution could be improved with white light interferometry when compared to conventional microscope in 3-D topography, which

broaden the application of white light interferometry. Deck and Groot (1994) proposed a high-speed profiler based on vertical scanning white light interferometry to map a 3-D structure of a 921-nm-high grating. R. Windecher and H. J. Tiziani (1999) measured the optical roughness of engineering surface by the use of extended white light interferometry. White light interferometry has also been extended with enlarged field of view using changeable tube lens (Windecher et al, 1999), with which the 3-D topography of a diamond-turned aluminum surface consisting of micro-mirrors was plotted. Olszak (2000) also proposed an alternative technique to extend the field of view for large objects. In the technique, the sample was scanned laterally with a tilted coherence plane, so that vertical and lateral scanning was synchronized. In this case, vertical scanning locates points on a surface, and lateral scanning extends the field of view of the interferometer.

In recent years, vertical scanning white light interferometry found itself being used in more applications. Groot and Lega (2003) applied vertical scanning white light interferometry to measurement of valve cone angle, roundness, straightness and waviness. Olszak and Schmit (2003) improved the accuracy and stability of white light interferometer by embedding an additional high-coherence interferometer into the system, in which short-term repeatability reaches 30 nm and long-term repeatability reaches 3 nm. Micro-cantilevers were also characterized using white light interferometry by O’Mahony et al in 2003. Montgometry et al (2004) used white light interferometry to map the 3-D profile of a FT spectrometer used in micro-optical electro-mechanical systems (MOEMS). Another application in micro-structures could

be found in a paper by Bosseboeuf and Petitgrand (2006) where the 3-D profile of a micro-accelerator was measured. In addition, Tooling characterization and qualification was carried out using white light interferometry (Vallance et al, 2004; Dawson and Kurfess, 2005). White light interferometry was also used in micro-lens fabrication to characterize focal length, surface roughness and optical aberrations (Moench and Zappe, 2004). White light interferometry has also been applied to biological and medical science recently and chondrocyte geometry was obtained by vertical white light interferometric scanning (Scott et al, 2004). In 2005, Hissmann and Hamprecht proposed Bayesian surface estimation based on white light interferometric measurement to retrieve the 3-D profile of a multi-step steel object. In the same year, Djinovic et al combined fiber-optics with white light interferometer to implement nano-scale measurement of wear rate and vibration of a pin in a standard pin-on-disc tribometer. In 2006, Poilâne introduced a double-sided white light interferometry to measure the thickness of non-transparent free films in which two white light interferometer were arrange on both sides of a film along an optical axis. Quan et al (2006) used white light interferometer for multifiber-end surface profiling. Recently, vertical scanning white light interferometry was also applied to characterizing membrane surface topography (Koyuncu et al, 2006).

2.2.2 Fringe analysis techniques

Figure 2.3 shows the basic layout of a vertical scanning white light interferometer. As an object is scanned vertically, the imaging unit record interference patterns for each

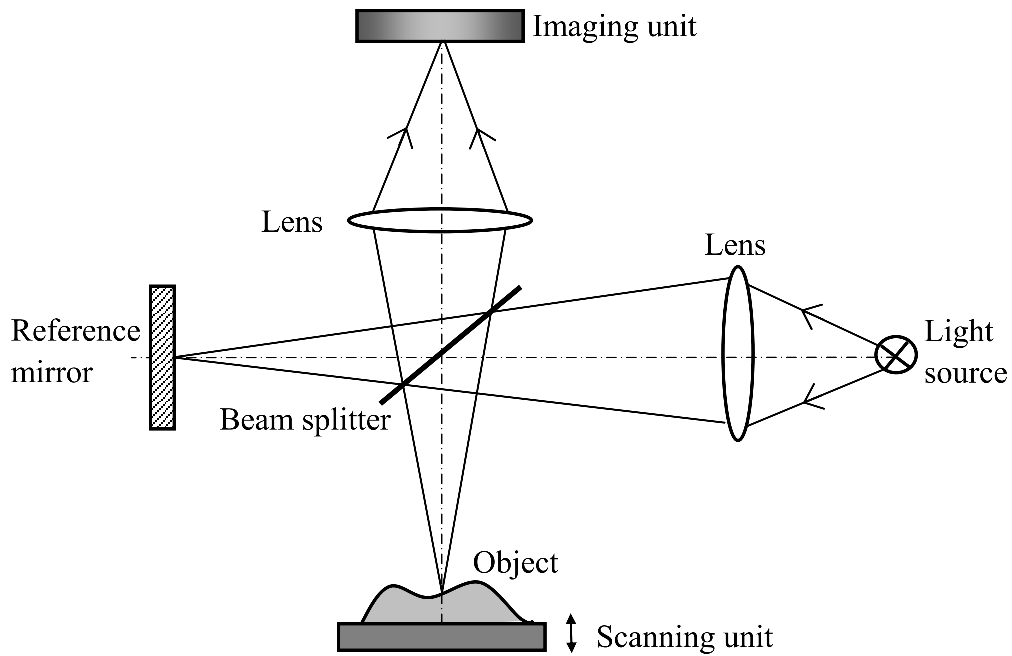

Fig. 2.3 Basic layout of a vertical scanning white light interferometer

scanning position. The recorded intensity response in the scanning direction of a point on the object surface is shown in Fig. 2.4 (a). This signal can be consider as a cosinoidal signal as shown in Fig. 2.4 (b) modulated by a visibility function given in Fig. 2.4 (c). Thus, the intensity response signal can be expressed as

$$I = I_0 + I_0 V \cos\varphi \tag{2.4}$$

where V is the visibility function, which is also called coherence envelope function and indicates the fringe contrast.

The fringe analysis process locates the peak position of the visibility functions in the scanning direction, which indicates the height of a point on the object surface. In previous studies, several methods to retrieve the visibility peak has been developed

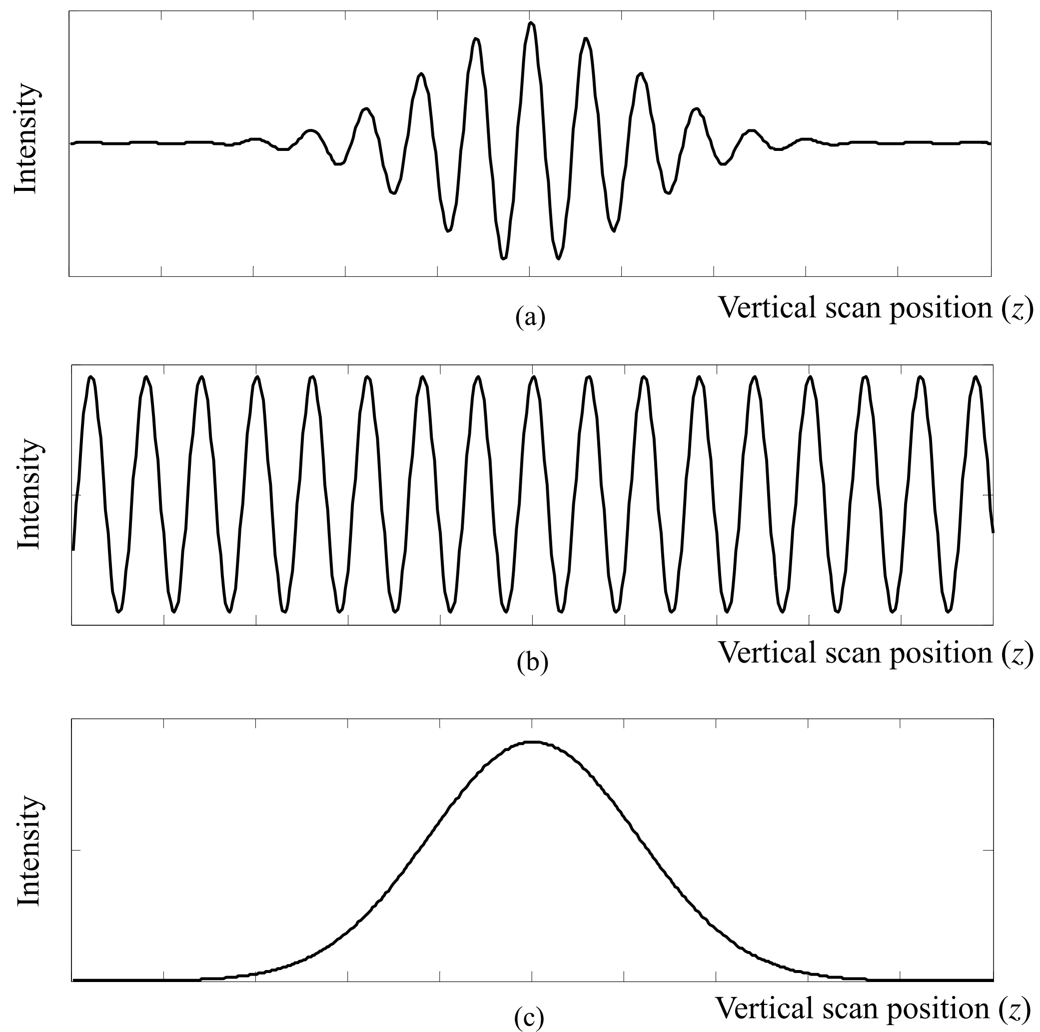

Fig. 2.4 (a) Intensity response of white light interferometry;
(b) cosinoidal signal; (c) visibility function

and improved. One simple way is to directly detect the maximum intensity with the assumption that the maximum intensity is recorded when the visibility reaches its maximum (Balasubramanian, 1982). Caber (1993) applied digital signal processing (DSP) algorithms to retrieve the envelope of the temporal intensity response. The high-speed measurement was obtained by implementing an algorithm in a high-speed DSP computer. Groot and Deck (1993) determined the phase-velocity OPD using the slope of the phase in terms of spatial frequency in a Fourier transform. Phase-shifting

techniques were employed for fringe analysis in 1995 by Hariharan and Roy, while Sandoz et al proposed a method based on a seven-step phase-shifting (1996; 1997). Phase-shifting in white light interferometry was also studied by Roy et al (2002). Hilbert transform was also used to extract the envelope of a white light interferometric temporal signal (Larkin, 1996). Park and Kim (2000) proposed direct quadratic polynomial fitting to detect the fringe peak with an assumption that the visibility variation near the maximum follows a quadratic polynomial function. In a recent study, a new method for fringe order determination was proposed to compensate for aberrations, distortion and dispersion that would otherwise lead to incorrect fringe order (Groot et al, 2002). In 2002, Hirabayashi et al developed a new algorithm based on a sampling theory for fast profiling using white light interferometry. In 2005, Hissmann and Hamprecht introduced a new method called Bayesian surface estimation.

2.2.2.1 Maximum intensity of a recorded interferogram

A method to obtain the position of maximum fringe contrast is to locate its maximum intensity (Balasubramanian, 1982; Bowe and Toal, 1996). The scanning position where the maximum visibility occurs is a measure of the relative height of a point on a surface. This method needs less storage space than other current popular methods for white light interferogram processing. Hence, it is suitable when high-speed or real-time measurement is required or a large digital storage device is not available. In this method, for each surface point only four buffers, B_1, B_2, B_3 and B_4, are required to

store the recorded intensities and scan positions during the measurement. The intensities of each point can be written as I_1, $I_{2\ldots}$ I_N. The values of B_1 and B_3 are first set as I_1, and the values of B_2 and B_4 are set as 1. The following operation is then carried out

If $B_1 < I_j$ $B_1 \leftarrow I_j$, $B_2 \leftarrow j$

Else $B_3 > I_j$ $B_3 \leftarrow I_j$, $B_4 \leftarrow j$ $j = 2,3,\ldots,N$

In this manner, the maximum value of a recorded white light interferogram can be obtained. This represents the relative height of the corresponding point on the measured surface. For example, if a maximum value is obtained at the jth scan, the height h of the point relative to a reference plane would be given by

$$h = j\Delta \tag{2.5}$$

where Δ is the vertical scanning increment. It is obvious that this method is simple and needs less data storage during measurement. However, it has its inherent shortcomings as the resolution in this case is limited to the step increment. For higher resolution and accuracy, the scanning increment should be decreased. However, as the scanning increment decreases, the effect of noise on the measurement results would increase dramatically as the recoded intensity difference between two adjacent scans reduces to that close to the noise level.

2.2.2.2 Envelope peak detection

Large digital storage devices and high speed computation make it possible to record large image data and digital filtering can be used to retrieve the coherence envelope. Since the intensity response is a cosinoidal signal modulated by a low frequency signal, the DC components of the signal can be easily removed and Eq. (2.4) is rewritten as follow

$$I = I_0 V(z)\cos\varphi \tag{2.6}$$

Squaring Eq. (2.6), resulting in

$$I^2(z) = \frac{I_0^{\ 2} V^2(z)}{2} + \frac{I_0^{\ 2} V^2(z)}{2}\cos(2\varphi) \tag{2.7}$$

where z indicates a vertical scan position. The visibility function is a low frequency signal. Thus, the high and low frequency parts are separated in Eq. (2.7) and the low frequency part, a coherence envelope of the signal, can be easily retrieved using a low-pass filter.

Fourier transform is a method used to filter out the high frequency part to obtain the coherence envelope (Kino and Chim, 1990). A procedure with Fourier transform to retrieve coherence envelope is described in Fig. 2.5. Fourier transform is applied to a signal in vertical scanning white light interferometric measurement shown in Fig. 2.5(a). The spectrum of Fourier transformed signal is shown in Fig. 2.5(b). The DC and negative frequencies are meaningless for the 3-D surface profiling and hence are

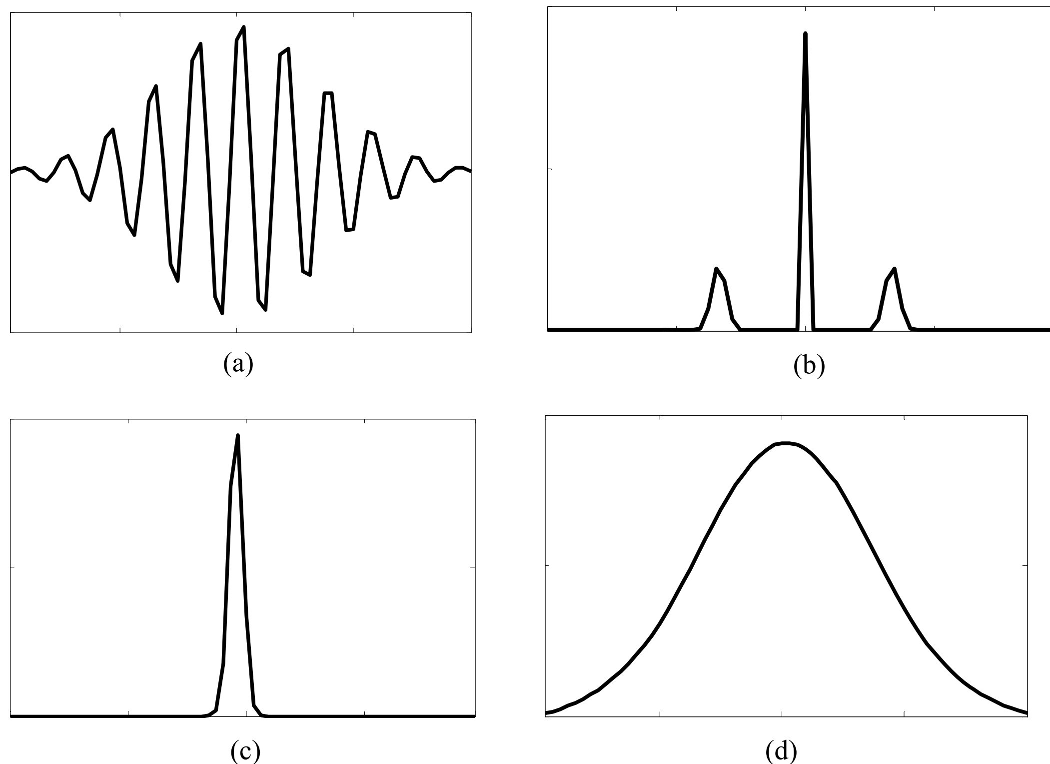

Fig. 2.5 (a) Recorded intensity; (b) spectrum of Fourier transform; (c) filtering out DC and negative frequencies and centralizing; (d) extracted coherence envelope by inverse Fourier transform

removed using a filtering window. Then, the spectrum is centralized as shown in Fig. 2.5 (c). The absolute values of the inversed Fourier transformed signal gives the coherence envelope shown in Fig. 2.5(d). To achieve accurate results, an interpolation is consequently applied to the extracted envelope to calculate the peak position. Because of the large number of image data to be processed and the nature of the computations involved, Caber (1993) implemented DSP in high-speed DSP hardware to reduce the calculation time and thus improve the measurement speed. However, because a filter window is manually selected in Fourier transform, more uncertainty will be introduced to the results. Moreover, due to the bandwidth of filter window, the noise with the frequencies close to the signal’s frequency will has much impact on the

results.

Hilbert transform was also introduced in digital filtering for extracting the coherence envelope (Chim and Kino, 1992). Larkin (1996) derived a nonlinear algorithm for envelope extraction based on the Hilbert transform. In Larkin's method, the value on the envelope for one sampling position is calculated from the recorded intensities of five sampling positions, the local position and four neighboring sampling positions. The calculated envelope is given by

$$V_i = \frac{1}{4}[4(I_{i-1} - I_{i+1})^2 - (2I_i - I_{i-2} - I_{i+2})^2]^{1/2} \qquad i = 3,4,...,N-2 \tag{2.8}$$

where i is the sampling order, and N is the total amount of samplings along the vertical scanning direction. For compensating errors, Eq. (2.8) is modified as

$$V_i = \frac{(I_{i-1} - I_{i+1})^2 \{[4(I_{i-1} - I_{i+1})^2 - (I_{i-2} - I_{i+2})^2] + (2I_i - I_{i-2} - I_{i+2})^2\}^{1/2}}{4(I_{i-1} - I_{i+1})^2 - (I_{i-2} - I_{i+2})^2} \tag{2.9}$$

Although Eq. (2.9) can provide a more precise envelope, there is a problem in practice that if the denominator is equal to zero, the program for data processing will be terminated. A simplification of Eq. (2.9) was thus proposed by Larkin (1996)

$$4V_i^2 \sin^4 \Delta\varphi = (I_{i-1} - I_{i+1})^2 - (I_{i-2} - I_i)(I_i - I_{i+2}) \tag{2.10}$$

where $\Delta\varphi$ is the phase-shift due to each scanning step. If $\Delta\varphi$ is close to $\pi/2$, Eq.

(2.10) can be rewritten as

$$V_i^2 = \frac{1}{4}[(I_{i-1} - I_{i+1})^2 - (I_{i-2} - I_i)(I_i - I_{i+2})] \tag{2.11}$$

V_i can be calculated with two multiplication and one square-root operations. However, in white light interferogram processing V_i^2 may be a negative number, and hence the envelope value would be a complex number. Therefore, in practical calculation program, a square operation is first applied to V_i^2, and then V_i is calculated by two square-root operations. Once an envelope is obtained, the peak position is located by applying a weighted least square fitting algorithm to the extracted coherence envelope. As reviewed, this algorithm requires a $\pi/2$ phase-shift for each scan step for accurate measurement, which is however not easy to obtain because the mean wavelength of the reflected light from a test object may be different for different material surfaces. Hence, a method independent of the mean wavelength is necessary to handle different kinds of test objects.

Another fast algorithm to retrieve coherence envelope was presented based on sampling theory by Hirabayashi et al (2002). In this method, an approximation was applied to the recorded intensities and the approximated values was given by

$$f_i = I(z_i) - \hat{C} \tag{2.12}$$

where z_i indicates the discrete vertical scanning positions and $\hat{C}$ is an estimated

number, which was defined as

$$\hat{C} = \frac{1}{N}\sum_{i=0}^{N-1} I(z_i) \tag{2.13}$$

Finally, the squared-envelope function was approximated by the following function:

$$V^2(z_i) = f_i^2 + \frac{4}{\pi^2}\left[\sum_{m=-(i+1)/2}^{(N-i-2)/2} \frac{f_i + 2m + 1}{2m + 1}\right]^2 \tag{2.14}$$

In order to get the surface height, the following steps to be carried out are the same as the previous methods.

Besides the interpolation operation, the phase values were also used to estimate accurate surface height *h* by the relation with phase-shift as

$$h \propto \lambda_0 (\Delta\varphi) \tag{2.15}$$

where λ_0 is the mean wavelength of a light source, which should be known to calculate the surface variation by this method. The phases can be easily calculated by Fourier transform. Since Fourier transform is also employed in this method, its drawbacks in white light interference fringe analysis discussed before also exist in this algorithm. In addition, this method is still dependent on an accurate mean wavelength of the light source, which may be different for different test objects.

2.2.2.3 Spatial domain Analysis

In 1990s, the concept of analyzing white light interferogram in spatial frequency domain was introduced by Groot et al (1993; 1995). White light interferogram can be regarded as an incoherent superposition of consecutive single-frequency interference patterns. Each of these single-frequency interference patterns can be defined by the following function (Groot and Deck, 1993)

$$I = 1 + \cos\varphi \tag{2.16}$$

where

$$\varphi = kZ \tag{2.17}$$

where $k = 2\pi / \lambda$ is a wave number and Z is the OPD, which indicates the surface height. Theoretically, from Eq. (2.17) it is clear that the OPD is given by

$$Z = d\varphi / dk \tag{2.18}$$

Therefore, one way to measure the height of a test surface is to calculate the rate of phase change in terms of spatial frequency. To calculate the phase slope with a wave number, we need the phase values over a range Δk of wave numbers centralized around a mean wave number k_0. The phase for each frequency component can be

extracted by Fourier transform. The transformed recorded white light interferogram is given by the following formula

$$P(k) = \int_{-\infty}^{\infty} I(z) \exp(-jkz) dz \tag{2.19}$$

The phase shift due to the OPD for each frequency, or wave number component, is give by

$$\varphi(k) = \tan^{-1}\left(\frac{\mathrm{Im}[P(k)]}{\mathrm{Re}[P(k)]}\right) \tag{2.20}$$

where $\mathrm{Im}[\ ]$ and $\mathrm{Re}[\ ]$ respectively refer to imaginary and real part of a complex number. The phases calculated from Eq. (2.20) are all wrapped within $-\pi$ and π, and hence phase unwrapping technique is used to obtain the real phase information for each frequency component. After data pairs (φ, k) are obtained from Fourier transform, a polynomial is fitted by linear least-square fitting technique to estimate the phase slope. Consequently, the height of a test surface can be determined from the change of phase over wave number $d\varphi / dk$. With this method of extracting OPD, if there is noise whose frequency is close to the central frequency of the interferogram, an error of the phase will be introduced, because the Fourier transform window is a frequency band. In addition, the manual selection of filter window in Fourier transform will add unnecessary uncertainty to the results.

2.2.2.4 Phase-shifting technique

Phase-shifting algorithms are widely used in data analysis for normal monochromatic interferometry (Wang et al, 2004). Since the fringe contrast of white light interferogram is not uniform, the normal phase-shifting algorithms cannot be directly applied to the analysis of a white light interferogram. Based on the concept of phase-shifting, Sandoz et al (1996; 1997) proposed a seven-point phase-shifting algorithm for the analysis of a white light interferogram. Based on the assumption that the coherence envelope of a white light interferogram is locally linear, Sandoz transformed the well-known four-point phase-shifting algorithm into a seven-point algorithm with weighted sampling intensities for white light interference fringe analysis. The phase-shift due to the OPD is approximately given by the following equation.

$$\varphi = \tan^{-1}\left(\frac{3I_{-1} + I_3 - I_{-3} - 3I_1}{4I_0 - 2I_{-2} - 2I_2}\right) \quad (2.21)$$

where I_i (i=-3,…,3) are recorded intensities corresponding to a relative phase-shift of $i\pi / 2$ due to vertical scanning. The phase-shift φ is a phase shift from the center of a zero-order fringe to a sampling position where intensity I_0 is recorded. I_0 is the intensity at a sampling position in which the fringe contrast of a recorded interferogram reaches its maximum value. Thus, the absolute phase value is given by

$$\varphi_a = \frac{m\pi}{2} - \varphi \tag{2.22}$$

where m is a sampling order, which corresponds to a recorded intensity I_0, from a reference plane. Eq. (2.22) is correct if I_0 is recorded within the theoretical zero-order fringe. However, in most situations, I_0 is not recorded within zero-order fringe. Therefore, to determine the fringe order of the central intensity I_0 is necessary. Sandoz et al (1997) proposed a method to identify the fringe order of the central intensity m'. After the fringe order is determined, the corrected absolute phase is given by

$$\varphi_a = \frac{m\pi}{2} - \varphi - 2m'\pi \tag{2.23}$$

The height of a corresponding surface point will be given by

$$h = \frac{\varphi_a}{4\pi}\lambda_0 \tag{2.24}$$

where λ_0 is the mean wavelength of a white light source.

Sandoz's method has its inherent problems in actual application. The assumption of local linearity of coherence envelope will introduce errors in the final calculated results. The seven-point algorithm is applied to the area around the position of maximum fringe contrast of the recorded intensities. This will lead to a bigger error in the approximation. Secondly, since phase-shifting algorithm is applied, the vertical

scanning step of $\pi/2$ should be accurate enough to implement precise measurement. Thus, the exact mean wavelength of the light source should be known. However, if the measured surfaces absorb some frequency components, the mean wavelength will be changed. From Eq. (2.24), it is clear that the height could not be obtained accurately if the mean wavelength of the light source was not determined precisely.

2.2.2.5 Direct quadratic polynomial fit

This algorithm was developed by Park and Kim (2000). In the method, the fringe contrast peak is determined by a direct quadratic polynomial fit based on a recorded temporal intensity response. For each surface point, the intensity response is given by (Born and Wolf, 1980)

$$I(z) = I_0 + I_0 g(h-z)\cos[2k_0(h-z)+\varphi_0] \tag{2.25}$$

where I_0 is background intensity, $g(h-z)$ is a coherence envelope, z is a vertical scanning position, h is surface variation relative to reference plane, k_0 is a mean wave number, and φ_0 the a initial phase offset. In Park and Kim's algorithm, the coherence envelope is approximated by a simple quadratic polynomial and the intensity of the white light interferogram is approximated by

$$I(z) = I_0 + I_0(a_1 + a_2 z + a_3 z^2)\cos[2k_0(h-z)+\varphi_0] \tag{2.26}$$

where a_1, a_2, and a_3 are the coefficients of the approximated coherence envelope function which determine the envelope peak by $h = -a_2 / 2a_3$. The least-square fitting is carried on Eq. (2.26). In order to implement linear least-square fitting, the following vector is defined.

$$
\begin{aligned}
C &= [c_1 \quad c_2 \quad c_3 \quad c_4 \quad c_5 \quad c_6 \quad c_7]^T \\
&= [I_0 \quad a_1 I_0 \cos\theta \quad a_2 I_0 \cos\theta \quad a_3 I_0 \cos\theta \quad a_1 I_0 \sin\theta \quad a_2 I_0 \sin\theta \quad a_3 I_0 \sin\theta]^T
\end{aligned}
\tag{2.27}
$$

where $\theta = 2k_0 h + \varphi_0$. Once vector C is calculated, the position of the coherence envelope peak is determined by

$$
h = \frac{1}{2k_0}\left(-\frac{a_2}{a_3}\right) = \frac{1}{2k_0}\left(-\frac{c_3}{c_4}\right) = \frac{1}{2k_0}\left(-\frac{c_6}{c_7}\right) \tag{2.28}
$$

For more accurate surface height, the phase information is considered, and the corresponding height is given by

$$
h' = \frac{1}{2k_0}\left(\theta_m + 2\pi \cdot Int\left[\frac{2k_0 h - \theta_m}{2\pi}\right]\right) \tag{2.29}
$$

where $Int[\ ]$ indicates integer operation.

$$\theta_m = \tan^{-1}\left(\frac{\sin\theta}{\cos\theta}\right) = \tan^{-1}\left(\frac{c_5}{c_2}\right) \tag{2.30}$$

This method was claimed to provide a maximum measurement error of less than $\pm 0.05\lambda_0$ in the presence of external disturbances of up to 14.2% of the maximum fringe contrast. However, if the disturbance level increases, this method may not be effective. Moreover, the calculated surface height is dependent on the mean wave number of the white light source, which may not keep constant for different objects. This will cause wavelength calibration for different test objects.

Five kinds of methods for the fringe analysis of 3-D surface profiling using vertical scanning white light interferometry have been reviewed. The first one has disadvantage of low resolution and accuracy and is very sensitive to noise. The methods using phase-shifting technique and direct quadratic polynomial fitting are dependent on the mean wavelength of a white light source. This requires the mean wavelength should be precisely known for high accurate measurements. In the methods of digital filtering and analysis in spatial frequency domain, the spatial (vertical scanning series) signal is transformed into frequency domain, and the frequency components near a central frequency are used to extract the position of maximum contrast. Thus, noise with frequencies close to the central frequency will introduce errors in results, because the Fourier transform window is a frequency band and hence keeps noise within bandwidth. This thesis is to develop new methods independent of the mean wavelength of a light source (automatic calibration of the

mean wavelength) and insensitive to noise for the fringe analysis of white light interferometry. Then, the new algorithm is extended to analyze white light interference fringe patterns for layered structures.

2.3 Wavelet applications in optical fringe analysis

Wavelet analysis (Daubechies, 1992) is a relatively new and robust mathematical tool for signal processing, and has been widely applied to fringe analysis in optical measurement. The wavelet analysis has been used to reduce speckle noise in holographic fringe patterns (Odegard et al, 1996). Berger et al (1997) proposed a new evaluation technique combined with the wavelet transformation for speckle interferometric deformation measurement. Whereas, Cherbuliez et al (1999) applied wavelet analysis technique to live fringe patterns to achieve real-time measurement in dynamic conditions. Two-dimensional (2-D) interferometric phase distributions were also mapped by the use of complex Morlet wavelet (Walkins et al, 1999). Wavelet transform also appeared in data processing of holographic interferometry and electronic speckle pattern interferometry (ESPI) (Li, 2000). In 2002, Federico and Haufmann proposed another numerical method based on CWT for phase retrieval in ESPI. In the same year, Shakher et al applied wavelet filtering to vibration analysis using digital speckle pattern interferometry. The wavelet was also applied as a data processing tool to velocity measurement using interferometric techniques (Fu et al, 2004). At the same time, instantaneous velocity displacement and contour measurement was implemented by use of shadow moiré and temporal wavelet

analysis (Tay et al, 2004). In a recent study, fringe-density estimation was another application of wavelet analysis, in which one-dimensional (1-D) complex Morlet wavelet transform was applied to a 2-D fringe pattern to estimate the fringe density (Quan et al, 2005). The Gabor wavelet has been used to analyze the spatial carrier fringe patterns (Zhong and Weng, 2004), while 2-D CWT was also proposed to demodulate spatial carrier fringe patterns and was tested using computer-generated and real fringes by Gdeisat et al (2006). In 2005, Zhou presented a new method, which employed Daubechies wavelet as the mother wavelet, to analyze spatial carrier fringe patterns. One could also find the application of 2-D CWT in strain analysis using moiré interferometry (Kadooka et al, 2003). Thin-film thickness profile was measured using wavelength-scanning interferometry with a data-processing tool based on wavelet transform (Hwang et al, 2008). Recently, wavelet analysis was used for analysis of white light interferograms (Recknagel and Notni, 1997). In this application, an envelope of white light interferogram was obtained by the absolute modulus of the transform, and then a polynomial interpolation was applied to get the surface height of an object. Meanwhile, similar work was done by Sandoz (1997). In the thesis, the phase value of the signal retrieved by CWT will be used to accurately identify the local fringe peak, which indicates the surface height of a test object. This method based on a local fringe peak can provide a higher resolution than current method which is based on a global envelope peak.

2.4 Color fringe analysis in optical measurement

Since color images contain more information than gray-scale images do, color fringe patterns recorded provide an additional degree of freedom that is necessary for measuring a surface profile (Alexander, 1987). Hence, color fringe techniques were widely used in optical measurement in recent years. Another factor stimulating digital color fringe analysis is the development of electronic devices, such as illumination, recording and computation devices.

Most of the optical techniques went to 3-D measurement due to requirement of applications. Livnat et al (1980) proposed a method of two-color moiré mapping to solve the problem of hills and valleys. Häusler and Ritter (1993) employed color-code triangulation concept for parallel 3-D sensing. Geng (1996) proposed a new concept rainbow camera for high-speed 3-D vision systems, which was able to achieve instantaneous full-frame 3-D imaging capability. Desse (1997) presented a three-color differential interferometry combining the advantages of differential interferometry in white light with those of monochromatic interferometry. Hu and Qin (1997) proposed a digital color encoding method to the moiré technique and verified this method using a true-color frame grabber, a color monitor, a black-and-white CCD camera and a PC. An adaptive structured light method has been used to widen the range of potential range sensing applications, which could reach the accuracy and robustness of gray-coded technique while using fewer projection patterns, and hence time interval during which the scene must remain static can therefore be reduced (Caspi et al, 1998). Salvi et al (1998) extended colored technique to dynamic applications by projecting a

colored grid pattern on an object to gain a 3-D measurement of either static or dynamic scenes. In the study by Huang et al (1999), a color-encoded digital fringe projection technique was developed for high-speed 3-D surface contouring, in which only one color image is needed to obtain three phase maps to be used for surface height calculation.

In this decade, study of color technique in optical measurement is still a popular topic in research. Huang et al (2003) implemented high-speed shape measurement based on digital fringe projection, in which a computer-generated color fringe pattern whose RGB channels are sinusoidal fringe patterns with 120-deg phase shift between neighboring channels was utilized. One major problem of using color processing is that the appearance of color fringe patterns reflected from the object to the image recorder is affected by the color of the object surface itself. To solve this problem, Pan et al (2005) presented a color-coded binary fringe projection technique, in which an adaptive threshold scheme enabled the extraction of the 3-D information of an object without being affected by the color of the object. Chen et al (2007) implemented 3-D surface profiling with Fourier transform by projecting a bicolor sinusoidal fringe pattern consisting of two interlaced RGB format base color fringe patterns with π phase difference onto an object. Meanwhile, Chen et al (2007) proposed a projection system with a novel composite fringe pattern, which consisted of color encoded stripes and cosinoidal intensity fringes with parallel arrangement. The stripe edges offer absolute height phases with high accuracy and the cosinoidal fringes provide abundant relative phases involved in the intensity distribution. Wavelet transform was

utilized in the data processing. Meanwhile, a similar study was presented with Fourier transform processing method by Su (2007). Desse (2003) applied real-time color holographic interferometry to analyze aerodynamic flows. A digital three-color holographic interferometer has also been designed by Desse (2008) for flow analysis and the variations in refractive index induced by a candle flame were analyzed.

As reviewed above, most of color fringe analysis techniques were applied to fringe projection and holographic interferometry. In these applications, color illuminations were required. However, white light interferometry, whose interferometric patterns are essentially color images, has not fully utilized the advantage of color fringe analysis in data processing. This thesis will investigate the topic of color fringe analysis in vertical scanning white light interferometry.

CHAPTER THREE

DEVELOPMENT OF THEORY

3.1 Vertical scanning white light interferometric measurement

The main difference between white light and laser interferometry is that a laser source is replaced with a low-coherent white light as an illumination source. A schematic Michelson-type white light interferometer is shown in Fig. 3.1. The object and reference mirror respectively produce object and reference beams, which interfere with each other when the OPD between them is within the coherence range of the light source.

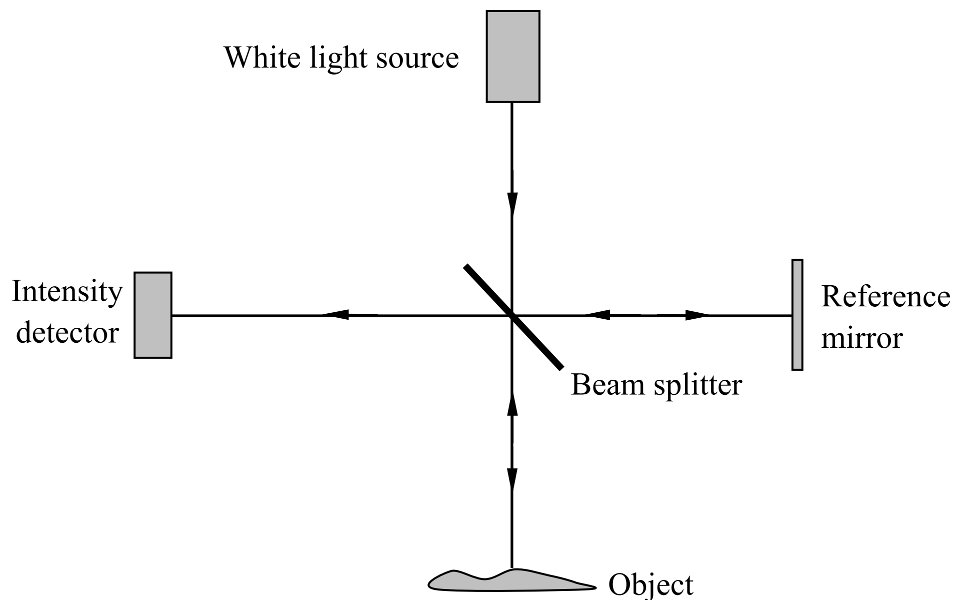

Fig. 3.1 Schematic diagram of a white light interferometer

A complex form of object and reference beams propagating onto the detector are respectively written as $E_r(t)$ and $E_o(t+\tau)$. τ is the time delay of the object beam relative to the reference beam and is determined by

$$\tau = \frac{Z}{c} \tag{3.1}$$

where Z is the OPD between two interference beams and c is the speed of the wave front. Superposition of wave (Hecht, 2002) results in

$$E(\tau) = E_r(t) + E_o(t+\tau) \tag{3.2}$$

The resultant intensity sensed by the detector can be expressed as (Hecht, 2002)

$$I(\tau) = \left\langle \left[E_r(t) + E_0(t+\tau)\right]\left[E_r(t) + E_0(t+\tau)\right]^* \right\rangle \tag{3.3}$$

where $\langle \ \rangle$ is a time average operator and * denotes a complex conjugate operation. Equation (3.3) can be further written as

$$I(\tau) = I_r + I_o + C(\tau) \tag{3.4}$$

where the first two terms I_r and I_o are the self-coherence intensities of reference and object beams and $I_r = \left\langle E_r(t) E_r(t)^* \right\rangle$, $I_o = \left\langle E_o(t+\tau) E_o(t+\tau)^* \right\rangle$. The last term is the cross-coherence intensity depending on the time delay between the two beams and can be expressed as

$$C(\tau) = 2\left\langle E_r(t)E_o(t+\tau)^*\right\rangle \tag{3.5}$$

The phase difference between two beams due to the OPD is given by

$$\varphi = 2\pi v_0 \tau \tag{3.6}$$

where v_0 is the central frequency of the light source. We can rewrite Eq. (3.4) according to Eq. (3.5) and (3.6)

$$I(\tau) = I_r + I_o + 2\sqrt{I_r I_o}\left|C_t(\tau)\right|\cos(2\pi v_0 \tau) \tag{3.7}$$

According to the Wiener-Khintcine theorem, the temporal coherence function $C_t(\tau)$ is the Fourier transform of the power spectral density $S(v)$ of the light source and is given by

$$C_t(\tau) = \int_0^\infty S(v)\exp(-j2\pi\tau)dv \tag{3.8}$$

For a light source with a Gaussian spectrum, the power spectral density is normally given by (Schmitt, 1999)

$$S(v) = \frac{2\sqrt{\ln 2/\pi}}{\Delta v}\exp\left[-4\ln 2\left(\frac{v-v_0}{\Delta v}\right)^2\right] \tag{3.9}$$

where Δv is a half-power bandwidth of the light source. Integrating Eq. (3.9), we have

$$I(\tau) = I_r + I_o + 2\sqrt{I_r I_o} \exp\left[-\left(\frac{\pi \Delta v \tau}{2\sqrt{\ln 2}}\right)^2\right]\cos(2\pi v_0 \tau) \tag{3.10}$$

From Eq. (3.1) and Eq. (3.10) using $v_{0.} = c\lambda_0$, the intensity function is rewritten as

$$I(Z) = I_0 + \gamma I_0 \exp\left[-\left(\frac{Z}{2l_c}\right)^2\right]\cos\left(\frac{2\pi}{\lambda_0} Z\right) \tag{3.11}$$

where I_0 represents the background intensity and γ is a constant. $l_c = \frac{c\sqrt{\ln 2}}{\pi \Delta v}$ represents the coherence length of the light source.

As shown in Fig. 3.1, if the surface of the object with respect to the reference mirror surface has a variation *h*, the OPD will be *2h*. Therefore, the intensity detected in terms of the surface variation is readily expressed by

$$I(h) = I_0 + \gamma I_0 \exp\left[-\left(\frac{h}{l_c}\right)^2\right]\cos\left(\frac{4\pi}{\lambda_0} h\right) \tag{3.12}$$

The surface height can be obtained with the fringe patterns. A 3-D surface profile will be readily obtained with $h(x, y)$ where (x, y) are the 2-D coordinates.

3.1.1 Micro-cantilever inspection

Micro-cantilevers are important components used in micro-electro-mechanical systems (MEMS). It is necessary to find a way to inspect the geometric parameters. A side view of a micro-cantilever is shown in Fig. 3.2. It is easy to obtain signal on the top surface of the micro-cantilever using an optical method. However, it is difficult to detect obstructed surface beneath the micro-cantilever, which is the remains of a

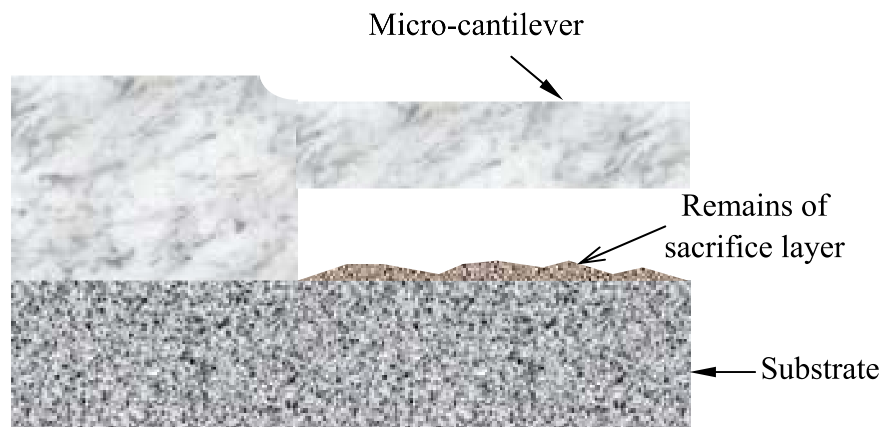

Fig. 3.2 Side view of a micro-cantilever structure

sacrificial layer, without proper illumination. Figure 3.3 shows a proposed illumination system to overcome the problem. The system is simplified as a single thin convex lens with a focal length *f*, and a lens diameter *D*. Each point on the lens emits a light cone as shown in dashed lines in Fig. 3.3. To illuminate the entire substrate surface obstructed by the micro-cantilever, the following condition must be satisfied

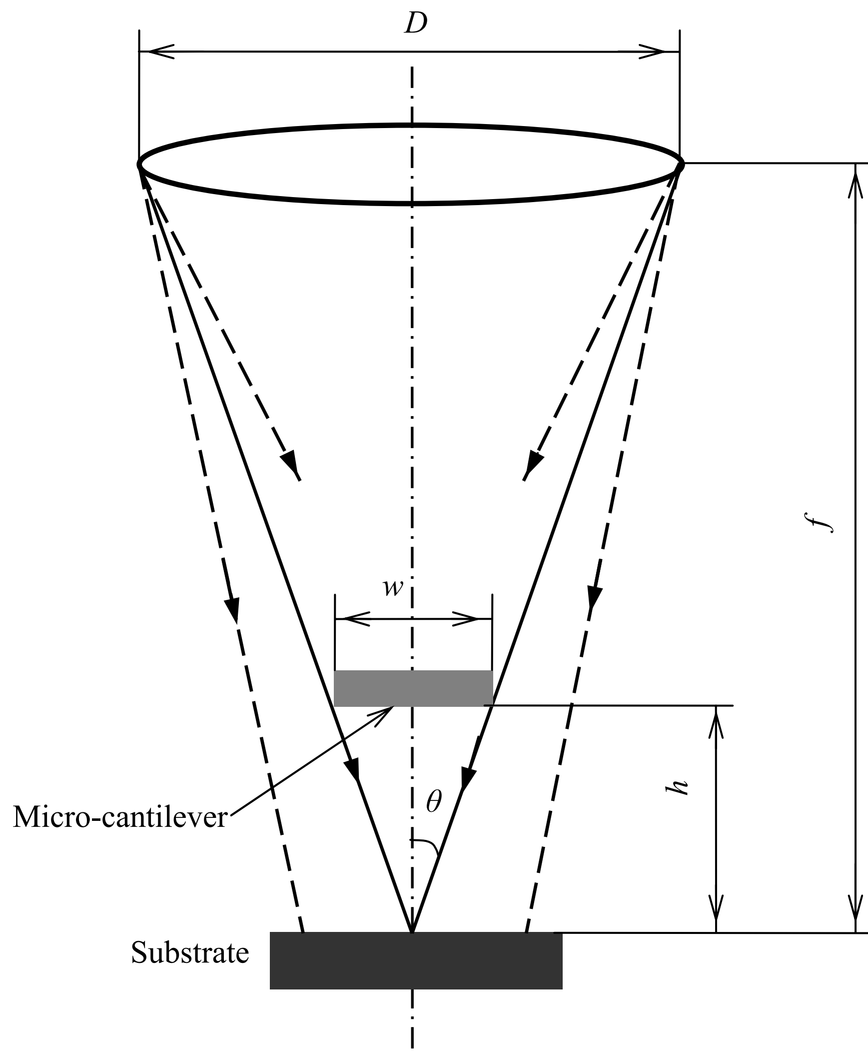

Fig. 3.3 Model of underneath surface measurement

$$\frac{D/2}{f} > \frac{w/2}{h} \tag{3.13}$$

Since $\tan\theta = \dfrac{D/2}{f}$, for complete illumination of the substrate, the condition necessitates

$$\tan\theta > \frac{w}{2h} \tag{3.14}$$

where w is the width of the micro-cantilever, h is the distance between the cantilever and substrate surface. Note that $\sin\theta$ is a numerical aperture of the illumination system. It is also readily seen that an additional condition requires that the height from the substrate to the top-surface of the cantilever does not exceed the working distance of the objective. This requirement is achieved with a Mirau objective.

3.1.2 Inspection of layered structures

Figure 3.4 shows a schematic diagram of a layered structure with various refractive indexes n_1, n_2, …, n_m and thicknesses of t_1, t_2, …, t_m. The dashed lines indicate the optical path distances from the reference plane to different interfaces of the structure. When the structure is illuminated, the beam reflected from each interface will interfere with the reference beam and produce m number of inference zones on the intensity recorded as shown in Fig. 3.5 during vertical scanning. The intensity response of a point on the structure can be approximated by

$$\begin{aligned} I(z) = I_0 &+ \gamma_0 I_0 g(z-z_0)\cos\left[2k_0(z-z_0)+\varphi_0\right] \\ &+ \gamma_1 I_0 g(z-z_1)\cos\left[2k_0(z-z_1)+\varphi_1\right] \\ &+ \gamma_2 I_0 g(z-z_2)\cos[2k_0(z-z_2)+\varphi_2] \\ &+ \cdots \\ &+ \gamma_m I_0 g(z-z_m)\cos[2k_0(z-z_m)+\varphi_m] \end{aligned} \tag{3.15}$$

where k_0 is the mean wave number of the light source,

$g(z - z_m) = \exp\{-[(z - z_m)/l_c]^2\}$ is a coherence envelope function and z_m

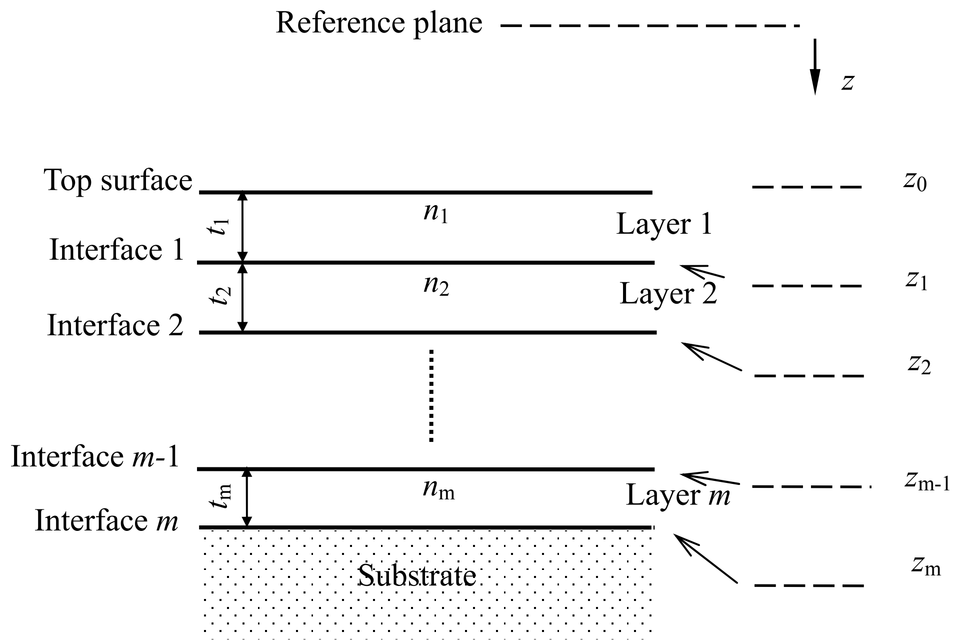

Fig. 3.4 Schematic of a layered structure

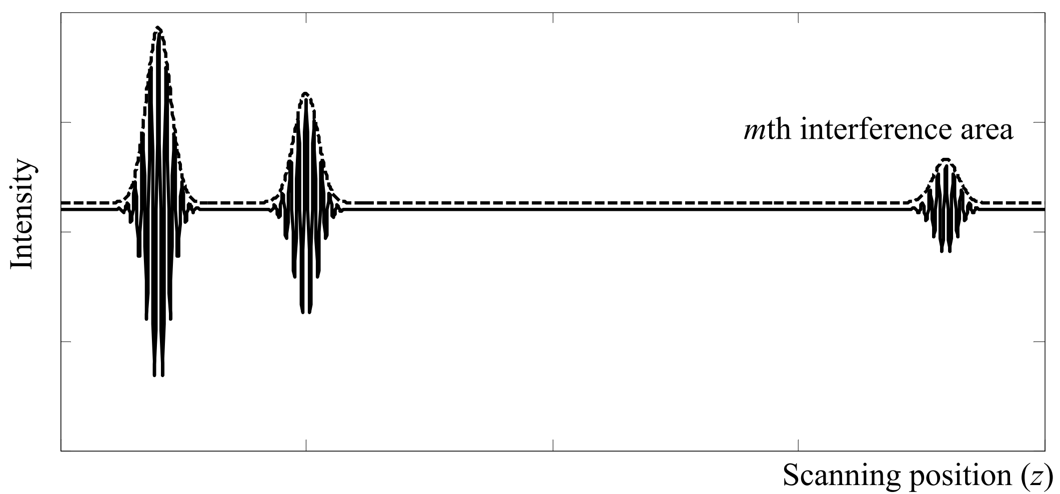

Fig. 3.5 A intensity response of a layered structure

indicates the optical path distance from the reference plane to the *m*th interface. Hence, the thickness of each layer is given by

$$t_m = \frac{z_m - z_{m-1}}{n_m} \qquad m = 1,2,3,\cdots,m \tag{3.16}$$

where n_m is the refractive index of the *m*th layer.

3.2 Fringe analysis using continuous wavelet transform

Wavelet transform maps a signal function $s(t)$ into a two-dimensional domain, a time-scale plane, which is normally denoted by $W(a,b)$ given by (Abbate et al, 2001)

$$W(a,b) = \frac{1}{\sqrt{a}}\int_{-\infty}^{+\infty} s(t)h^*\left(\frac{t-b}{a}\right)dt = \int_{-\infty}^{+\infty} s(t)h_{ab}^*(t)dt \tag{3.17}$$

where * indicates a complex conjugate operation and $h(t)$ is generally called mother wavelet, and a basis function of the transform, called daughter wavelet, is given by

$$h_{ab} = \frac{1}{\sqrt{a}}h\left(\frac{t-b}{a}\right) \tag{3.18}$$

$h_{ab}(t)$ is a set of basis functions obtained from the mother wavelet $h(t)$ by compression or dilation using scaling parameter *a* and temporal translation using shift

parameter *b*. The scaling parameter *a* is positive and varies from 0 to ∞ ($a > 0$). For $a < 1$, the transform performs compression of the signal, and for $a > 1$, the transform performs dilation of the signal. The signal $s(t)$ can be reconstructed from the wavelet coefficients $W(a,b)$ by inverse wavelet transform and is given by

$$s(t) = \frac{1}{C}\int_{-\infty}^{+\infty}\int_{0}^{\infty} W(a,b)h\left(\frac{t-b}{a}\right)\frac{da}{a^2}db \tag{3.19}$$

and constant *C* is given by

$$C = \int_{-\infty}^{+\infty}\frac{|H(\omega)|^2}{\omega}d\omega < \infty \tag{3.20}$$

Equation (3.19) is also referred as a reconstruction formula, inverse transform, or synthesis, and Eq. (3.20) is in general known as the admissibility condition (Strang, 1994).

3.2.1 Selection of mother wavelet

Selection of mother wavelet is important in signal processing. The selection is dependent on the signal frequency and spatial characteristics. For example, if a smooth signal is processed, a smooth wavelet having good frequency localization should be chosen; if one has a signal with discontinuities, a signal with good spatial localization is a good choice.

In the case of fringe analysis in white light interferometry, a signal defined by Eq. (3.12) is processed. The signal is also demonstrated in Fig. 2.4. It is a smooth signal with a Gaussian modulation. It is noted from Eq. (3.17) that CWT uses different daughter wavelets with different frequencies to scan a signal along the temporal direction as illustrated in Fig. 3.6, and calculates correlation coefficients between the signal and wavelets. When a signal and a wavelet match in both frequency and temporal position, a maximum correlation coefficient is obtained. That means the wavelet transform finds out the maximum similarity between the signal and a wavelet. Therefore, a Morlet wavelet with a Gaussian modulation is a good choice for signal

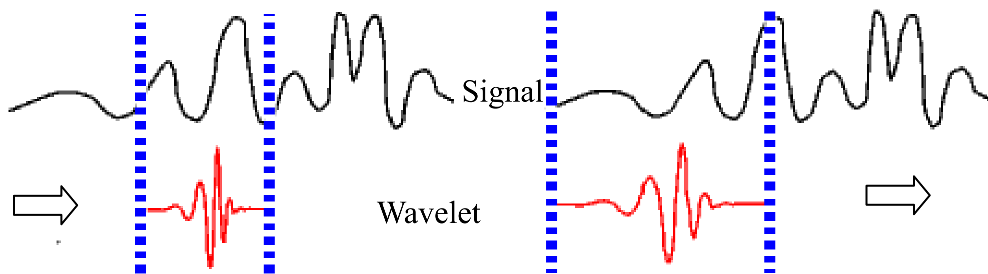

Fig. 3.6 Illustration of a continuous wavelet transform

processing in white light interferometry. In addition, in optical fringe analysis, phase retrieval is normally required. Hence, a complex Morlet is chosen as the mother wavelet, which is normally given by

$$h(t) = g(t)\exp(j\omega_0 t) \tag{3.21}$$

where ω_0 is the mother frequency and $g(t)$ is given by

$$g(t) = \exp\left(-\frac{t^2}{2}\right) \tag{3.22}$$

The frequencies of daughter wavelets ω are obtained from the mother frequency by the scaling parameter a.

$$\omega = \frac{\omega_0}{a} \tag{3.23}$$

Thus, a daughter wavelet can be expressed by

$$h_{ab}(t) = \frac{1}{\sqrt{a}} \exp\left[-\frac{(t-b)^2}{2a^2}\right] \exp\left[j\frac{\omega_0}{a}(t-b)\right] \tag{3.24}$$

Equation (3.24) implies that the scaling parameter a not only determines the frequency of a daughter wavelet but also the width of the correlation window. So, the coefficient function of a CWT with Morlet wavelet as the mother wavelet can be rewritten based on Eq. (3.17) as

$$W(a,b) = \frac{1}{\sqrt{a}} \int_{-\infty}^{+\infty} s(t) \exp\left[-\frac{(t-b)^2}{2a^2}\right] \exp\left[-j\frac{\omega_0}{a}(t-b)\right] \tag{3.25}$$

In order to satisfy the admissibility condition given by Eq. (3.20), ω_0 should be larger than 5. If the frequency of a signal does not change significantly, a larger value

of ω_0 is always beneficial.

3.2.2 Data analysis in white light interferometric measurement

Data processing of white light interferometric measurement involves scanning locations of zero OPD, which indicate the surface height. In the current methods, an envelope of intensity response is extracted, and the maximum location of an envelope corresponding to a zero-order fringe is identified and hence the surface height is determined. The interference intensity varies in a sinusoidal form while the global intensity variation is modulated by an envelope pattern. Since a vertical scanning step is in nanometers, using a local fringe peak to determine the surface height would be more accurate than retrieving a global coherence envelope. In addition, the local fringes form a sinusoidal pattern and phase information can be used to determine a local OPD. Figure 3.7 shows a method for determining the maximum peak of a local fringe. Since values of recorded intensities are discrete (shown as solid dots in Fig. 3.7), a recorded fringe peak value may not indicate the actual peak of a continuous fringe pattern. As shown in Fig. 3.7, a solid dot, which is a sampling point on a continuous fringe pattern, indicates that *h'* is the peak position of a zero-order fringe, while in fact *h* is the actual peak location. The difference Δh between *h* and *h'* is given by

$$\Delta h = h' - h = \frac{\lambda_0}{4\pi}\varphi \tag{3.26}$$

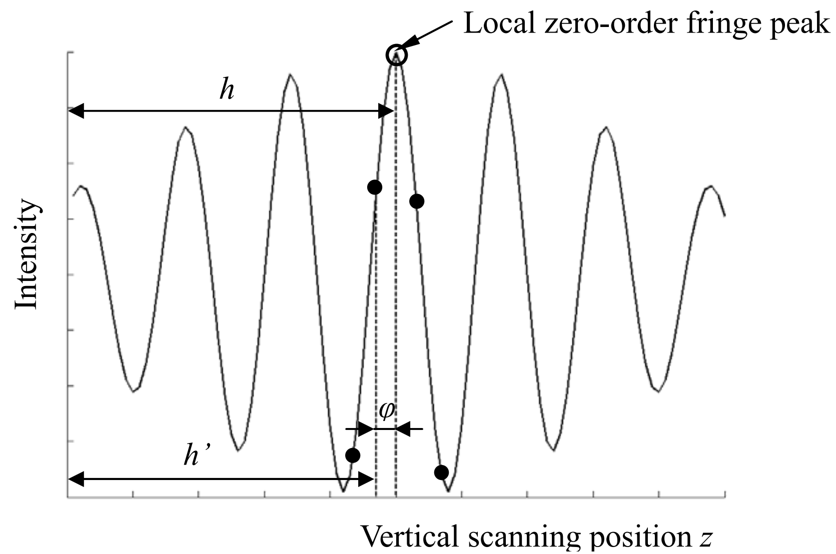

Fig. 3.7 Illustration of zero-order fringe peak determination

where φ is an apparent phase difference between *h'* and *h*. Hence, the actual surface height relative to the reference surface is given by

$$h = h' - \frac{\lambda_0}{4\pi}\varphi \tag{3.27}$$

Thus, once the sampled local fringe position *h'* and the phase-shift φ are obtained, the actual fringe peak position *h*, and hence the surface height, is determined.

The zero-order fringe can be indentified using CWT. Ignoring the background intensity (DC component), the white light interference intensity response is expressed as

$$I(z) = V(z)\cos\varphi(z) \tag{3.28}$$

The coefficients of the transform with complex Morlet wavelet as mother wavelet can be approximated by

$$W(a,b) = \frac{\sqrt{a}}{2} V(b) G\left[\omega_0 - a\varphi'(b)\right] \exp\left[j\varphi(b))\right] \qquad (3.29)$$

provided the following conditions are satisfied (Mallat, 1997).

$$\frac{\omega_0}{\left|\varphi'(b)\right|^2} \frac{\left|V''(b)\right|}{\left|V(b)\right|} << 1 \qquad (3.30)$$

and

$$\omega_0^2 \frac{\left|\varphi''(b)\right|}{\left|\varphi'(b)\right|} << 1 \qquad (3.31)$$

where $G(\omega)$ is the Fourier transform of $g(t)$. Equations (3.30) and (3.31) show that V' and φ' must have slow variation if φ' is small but may vary much quickly for large instantaneous frequencies.

The trajectory maximum value of $\left|W(a,b)\right|^2$ is called a ridge in a time-scale plane. Since $\left|G(\omega)\right|$ reaches its maximum value at $\omega = 0$, $\left|W(a,b)\right|^2$ reaches its maximum when

$$\varphi'(b) = \frac{\omega_0}{a_0} \tag{3.32}$$

where $\varphi'(b)$ and a_0 are the frequency and the value of scaling parameter a on the ridge at instant b. Hence, the wavelet transform coefficients on the ridge can be expressed as

$$W(a_0, b) = \frac{\sqrt{a}}{2} V(b) G(0) \exp[j\varphi(b))] \tag{3.33}$$

It can be noted that the phase of the wavelet transform coefficients on the ridge is exactly the phase of the signal. The phase is given as

$$\varphi(b) = \tan^{-1}\left(\frac{\mathrm{Im}[W(a_0, b)]}{\mathrm{Re}[W(a_0, b)]}\right) \tag{3.34}$$

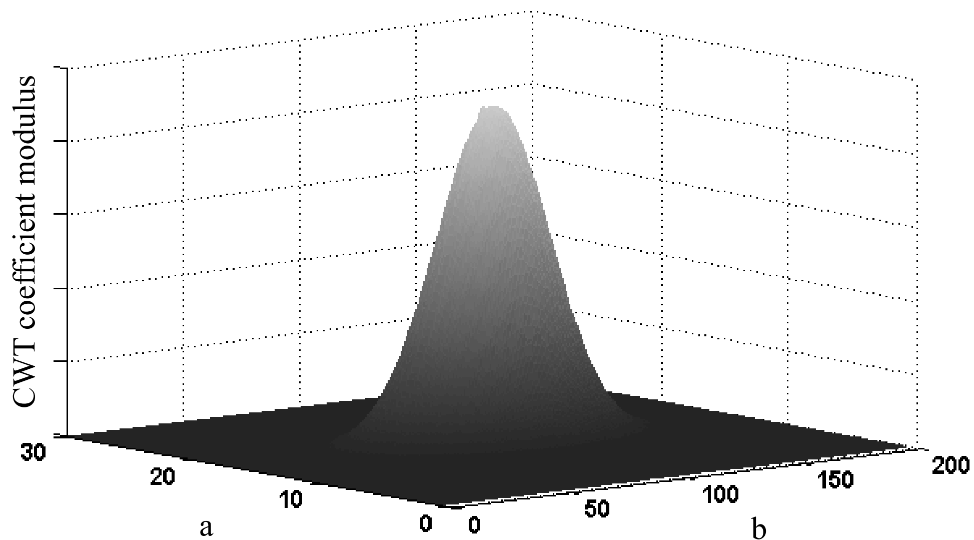

Fig. 3.8 Wavelet transform scalogram of a white light interferometric signal

Figure 3.8 shows the wavelet transform ($\omega_0 = 2\pi$) scalogram of a white light interferometric signal, and the signal, an envelope defined by the ridge and phases on the ridge are given in Fig. 3.9. The zero-order fringe can be determined by the

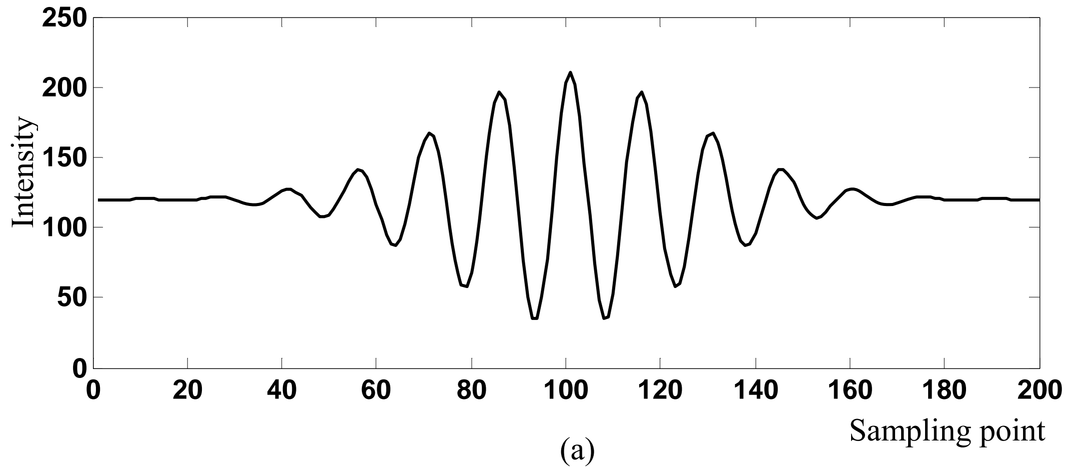

(a)

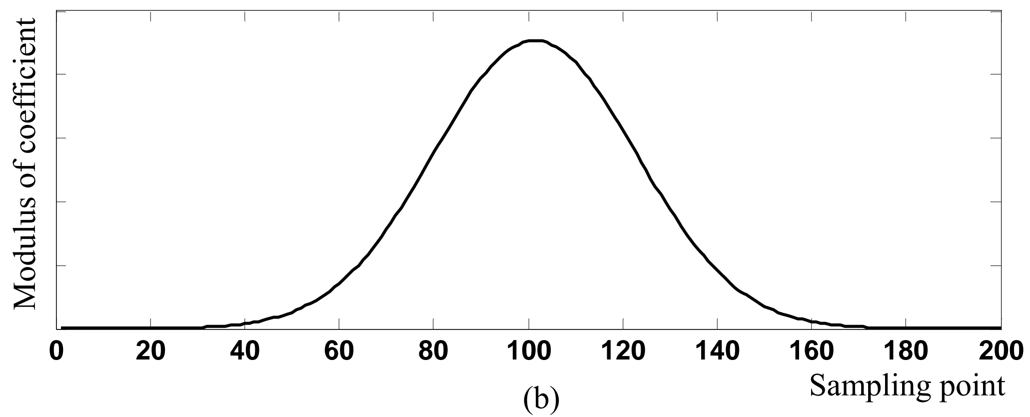

(b)

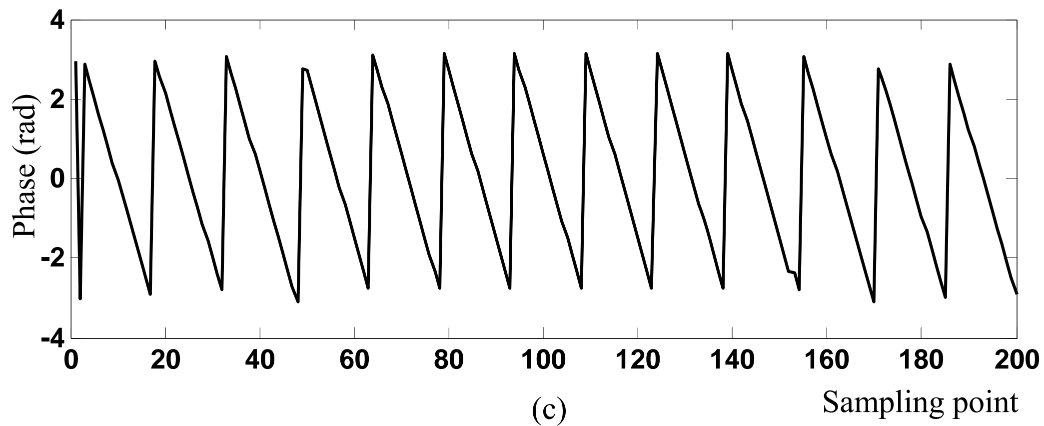

(c)

Fig. 3.9 (a) A white light interferometric signal; (b) coherence envelope defined by the ridge; (c) phases on the ridge

maximum of the envelope at $b = b_0$. The phase at this point is given by

$$\varphi = \tan^{-1}\left(\frac{\mathrm{Im}[W(a_0, b_0)]}{\mathrm{Re}[W(a_0, b_0)]}\right) \tag{3.35}$$

and Eq. (3.27) can be rewritten as follows.

$$h = h' - \frac{\lambda_0}{4\pi}\tan^{-1}\left(\frac{\mathrm{Im}[W(a_0, b_0)]}{\mathrm{Re}[W(a_0, b_0)]}\right) \tag{3.36}$$

where h' is determined by the peak of the envelope defined by the ridge, and the mean wavelength λ_0 is determined by the frequency on the ridge peak, which is exactly the frequency of the signal.

$$\lambda_0 = \frac{4\pi\Delta}{\varphi'(b_0)} = \frac{4\pi\Delta a_0}{\omega_0} \tag{3.37}$$

where Δ is the vertical scan increment in the measurement.

3.3 Color fringe analysis in white light interferometry

In previous methods involving white light interferometry, only monochrome images were employed for 3-D surface profiling. However, white light interference fringe patterns in essence contain color fringes. When a white light fringe pattern is converted into a monochrome image, some inherent information is lost. However, if a

white light interference fringe pattern is recorded using a three-channel (R: red; G: green; B: blue) color camera, three different intensity responses with wavelengths of $\lambda_R, \lambda_G, \lambda_B$ are obtained and they can be expressed as

$$\begin{aligned} I_R(z) &= I_{0R} + V_R(z)\cos\varphi_R(z) \\ I_G(z) &= I_{0G} + V_G(z)\cos\varphi_G(z) \\ I_B(z) &= I_{0B} + V_B(z)\cos\varphi_B(z) \end{aligned} \quad (3.38)$$

where z is a vertical scanning position. If a single-CCD color camera is used to record a fringe pattern, the intensity responses of three channels defined by Eq. (3.37) cannot be obtained. This is because each pixel of a single-CCD color camera records only an intensity of one channel, and the values of the other two channels are obtained through spatial color interpolation which is carried out electronically by the camera. Thus, a single-CCD color camera is unable to record color fringe patterns for this algorithm because two channels do not record real intensities. Therefore, a 3-CCD color camera is required. For each channel, the relationship between the phase φ and scanning position z is expressed as

$$\begin{aligned} \varphi_R(z) &= A_R z + B_R \\ \varphi_G(z) &= A_G z + B_G \\ \varphi_B(z) &= B_B z + B_B \end{aligned} \quad (3.39)$$

The phases of the three channels R, G and B are shown in Fig. 3.10. The zero-OPD locations of the three channels are theoretically at the same position along

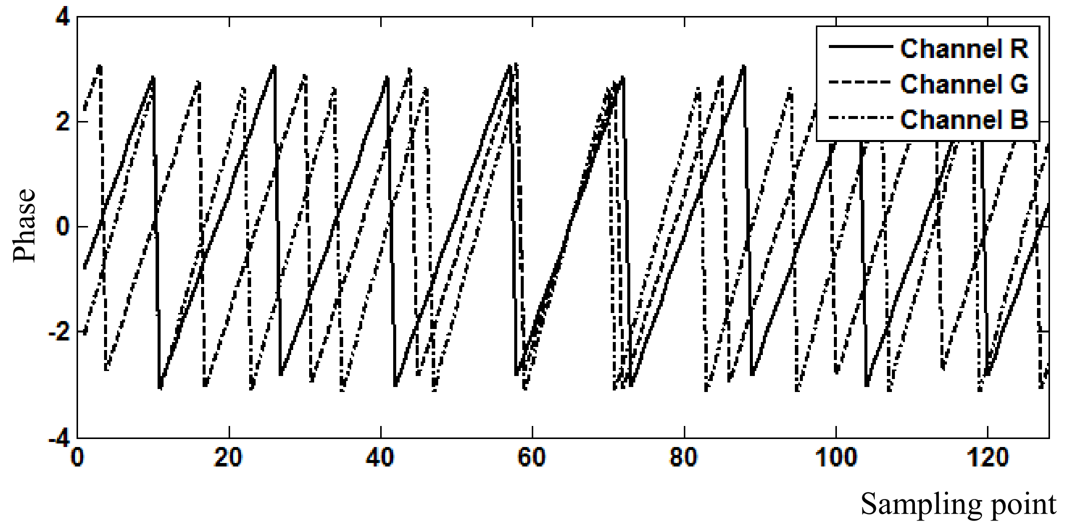

Fig. 3.10 Phases of channels R, G and B

the scanning direction. It is noted that the phases are wrapped, but unwrapping is not required since the phases within a zero-order fringe can be used to determine the values of the constants in Eq. (3.39). Although the zero-OPD locations of channels R, G and B are theoretically at the same position along the scanning direction, this may not be realized in practice. In practice, an estimated zero-point position z_0 can be obtained when $\varphi_R^2 + \varphi_G^2 + \varphi_B^2$ reaches a minimum. For $\varphi_R^2 + \varphi_G^2 + \varphi_B^2$ to reach its minimum value, the following condition must be satisfied.

$$\frac{d(\varphi_R^2 + \varphi_G^2 + \varphi_B^2)}{dz} = 2\left(A_R^2 + A_G^2 + A_B^2\right)z + 2\left(A_R B_R + A_G B_B + A_B B_B\right) = 0 \tag{3.40}$$

Hence, the estimated zero-point position z_0, which indicates the actual surface height h of a point, is given by

$$h = z_0 = -\frac{A_R B_R + A_G B_B + A_B B_B}{A_R^2 + A_G^2 + A_B^2} \tag{3.41}$$

In order to determine the values of function coefficients A and B, the zero fringe order should be determined first and a new method for determining the zero fringe order is proposed as follows. The absolute values of phase differences between different channels are used:

$$\begin{aligned} d_{RG} &= |\varphi_R - \varphi_G| \\ d_{GB} &= |\varphi_G - \varphi_B| \end{aligned} \tag{3.42}$$

Figure 3.11 shows the absolute values of phase differences between channels R and G and those between channels G and B. It can be seen that the minimum absolute value shows the position of zero-order fringe. The method is effective when the

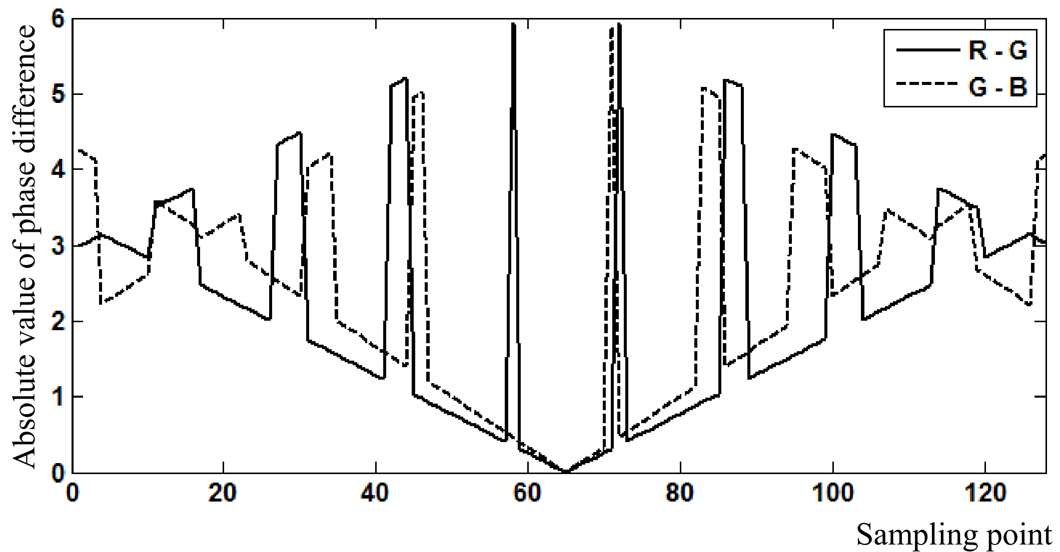

Fig. 3.11 Absolute values of phase differences between channels R and B and that between channels G and B

sampling points are within one equivalent wavelength λ_{RG} or λ_{GB}. An equivalent wavelength is defined as

$$\lambda_{RG} = \frac{\lambda_R \lambda_G}{\lambda_R - \lambda_G}$$
$$\lambda_{GB} = \frac{\lambda_G \lambda_B}{\lambda_G - \lambda_B} \tag{3.43}$$

A longer equivalent wavelength would provide a bigger sampling range along the vertical scanning direction. Hence using channels with a longer equivalent wavelength would be more effective in identifying the position of zero-order fringe.

Once the zero-order fringe is determined, the function coefficients *A* and *B* in Eq. (3.39) can be obtained using least square fit based on the phases retrieved. The phase function in terms of scanning position *z* for each channel is given by

$$\varphi_i = Az_i + B \quad i = 1,...,n \tag{3.44}$$

where *n* is the sampling number within the zero-order fringe. Using least square theory, *A* and *B* should satisfy the following conditions

$$\frac{\partial}{\partial A}\left(\sum_{i=1}^{n}(\varphi_i - Az_i - B)^2\right) = 0$$
$$\frac{\partial}{\partial B}\left(\sum_{i=1}^{n}(\varphi_i - Az_i - B)^2\right) = 0 \tag{3.45}$$

and

$$\begin{aligned} A\sum_{i=1}^{n} z_i^2 + B\sum_{i=1}^{n} z_i &= \sum_{i=1}^{n} z_i\varphi_i \\ A\sum_{i=1}^{n} z_i + Bn &= \sum_{i=1}^{n} \varphi_i \end{aligned} \tag{3.46}$$

Thus, the coefficients *A* and *B* are readily determined:

$$\begin{aligned} A &= \frac{n\sum_{i=1}^{n} z_i\varphi_i - \sum_{i=1}^{n} z_i \sum_{i=1}^{n} \varphi_i}{n\sum_{i=1}^{n} z_i^2 - \left(\sum_{i=1}^{n} z_i\right)^2} \\ B &= \frac{\sum_{i=1}^{n} z_i \sum_{i=1}^{n} z_i\varphi_i - \sum_{i=1}^{n} z_i^2 \sum_{i=1}^{n} \varphi_i}{\left(\sum_{i=1}^{n} z_i\right)^2 - n\sum_{i=1}^{n} z_i^2} \end{aligned} \tag{3.47}$$

The scanning position z_i is recorded during the scanning process and the phases are retrieved using the method described in section 3.2.2. The function coefficients *A* and *B* for each channel are determined by Eq. (3.47) and finally the surface height is determined by Eq. (3.41).

CHAPTER FOUR

EXPERIMENTATION AND SIMULATION

4.1 Experimental system

A unique experimental system, which can be easily transformed between Michelson-type and Mirau-type interferometers, was developed based on a conventional microscope for 3-D measurement/inspection using vertical scanning white light interferometry. Figure 4.1 shows the experimental set-up using Michelson interferometer, while a system using Mirau interferometer is shown in Fig. 4.2. As shown in Fig. 4.1, a light source goes through a collimator to illuminate the test object. A test sample is mounted on a PZT translation stage controlled by a PZT controller for vertical scanning along the optical *z*-axis. The light is split into two beams. One beam

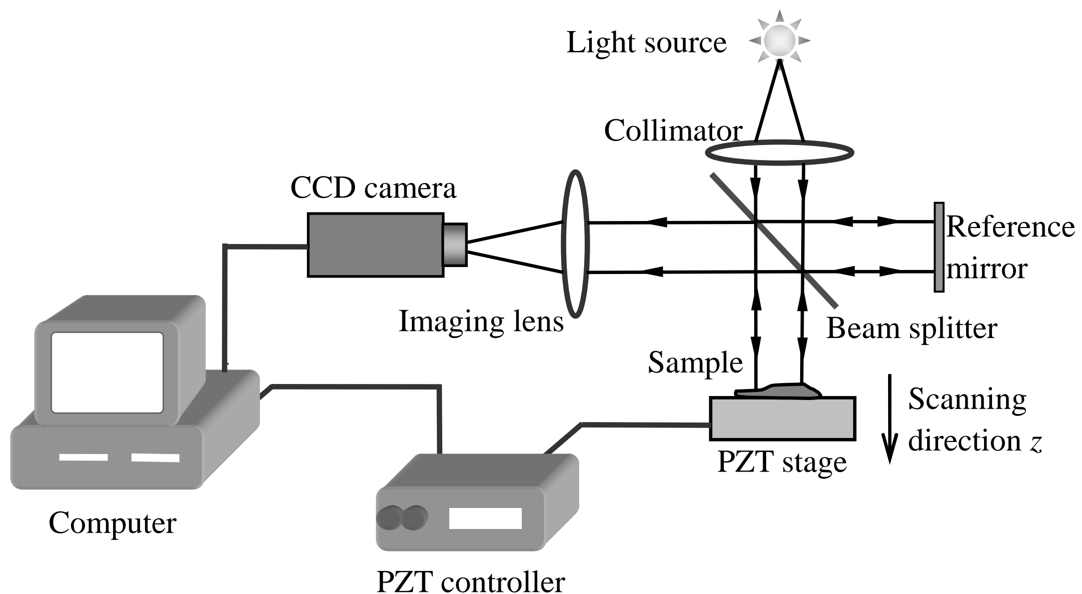

Fig. 4.1 Schematic layout of the experimental system using Michelson interferometer

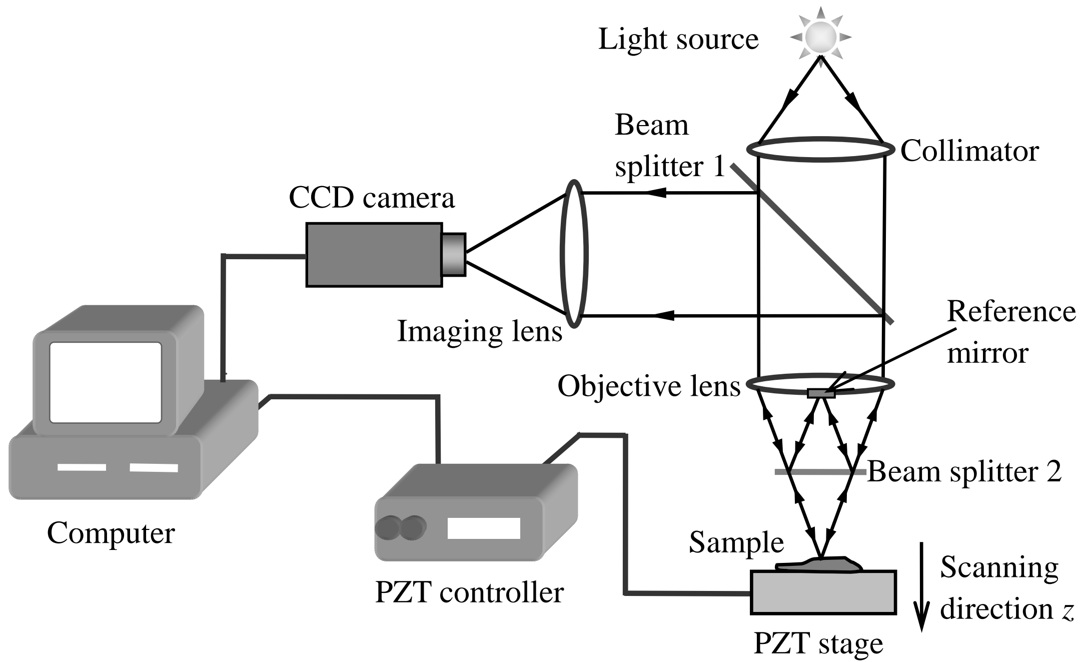

Fig. 4.2 Schematic layout of the experimental system using Mirau interferometer

shines onto the test sample as an object beam, while the other one is directed at a reference mirror. The reflected reference and object beams interfere with each other when the OPD between them is within the coherence range of the light source. The resulting interference fringe patterns are recorded on a sensor array of a CCD camera by an imaging lens and the recorded images are stored in a computer for processing. For each step of the translation stage movement, an image is captured for subsequent processing. In the Mirau interferometer set-up, the reference and object beams are produced by a mirror attached to the center of the objective lens and a beam splitter placed below the objective lens at half the focal length of the lens (beam splitter 2 in Fig. 4.2). This is to enable the Mirau interferometer to detect obstructed surfaces as described in section 3.1.1. The whole system is controlled by a computer through

software developed by the author.

Figure 4.3 shows the actual experimental system, which is uniquely modified based on a conventional microscope. It provides maximum field of view of 1666 µm × 1250 µm, while its vertical resolution and lateral resolution are able to reach 0.5 nm and 0.54 µm respectively. A halogen lamp, PHILIPS-EKE-13629-21V150W, is used as the illumination source of the system, and light is guided into the collimator using an optical fiber. The spatial filter controls the light intensity by adjusting its size. The PZT stage is mounted on a 3-D translation stage, which is used for initial positioning of a test object. A tilt plate is mounted on the PZT stage to adjust the tilt of a test

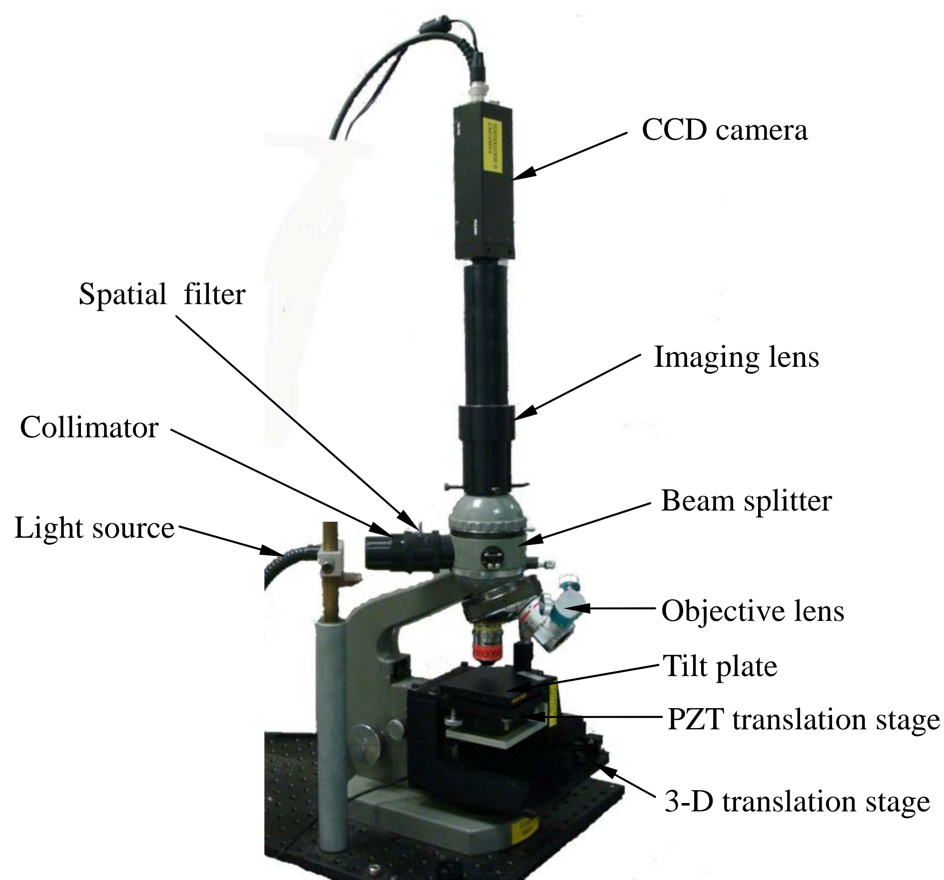

Fig. 4.3 Actual experimental set-up for 3-D measurement

object, which is attached on the plate. The objective lens can be altered readily depending on its applications. An aberration correction imaging lens is incorporated in the optical set-up. The key components of the experimental system are as follows:

Camera: A PULNiX TM-765E monochrome interlace CCD camera with the resolution of 768 × 576 pixels and image acquiring rate of 25 frames per second is employed in the system.

Objective lens: Three NIKON interferometry lenses, one Michelson-type lens (5×) and two Mirau-type lenses (10×, 20×) are used. Please refer to Appendix D for more details.

Vertical scanning stage: A PI PZT nanopositioning stage P-622.ZCD is utilized. Controlled by a PI LVPZT servo-controller E-665.CR, it can achieve a resolution of 1 nm with repeatability error less than 0.02%.

4.2 Software algorithms used for experiments

4.2.1 Image recording

An image recording program to capture fringe patterns during vertical scanning was developed. A flowchart of the algorithm is shown in Fig. 4.4. Each fringe pattern of a scan is recorded by the CCD camera and stored in the computer. Both the camera and PZT stage are controlled by a computer a via RS-232 serial port. The PZT stage scan one step once a movement command is received from the serial port. A record command is sent to the image grabber after a certain settling time and then the captured image is stored for subsequent processing. The program was developed

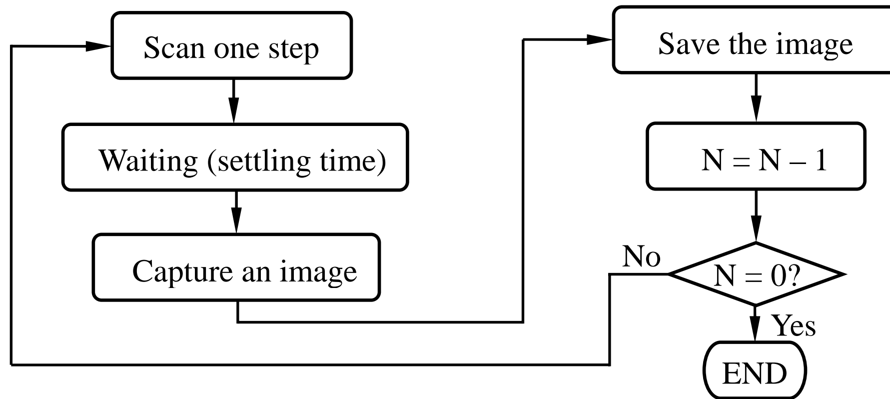

N: The total number of scan steps

Fig. 4.4 Flowchart of fringe pattern recording

using Microsoft Visual C++ 6.0 language. A pseudocode of the subprogram is as shown below.

```
Initialize Camera;
Initialize PZT controller;
int n;
double Vincrement;                    //The increment of the vertical scanning
for (n=1, N, n++)                    //N is the total number of scan steps
    CSerial.Send(int port, char MOV, Vincrement); //Send movement command
    Sleep(settling time);
    Cserial.Send(int port, char CAP); //Send capture command
    CSave(String path, buffer);    //Save the image to the harddisk
    n++;
end
```

The main imaging control program developed using Microsoft Visual C++ 6.0 is shown in Appendix A.

4.2.2 Gray fringe analysis

The gray fringe analysis algorithm based on CWT was programmed using MATLAB. The procedure of the fringe analysis is outlined in Fig. 4.5. In the data processing, the

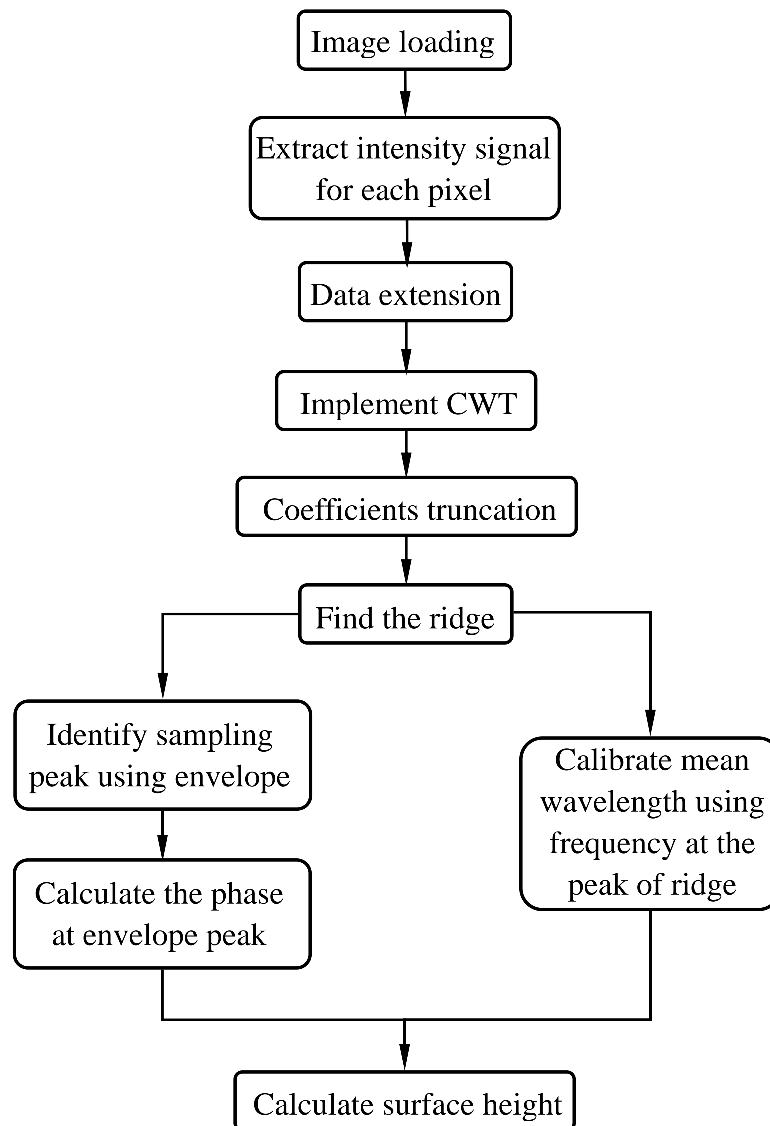

Fig. 4.5 Procedure of the fringe analysis using CWT

fringe images are first loaded to the memory and then the intensity response signal of each pixel is extracted. The intensity signal data is extended to eliminate border effect of CWT. CWT is then applied to the extended intensity signal of a pixel on the image. After the coefficients are truncated, a ridge is located on the time-scale plane. A sampling peak is identified on an envelope defined by the ridge. The phase of the peak is then calculated using Eq. (3.35). Meanwhile, a mean wavelength of the illumination source is determined by the frequency at the ridge peak. Finally, the

surface height is calculated using Eq. (3.27) or (3.36). Following the procedure, the height of each pixel, which corresponds to each point of a test object, is obtained and hence the 3-D surface of the object is mapped. Since wavelet transform shows border effect at the beginning and end of each signal, a signal extension is required in order not to lose signal information. Symmetrical extension is employed since the signal is symmetrical with every small variation at the beginning and end of the signal as shown in Fig. 2.4 (a). After CWT, a coefficient truncation is applied to keep only the transform coefficients of the signal itself. Since the frequency at the ridge peak can be obtained in CWT, the mean wavelength of the light source is then able to be calibrated using the frequency. The sampling peak is also identified using the modulus of the coefficients on the ridge, which defines a coherence envelope of the signal. Note that in Fig. 4.5, phase calculation and wavelength calibration are illustrated in parallel in order to show that the surface height is determined by them together, while the MATLAB program execute the two tasks in sequence in stead of in parallel. The subroutine of the data processing is shown in Appendix B.

4.3 Simulations on color fringe analysis

An algorithm based on CWT for color fringe analysis was developed. A single-CCD color camera is not suitable for recording fringe in vertical scanning white light interferometric measurement because the signal from each of R, G and B channels is not defined by Eq. (3.11) or (3.38) due to its working principle as described in Chapter 3, while a 3-CCD color camera is able to satisfy the condition of the

algorithm for 3-D measurement. Unfortunately, a 3-CCD color camera was not available in the experiments. Therefore, simulations of 3-CCD color camera images were carried out to verify the proposed algorithm.

The signal from each of the three channels is an independent white light interferometric intensity response, which is defined by Eq. (3.12). Hence, three sets of white light interference signals are generated and are assigned to the three channels: R, G and B. In generating the fringes, the parameters in Eq. (3.12) are as shown in Table 4.1. The color fringes of a prescribed step profile were generated and processed using the proposed algorithm to retrieve 3-D property of the prescribed step.

Table 4.1 Parameters of the illumination source in simulations

Channel	I_0	γ	λ_0 (nm)	l_c (nm)
R	120	0.8	620	750
G	120	0.8	550	750
B	120	0.8	480	750

The fringe analysis algorithm structure is outlined in Fig. 4.6. The fringe images are loaded in the memory and the intensity response signal of each pixel is extracted. The intensity signal is extended to eliminate border effect of CWT. The CWT is applied to each extended signal of three channels and then data truncation is applied to keep only the transform coefficients of the signal itself. Consequently, a ridge on the time-scale plane is identified for each channel and then the phases over the ridges are calculated using Eq. (3.34). After the phases of the three channels are obtained, the

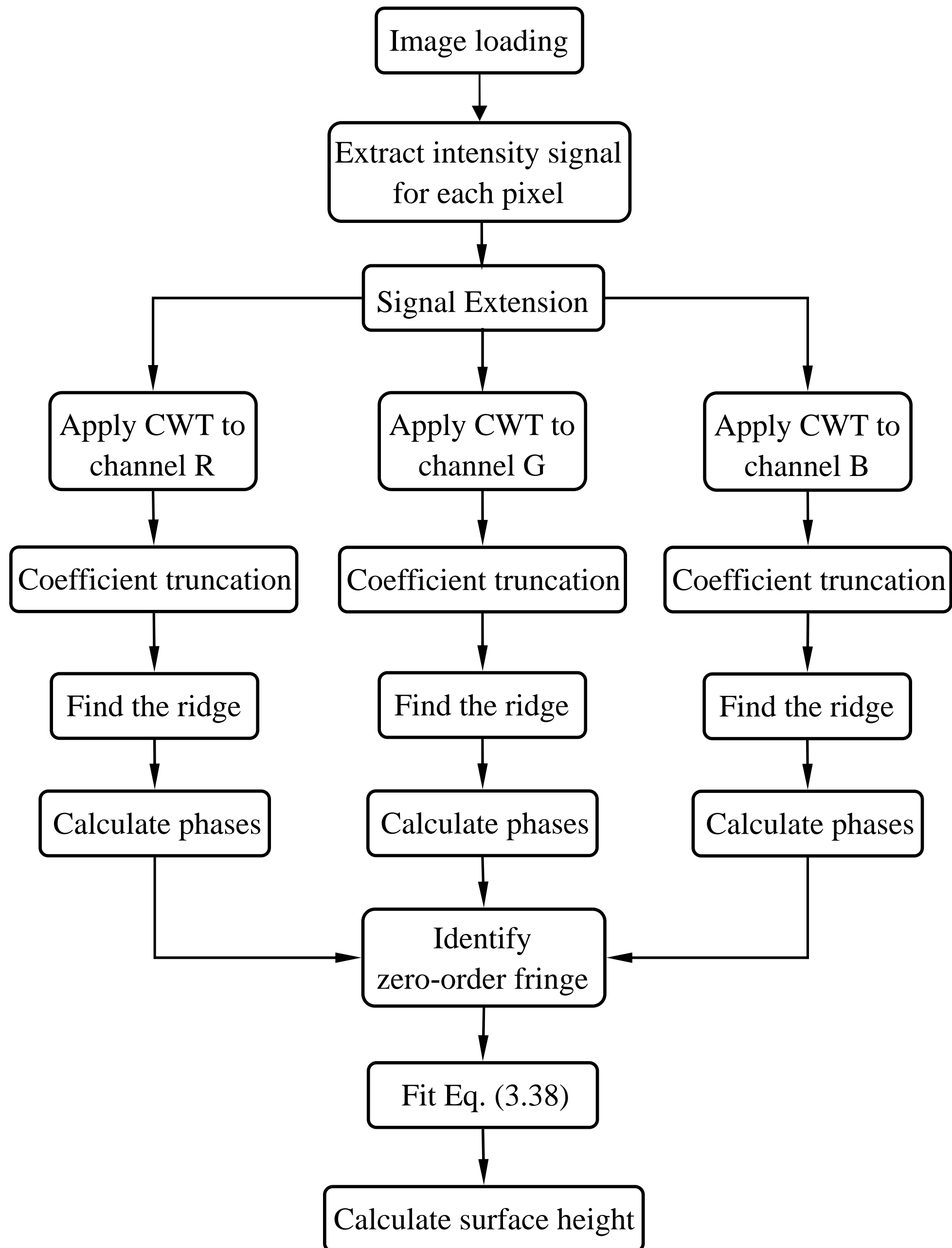

Fig. 4.6 Algorithm structure for color fringe analysis

zero-order fringe is identified using the proposed method. A least square fit is then applied to the phases in the zero-order fringe to determine the function coefficients in Eq. (3.39), and the surface height of a pixel is calculated using Eq. (3.41). With the height of each pixel, which corresponds to each point of a test object, a 3-D surface of

an object is mapped. Since wavelet transform shows border effect at the beginning and end of each signal, a signal extension is required in order not to lose signal information before CWT is applied. Symmetrical extension is employed since the signal is symmetrical with every small variation at the beginning and end of the signal. In Fig. 4.6 the R, G and B channels are illustrated in parallel in order to show that the zero-order fringe is determined by three separate channels, while the software calculates the three channel values in sequence. The subroutine of the program is shown in Appendix C.

CHAPTER FIVE

RESULTS AND DISCUSSION

5.1 3-D surface profiling

Two standard specimens (A and B as shown in Fig. 5.1) of step height values specified by NPL (National Physical Laboratory) as 1785.9 ± 3.8 nm and 23474 ± 14.1 nm were tested using the proposed Michelson layout set-up. Specimen A is a groove shape and specimen B is a ridge shape. The measured area of specimen A is 1666 μm × 1250μm, and that of specimen B is 1666 μm × 651 μm. The reconstructed

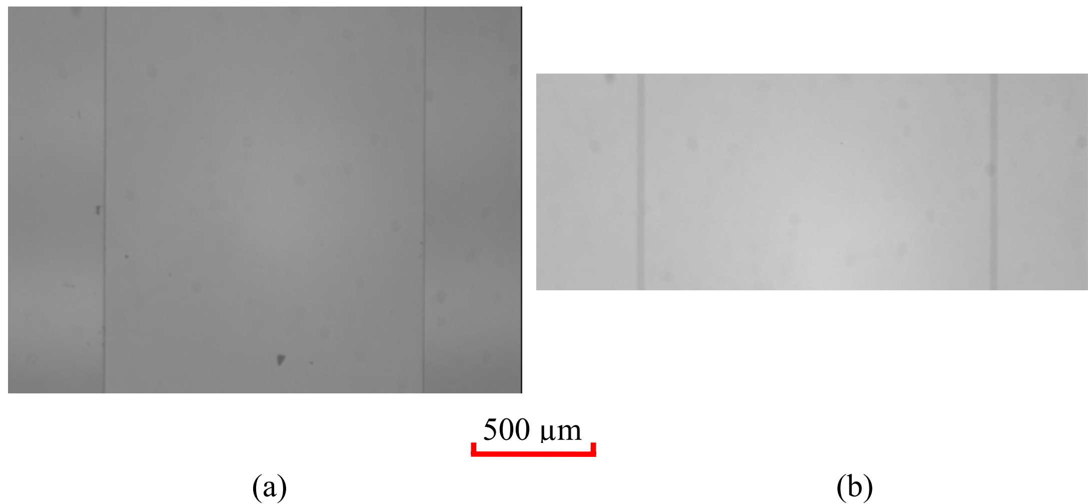

Fig. 5.1 (a) Top view of standard step specimen A; (b) top view of standard step specimen B

3-D surface profiles of the two specimens obtained by the proposed algorithm based on phase retrieval using CWT are shown in Fig. 5.2. The specimens were evaluated by selecting an area (542.5 μm × 217 μm) on the top surface and an area with the same dimensions on bottom surface at the same position in *x* direction and the difference between the mean heights of the two areas was taken as the height of the

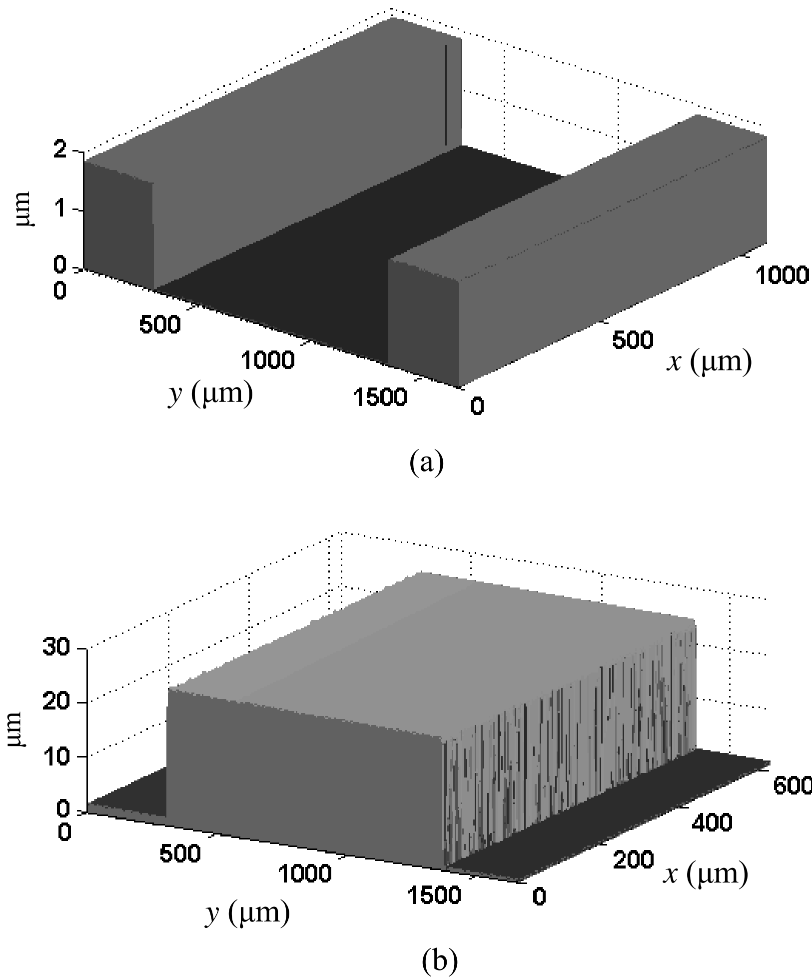

Fig. 5.2 (a) A 3-D plot of a step height standard 1785.9 ± 3.8nm;
(b) a 3-D plot of a step height standard 23474 ± 14.1nm

evaluated specimens. The measured values based on ten measurements taken are 1796 ± 9 nm and 23501 ± 19 nm respectively. The absolute deviations are 10.1 nm and 27 nm and the relative deviation are 0.57% and 0.12% respectively. From the deviation, it can be seen that the proposed method gives measured values very close to the specified standard values. This indicates that the proposed method is able to achieve very high measurement accuracy. It is also seen that the relative deviation of specimen B (0.12%) is smaller than that of specimen A (0.57%). This can be explained that a constant system noise will introduce a smaller relative error for a larger measurement

range. It is noted that the measured heights are slightly larger than the standard values. This is caused by two factors: one is misalignment of the scanning direction with optical axis, and another is tilting of the sample relative to the reference plane as shown in Fig. 5.3. A misalignment of angle β_1 between the scanning direction and the optical axis will cause the actual scan increment along the optical axis (Δ') to deviate from the scanning direction (Δ). Since the step height is obtained from the scanning direction, a larger step height value is obtained. Figure 5.3 (b) shows that the effect of a sample tilting of angle β_2 relative to the reference plane. It is seen that for a relative tilt of β_2 the height value *h* measured will be larger than the actual height *h'*. Actually the two factors cause the same effect on the final results, and hence can be considered as one combination, called alignment deviation β. The sources and

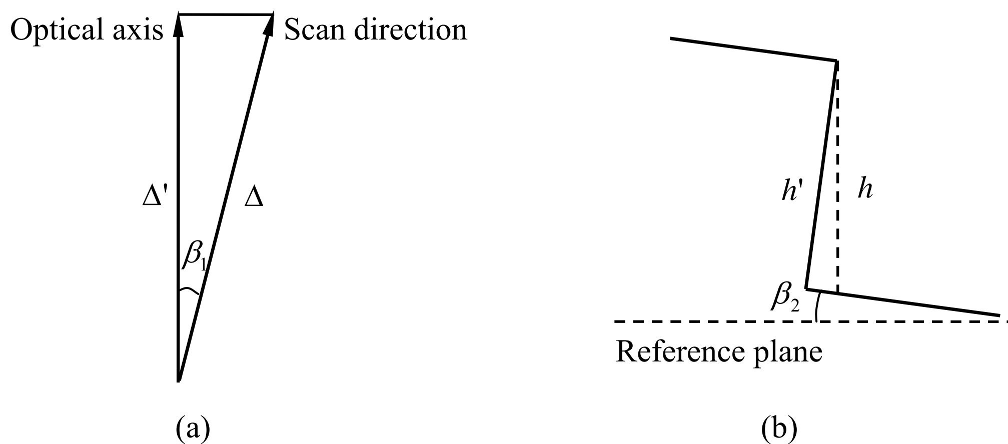

Fig. 5.3 (a) Misalignment; (b) relative tilt of reference plane

their contributions are given in Table 5.1. Misalignment of PZT translation stage to the optical axis is less then 0.2º, which is determined by the mechanical installation adapter between the PZT stage and the base of the instrument. The translation tilt of

the PZT stage itself is given by 1 μrad specified by the manufacturer, which results in 5.7×10^{-5} degrees alignment deviation. Misalignment of beam splitter is less than 0.2º, which is determined by its mechanical holder. Because the light beam goes through beam splitter twice, the misalignment of beam splitter results in 0.4º. Using a monochromatic interferometric method, the misalignment of reference mirror is able to be adjusted to less than one fringe in the field of view (1666 μm × 1250 μm). The wavelength of the light source, which was used to align reference mirror, is 640 nm. Thus, the contribution to the alignment deviation is given by $\arcsin(320/1250/1000) = 0.015°$. In order to facilitate adjustment and get good fringe quality, four fringes should be contained in the field of view, which causes alignment deviation of $\arcsin(4 \times 320/1250/1000) = 0.059°$. The total alignment deviation is 0.67º. For more confidence, the alignment deviation is expanded to 1º. The error of specimen A caused by the alignment deviation is given by $1785.9 \times (1 - \cos 1°) = 0.3$ nm, while the error of specimen B caused by the alignment deviation is calculated by

Table 5.1 Sources of alignment deviation and their contributions

Source of alignment deviation	Deviation value	Contribution to alignment deviation in degree
PZT alignment to optical axis	0.2º	0.2
PZT translation tilt	1μrad	5.7×10^{-5}
Beam splitter alignment	0.2º	0.4
Reference mirror alignment	1 fringe	0.015
Test object tilt	4 fringe	0.059
Total alignment deviation	-	0.67

$23474 \times (1-\cos 1°) = 3.5$ nm. Actually, the alignment deviation is one of the measurement uncertainty sources, which will be discussed in section 5.5.

A lamellar grating was also scanned and evaluated using the proposed Michelson-layout measurement system. Figure 5.4 shows a top view of the lamellar grating. The bright strips indicate top surfaces of the lamellar and the dark parts indicate the troughs. A 1 mm × 1 mm area was evaluated. A reconstructed 3-D plot of

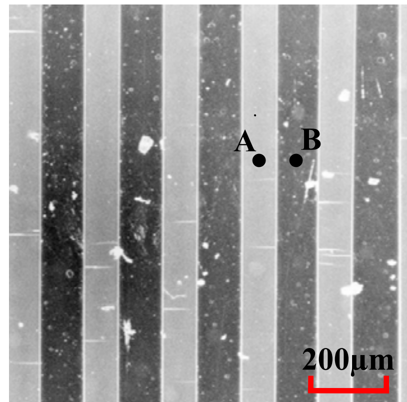

Fig. 5.4 A 2-D top view of a portion of a lamellar grating

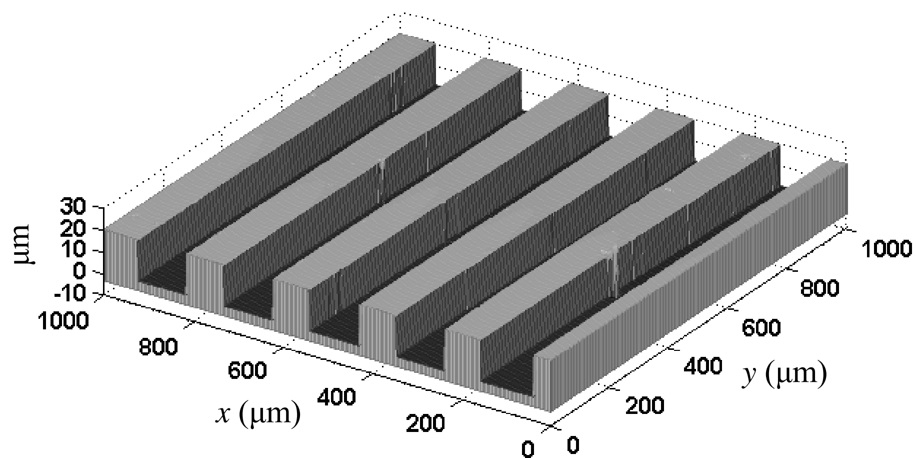

Fig. 5.5 A 3-D plot of a reconstructed lamellar grating

the structure is shown in Fig. 5.5. It can be seen that the lamellar grating is readily reconstructed and each step change is shown clearly. Such structure with sharp step changes is difficult to measure using normal monochromatic interferometry due to the phase ambiguity problem. The grating height is readily determined from the 3-D data of the structure. For example, the height difference between the points A and B (black dots as shown in Fig. 5.4) is given by 19.34 ± 0.02 μm. A cross-section along the horizontal line at $y = 620$ μm is plotted in Fig. 5.6. It is seen that the grating is well

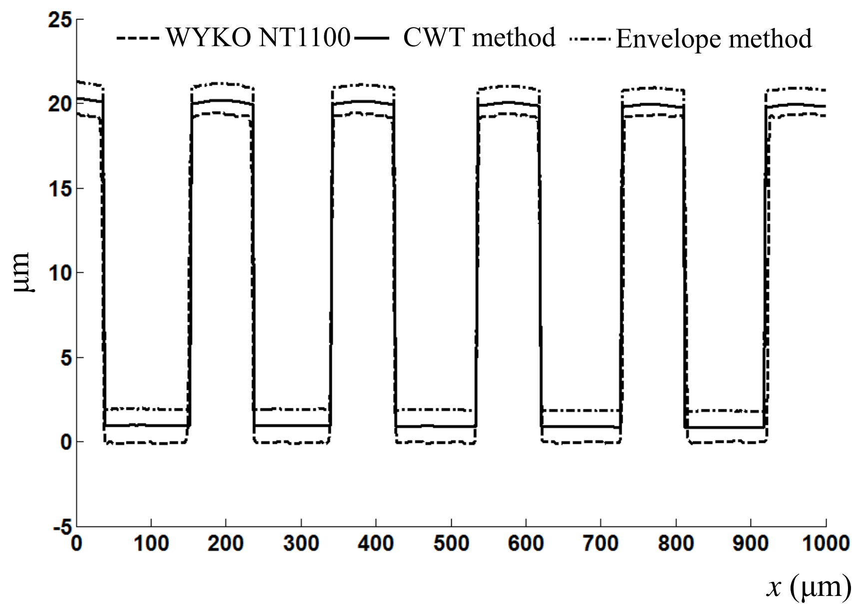

Fig. 5.6 Comparison of cross-sections obtained by different methods

defined especially along the edges of the steps. For comparison, data retrieved by the envelope method and a WYKO NT1100 profiler are also shown in Fig. 5.6. In order to distinguish between the sections, the plots are separated by a shift of 1 μm in the vertical direction. The maximum discrepancy between the results obtained by the proposed CWT method and the profiler is 0.6%, while that between the envelope method and the profiler is 1.6%. In addition to the profile, the roughness of the grating

surface was also evaluated. The RMS roughness value of the grating surface obtained by the profiler is 125 nm, while the values obtained by the CWT and envelope methods are 182 nm and 200 nm respectively. This again indicates that the proposed method shows a smaller discrepancy with the profiler. This is explained that the CWT method retrieve the surface height by locating a local fringe peak, while the envelope method obtained the surface height by identifying a global envelope peak. Another explanation is that CWT performs better in reducing noise than Fourier transform employed in the envelope method.

A computer simulation was also carried out to evaluate the validity of the algorithm. A prescribed surface profile (part of a sphere with diameter of 20 mm) as shown in Fig. 5.7 (a) was generated and a series of fringe patterns were simulated using Eq. (3.11) ($\lambda_0 = 600$ nm, $l_c = 750$ nm, $I_0 = 120$ and $\gamma = 0.8$). For a scanning increment of 20 nm, five different series of fringe patterns with random noise restricted to within 0%, 5%, 10%, 20% and 30% of the maximum fringe intensity were generated. Figure 5.7 (b) shows a 3-D profile reconstructed from the fringe patterns with a 10% noise incorporated using CWT method, while Fig. 5.7 (c) shows the profile obtained using the envelope method. It can be seen that the surface profile in Fig. 5.7 (c) shows a more noisy profile. The absolute errors of the results are shown in Figure 5.8. The error maps in the left column show errors introduced by the CWT method, while those in the right column indicate errors introduced by the envelope method. The maps (from the top) correspond to fringe patterns with 0%, 5%, 10%, 20%, and 30% noise incorporated. It can be seen that the results obtained with the

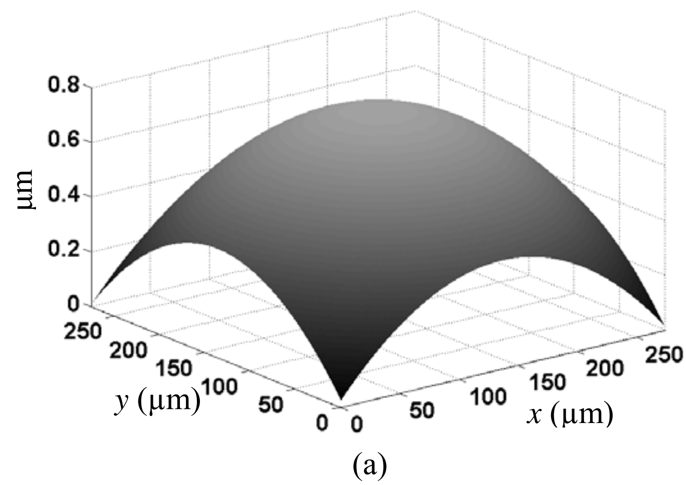

(a)

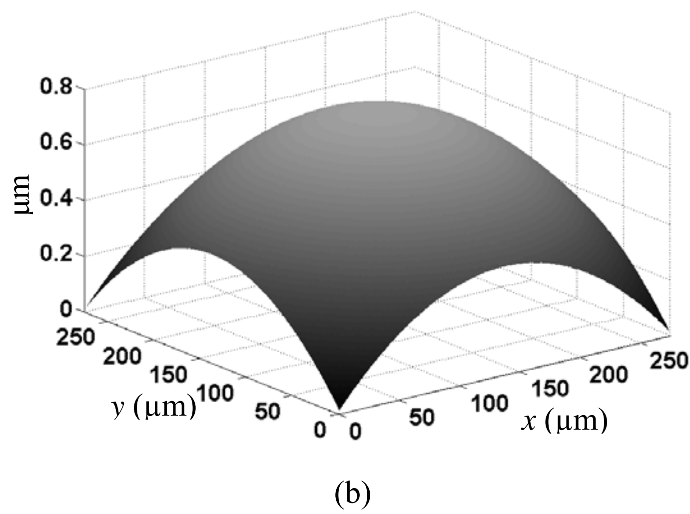

(b)

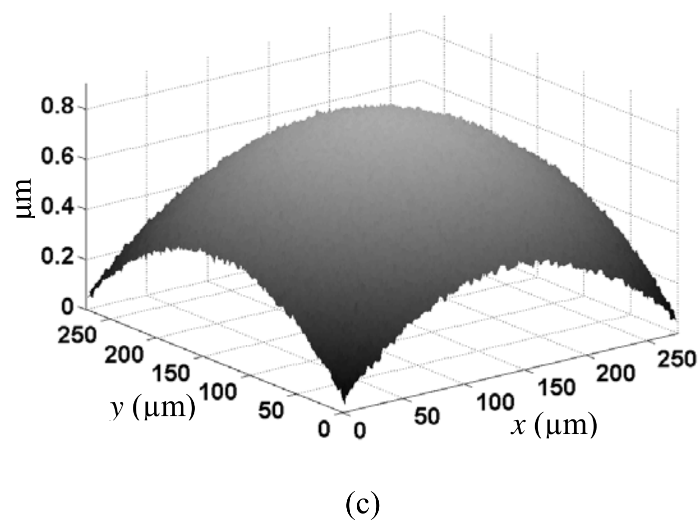

(c)

Fig. 5.7 (a) A prescribed surface; (b) reconstructed 3-D plot of the surface using CWT method; (c) reconstructed 3-D plot of the surface using envelope method

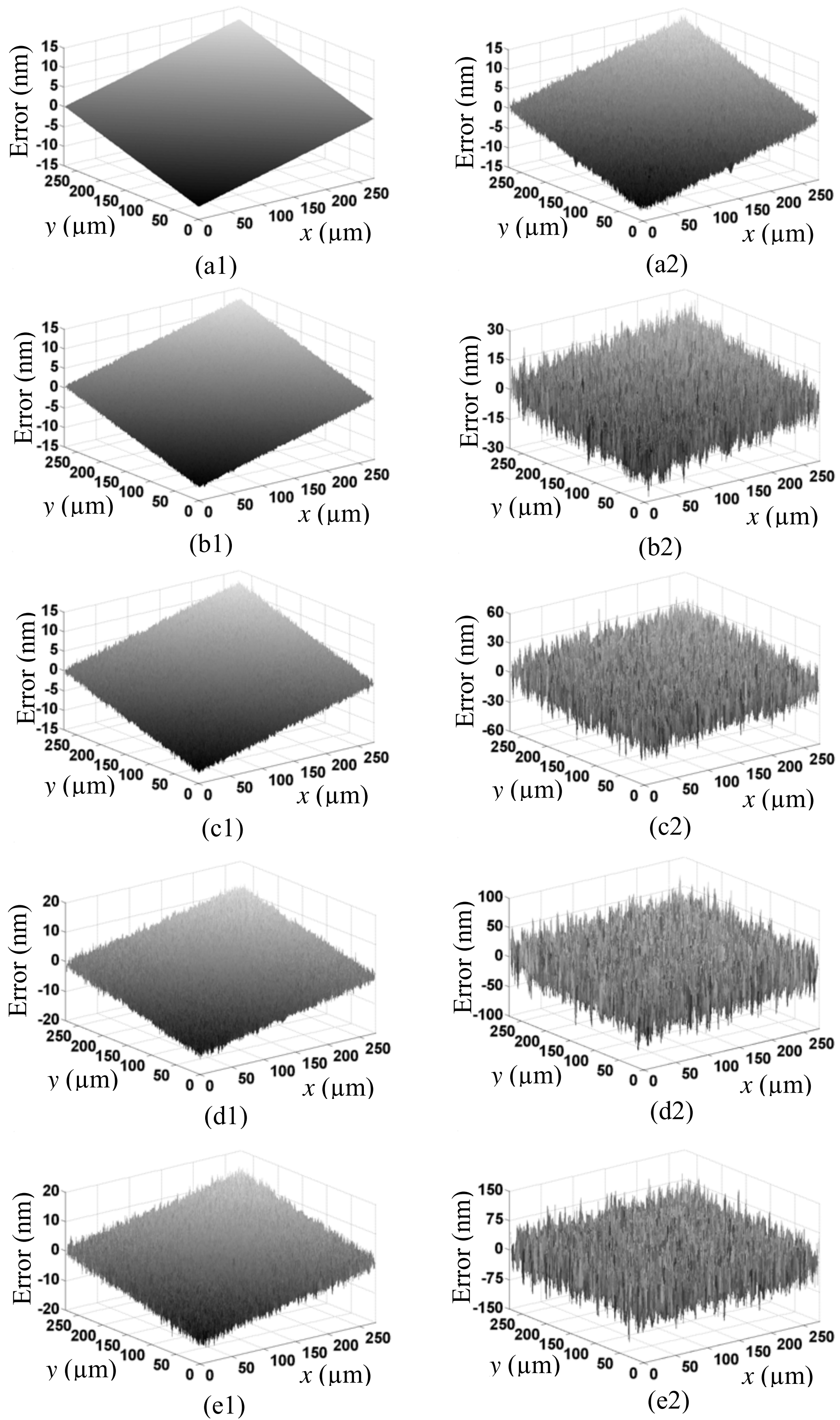

Fig. 5.8 Errors introduced by the algorithm

proposed CWT method show less error than those obtained with the envelope method. Figure 5.9 shows a comparison of relative errors introduced by the different methods.

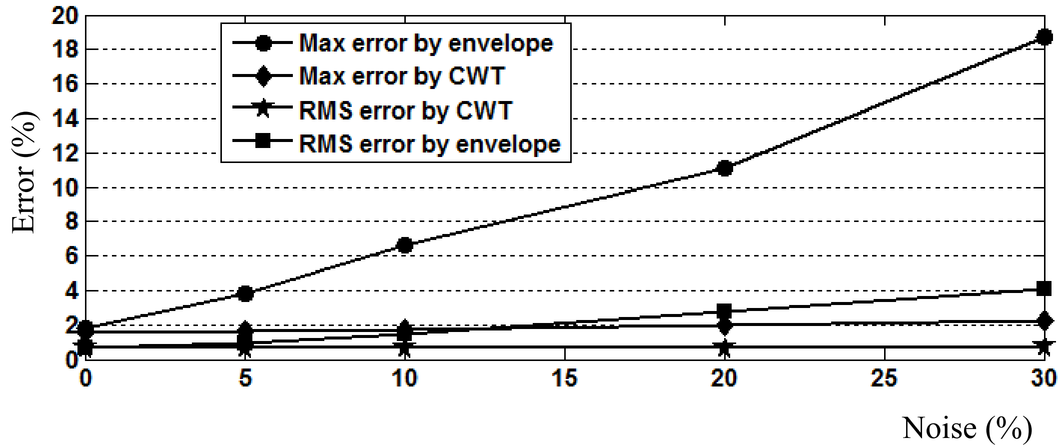

Fig. 5.9 Comparison of errors due to different noise levels

It is seen that the proposed CWT method is relatively unaffected by the noise, while the errors introduced by the envelope method increase drastically as the noise increases. This is explained that CWT is able to exactly determine the frequency of a signal and hence eliminate the effect of noise with other frequency, while Fourier transform cannot remove the noise with frequencies close to the signal frequency due to the filter window size. The influence of scanning increment is also investigated using fringe patterns with 10 percent noise incorporated, and the errors introduced are shown in Fig. 5.10. It can be seen that as the scanning interval increases, the error remains relatively constant. This indicates that the accuracy remains unaffected with large scanning interval. Hence, a large scanning increment can be used as long as the Nyquist sampling theorem is satisfied. It is noted in Fig. 5.10 that the errors introduced by the envelope method decrease slightly in the scanning range from 20 nm to 30 nm. This is due to the manual selection of filter window in Fourier transform.

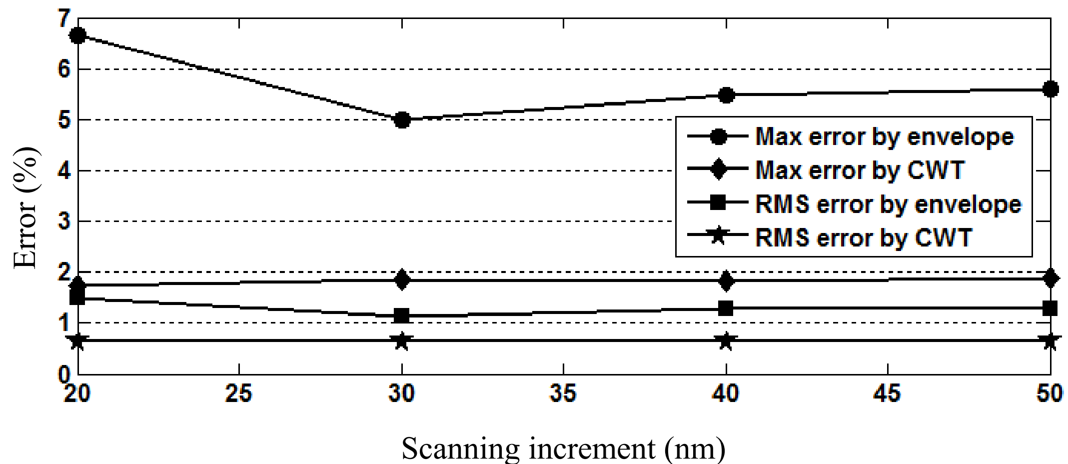

Fig. 5.10 Comparison of errors introduced by scanning increment

Figure 5.11 shows phase errors plot due to noise level. The errors include phase change due to surface reflection, which is assumed constant for a uniform test surface. Hence it is more meaningful to look into the standard deviation of error when the noise level changes. The standard deviation (0.009 rad) of phase error shown in Fig. 5.11 shows that the error increases slowly as the noise level increases.

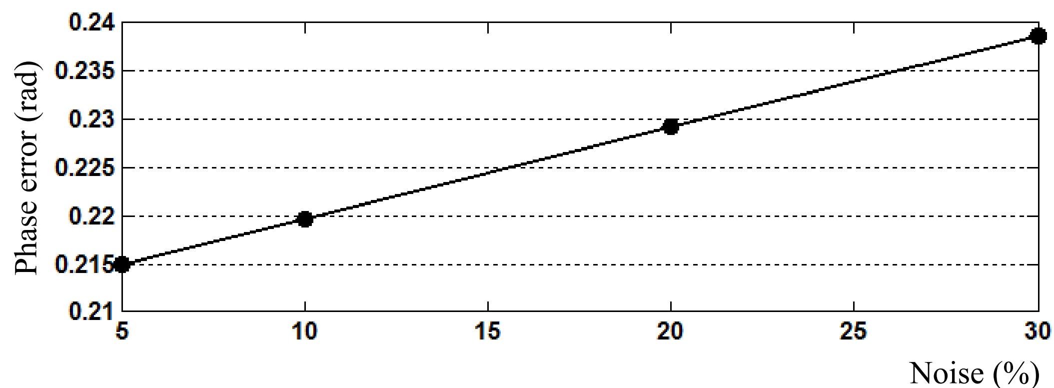

Fig. 5.11 Phase error plot in terms of noise level

The proposed method was also applied to the measurement of a micro-gear with diameter of 600 μm and average thickness of 2 μm. A 3-D profile of the micro-gear was reconstructed using the CWT algorithm as shown in Fig. 5.12 (a). From the 3-D

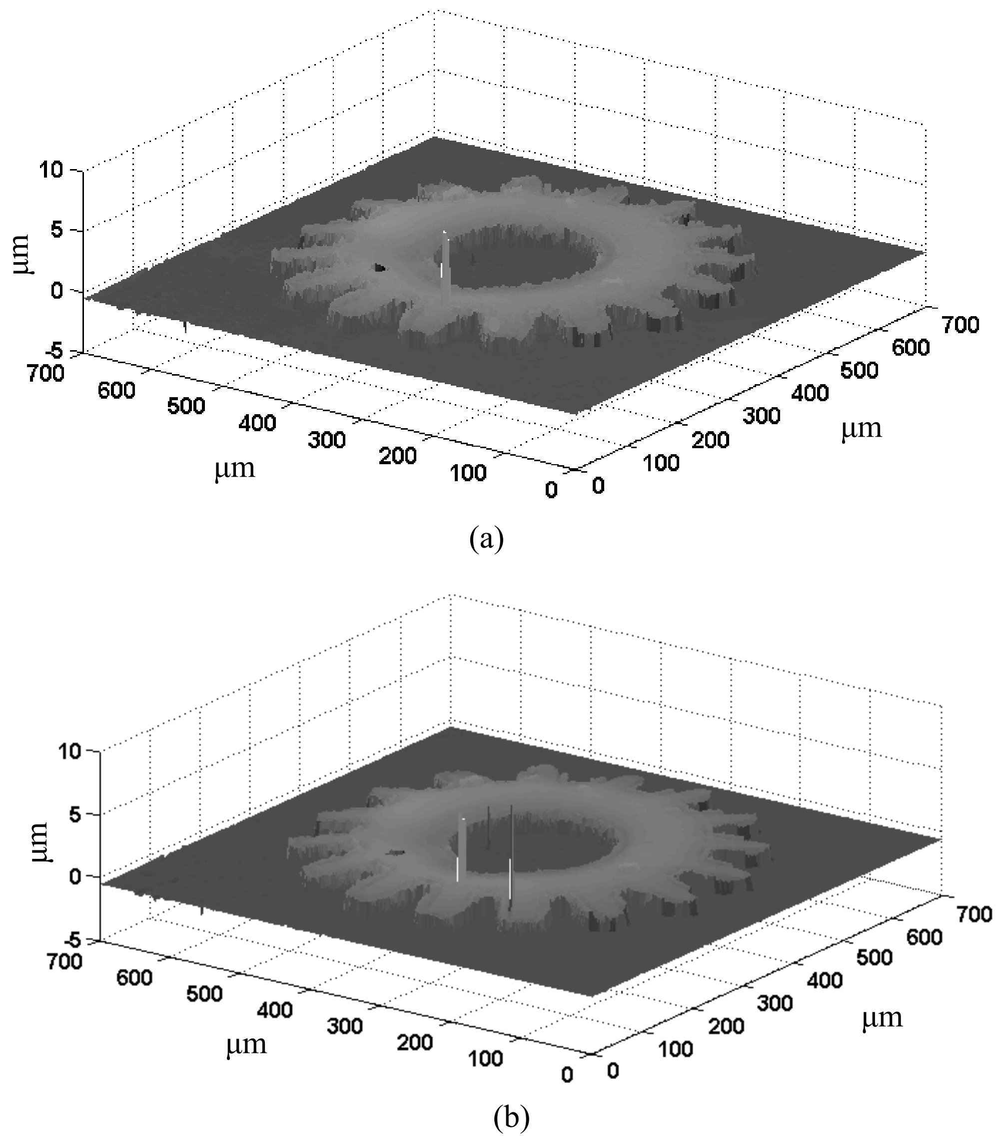

Fig. 5.12 (a) A reconstructed micro-gear surface using CWT method;
(b) a reconstructed micro-gear surface using envelope method

data of the micro-gear profile, the average thickness was determined as 2.13 μm, which has a discrepancy of 6.5% from the specified average thickness of 2 μm. As a comparison, a 3-D surface reconstructed using the envelope method is shown in Fig. 5.12 (b). It is seen that there are three noisy regions on the surface obtained by the envelope method compared to only one on the surface obtained by the CWT method. The results imply that the CWT method is more effective in reducing noise. The

results are consistent with the simulated results. The noisy region obtained by the CWT method may be due to a dust particle on the micro-gear as shown in Fig. 5.13. From the fringe pattern circled in Fig. 5.13 (a) and (b), it can be seen that there is a small particle, which is at a different height level from the micro-gear surface. Hence, the strike in Fig. 5.12 (a) may be a dust particle on the micro-gear. In the other two areas where spikes occur in Fig. 5.12 (b), no obvious particles were observed in the fringe patterns, thus the two spikes may caused by some other noise, which was eliminated by the CWT-based algorithm.

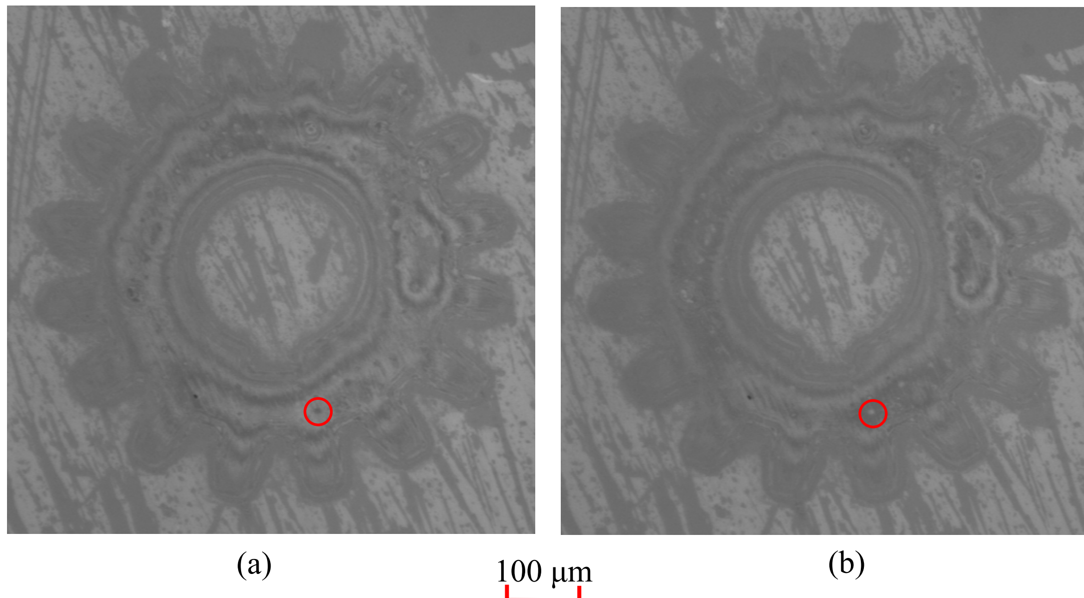

Fig. 5.13 White light interferometric fringe patterns of a micro-gear

5.2 Inspection of dual-layer structures

Measurement was also conducted on a coated silicon dual-layer wafer. The intensity response of a point on the wafer is shown in Fig. 5.14 (a) and a wavelet transform spectrum of the intensity response is shown in Fig. 5.14 (b). It is seen that the peaks of

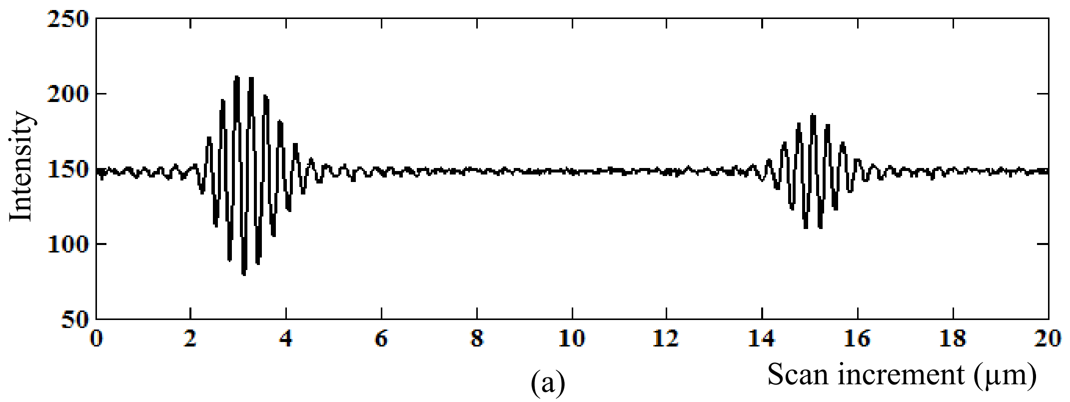

(a)

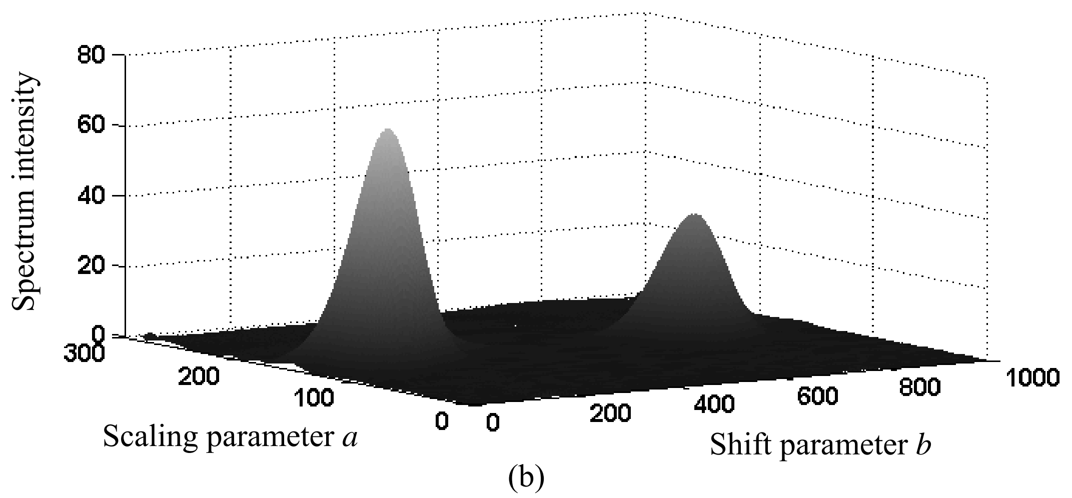

(b)

Fig. 5.14 (a) Intensity response of a point on a coated wafer; (b) Wavelet transform spectrum of the intensity response

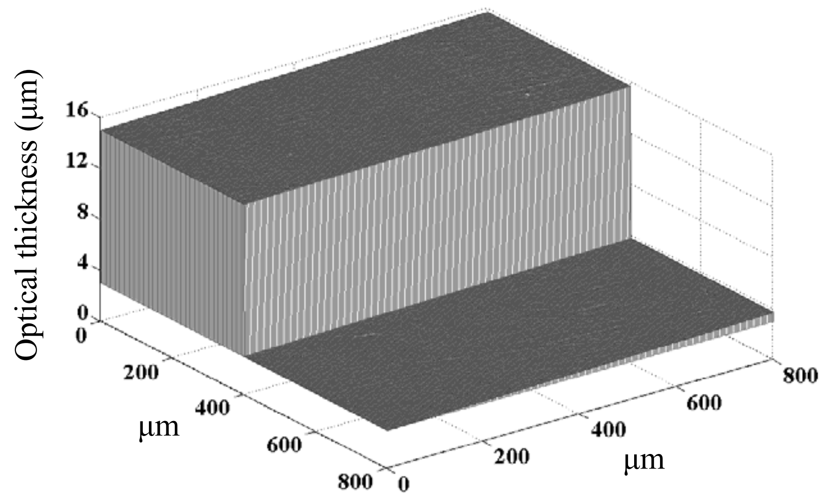

Fig. 5.15 Optical thickness of a coating layer on a wafer

the signal can be identified easily. The phase of each peak was then calculated using Eq. (3.35), and a more accurate peak value was identified with Eq. (3.36). The double envelopes indicate the position of the top and bottom surface of the coating. Hence, the optical thickness of the coating is obtained as shown in Fig. 5.15. The step in Fig. 5.15 is a virtual step, which was produced to illustrate the coating layer by removing part of coating with software during the reconstruction procedure. The higher level of the step indicates the top surface of the coating and the lower level indicates the interface between the coating and the substrate. From the average distance between

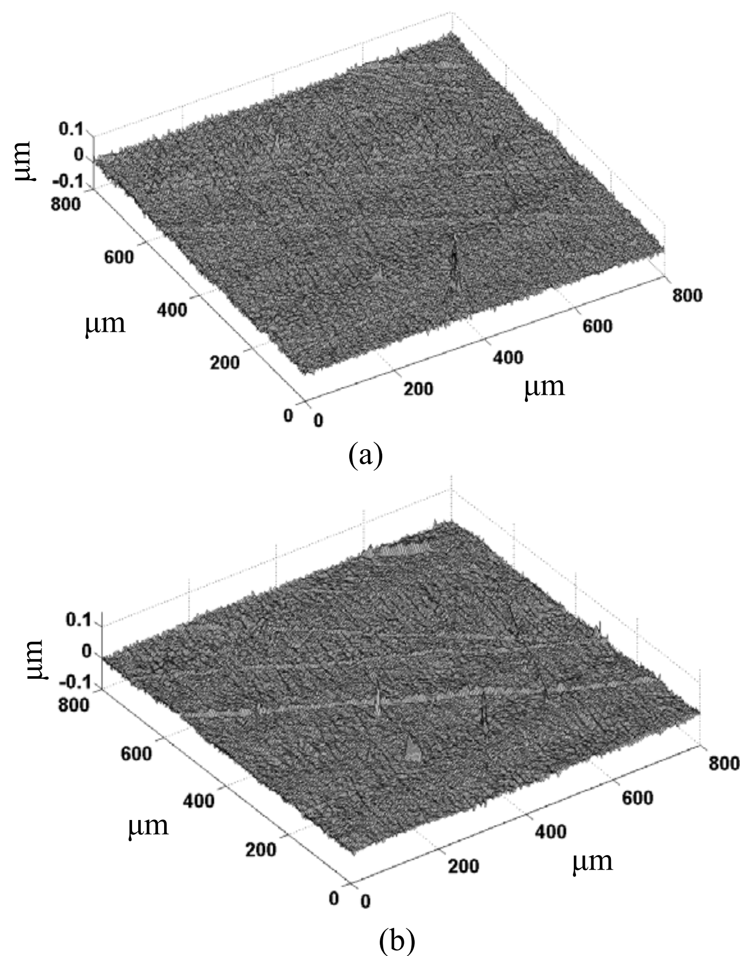

Fig. 5.16 (a) 3-D plots of top surface of coating; (b) interface between coating and substrate

the peaks (optical thickness of 11.89 μm) and the refractive index (1.65), the average thickness of the coating was determined as 7.21 μm. Based on the resulting fringe patterns, the surface roughness of the two layers was also studied using the proposed technique. Figure 5.16 (a) shows a 3-D profile of the top surface of the wafer coating and Fig. 5.16 (b) shows that of the interface between the coating and the second layer. From the results, the RMS roughness values of the wafer coating surface and interface are 0.03 μm and 0.06 μm respectively.

The proposed method was also employed to determine the thickness of a transparent micro-gear specimen (as shown in Fig. 5.17) which is essentially a dual-layer structure deposited on an opaque substrate. The diameter of the micro-gear is 500 μm and the grating line on the background is the surface texture of the opaque substrate. Since the refractive index of the transparent layer is larger than that of air, the optical path of light in the transparent layer of the micro-gear $(t+t')$ is longer than the thickness of the transparent layer (t) as shown in Fig. 5.18. The relationship

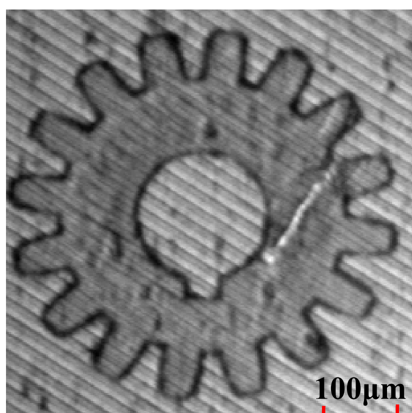

Fig. 5.17 A top view image of a transparent micro-gear

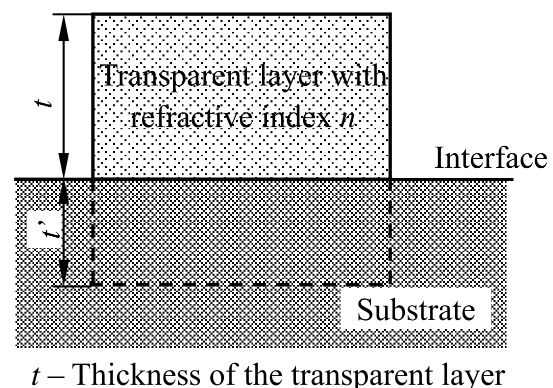

Fig. 5.18 A transparent layer on an opaque substrate

between the thickness of the transparent layer (t) and apparent thickness (t') due to the refractive index (n) of the transparent layer is given by

$$t + t' = nt \tag{5.1}$$

and the transparent layer thickness is given by

$$t = \frac{t'}{n-1} \tag{5.2}$$

From Fig. 5.19 which indicates the intensity response of a point on the micro-gear, the peak position can be determined. It is noted that the intensity distribution contains only one fringe envelope. Real-time fringe patterns imply that the fringe envelope is due to the interface between the micro-gear and substrate. This is because light

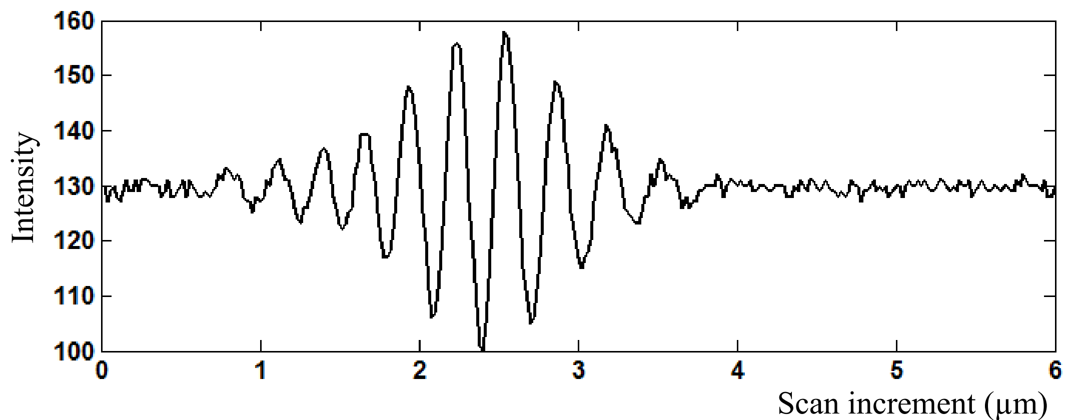

Fig. 5.19 Intensity response of a point on the micro-gear

reflected from the top surface of the micro-gear is too weak to be recorded due to the transparency of the micro-gear. Hence, only light reflected off the interface was recorded and the resulting intensity distribution is utilized to determine the thickness of the micro-gear. From the resulting intensity distribution, the apparent thickness (t') was obtained using the proposed algorithm, and the thickness of the gear is therefore obtained using Eq. (5.2). Figure 5.20 (a) shows a 3-D profile of the micro-gear and Fig. 5.20 (b) shows the apparent thickness (t') due to the refractive index of the micro-gear. Given the specified refractive index of 1.4 (the material of the gear is

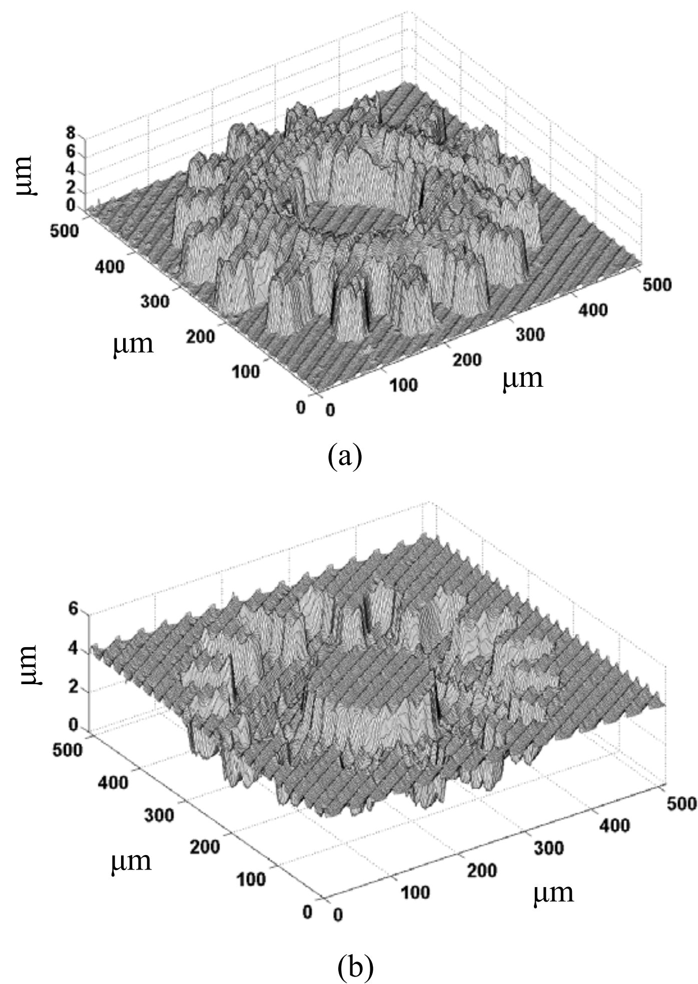

Fig. 5.20 (a) 3-D profile of a transparent micro-gear; (b) the apparent thickness due to the refractive index

a photosensitive polymer), the average thickness of the gear is about 5.54 μm. It is seen in Fig. 5.20 that grating lines are presented on the micro-gear specimen and substrate. This is due to the surface texture of the opaque substrate. The results of above two experiments show that the proposed method is a potential way to evaluate transparent/semi-transparent layered structures.

5.3 Micro-cantilever inspection

The proposed method was also employed to measure a micro-cantilever structure, which has two cantilevers as shown in Fig. 5.21. The micro-cantilevers were

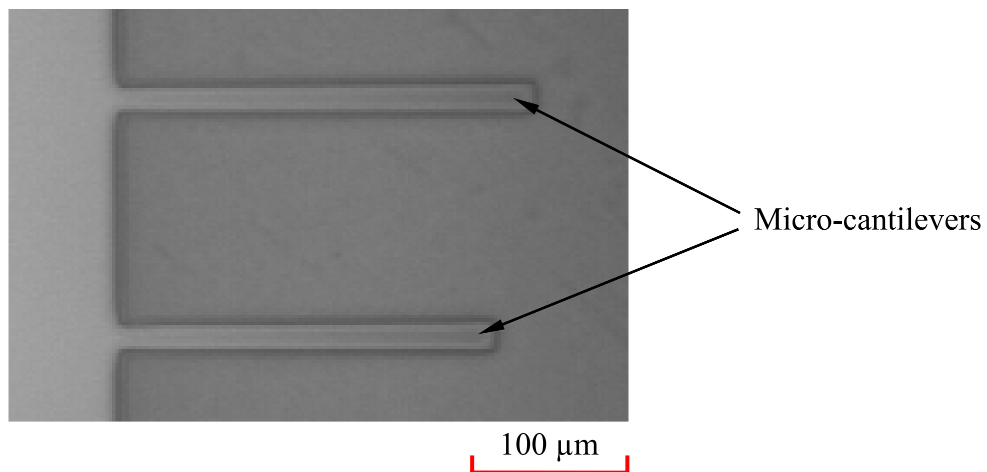

Fig. 5.21 Top view of a micro-cantilever structure

fabricated using etching technique and its material is silicon. The testing sample was measured by the proposed Mirau-layout system, which can implement the lighting arrangement as shown in Fig. 3.3 in Chapter 3. In the system, the illumination is able to bypass the cantilever and then reach the surface below the micro-cantilever to produce the object beam for the interference. Figure 5.22 shows an intensity response of a point on a tested micro-cantilever. It can be seen that there are three interference

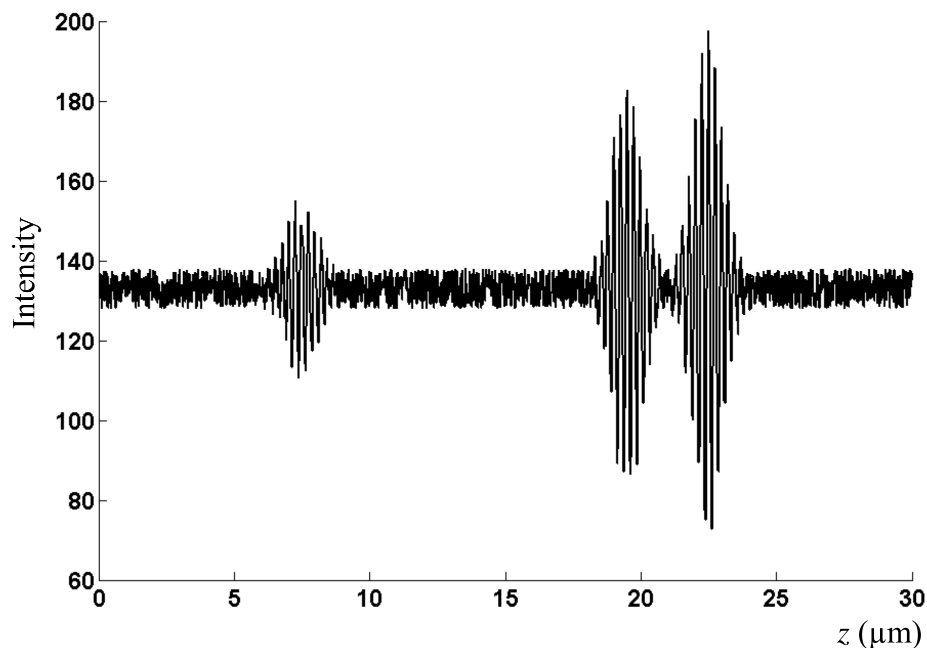

Fig. 5.22 Intensity response of a point on a micro-cantilever

zones along the scanning direction. From right to left, the first zone is due to the top surface of the micro-cantilever coating which is semi-transparent. The second is produced by the interface between the micro-cantilever and coating layer. Because of using a Mirau-type interferometer, the third interference zone, which is due to the surface under the micro-cantilever, was obtained. However, a Michelson interferometer cannot obtain signals from the obstructed surface. From the fringe patterns, we can obtain the 3-D top profile of the micro-cantilever, the coating thickness associated with refractive index of the coating layer and the 3-D profile of the surface under the micro-cantilever in one scanning. Figure 5.23 shows a reconstructed 3-D top profile of the micro-cantilever sample. There are two cantilevers in the investigated area. The steps on the two micro-cantilevers are virtual steps, which are produced to illustrate the coating layer by removing part of coating

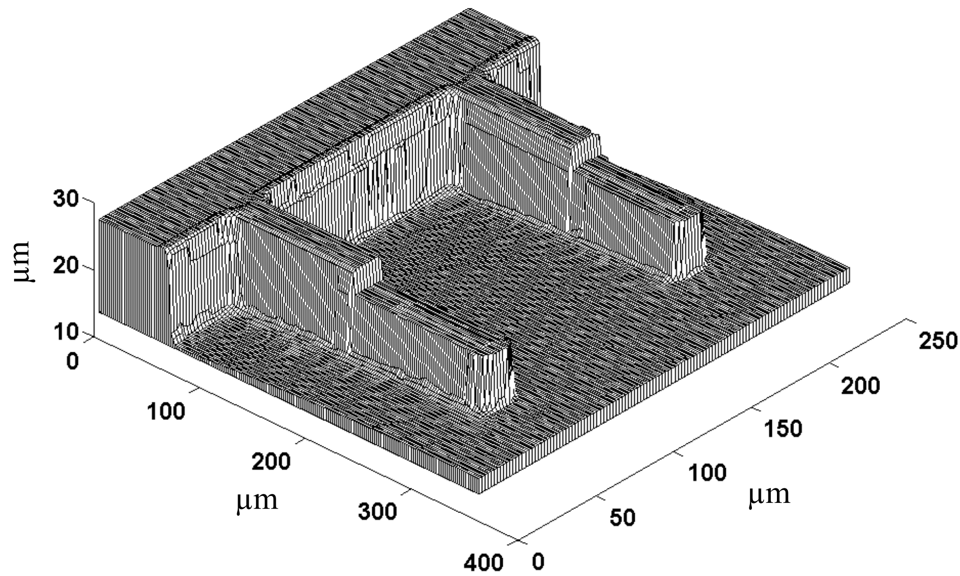

Fig. 5.23 A reconstructed 3-D top profile of micro-cantilevers

with software during the reconstructing procedure, the higher level of the step indicates the top surface of the coating and the lower level indicates the interface between the coating and micro-cantilever. From Fig. 5.23, it is seen that the substrate below the micro-cantilevers is obstructed completely by the micro-cantilevers. The obstructed surface and gap between the micro-cantilever and substrate cannot be seen directly from the top and hence the top profile reconstructed looks like a solid body. However, using the proposed Mirau-layout system, the substrate surface was readily reconstructed because the underneath substrate is able to be illuminated by the bypassing lighting. A 3-D plot of the substrate profile on a layer below the micro-cantilever at the top in Fig. 5.21 is shown in Fig. 5.24 (a). It can be seen that the results obtained using the proposed method agrees with that predicted based on the fabrication technique: etching from side to center would produces a ridge at the

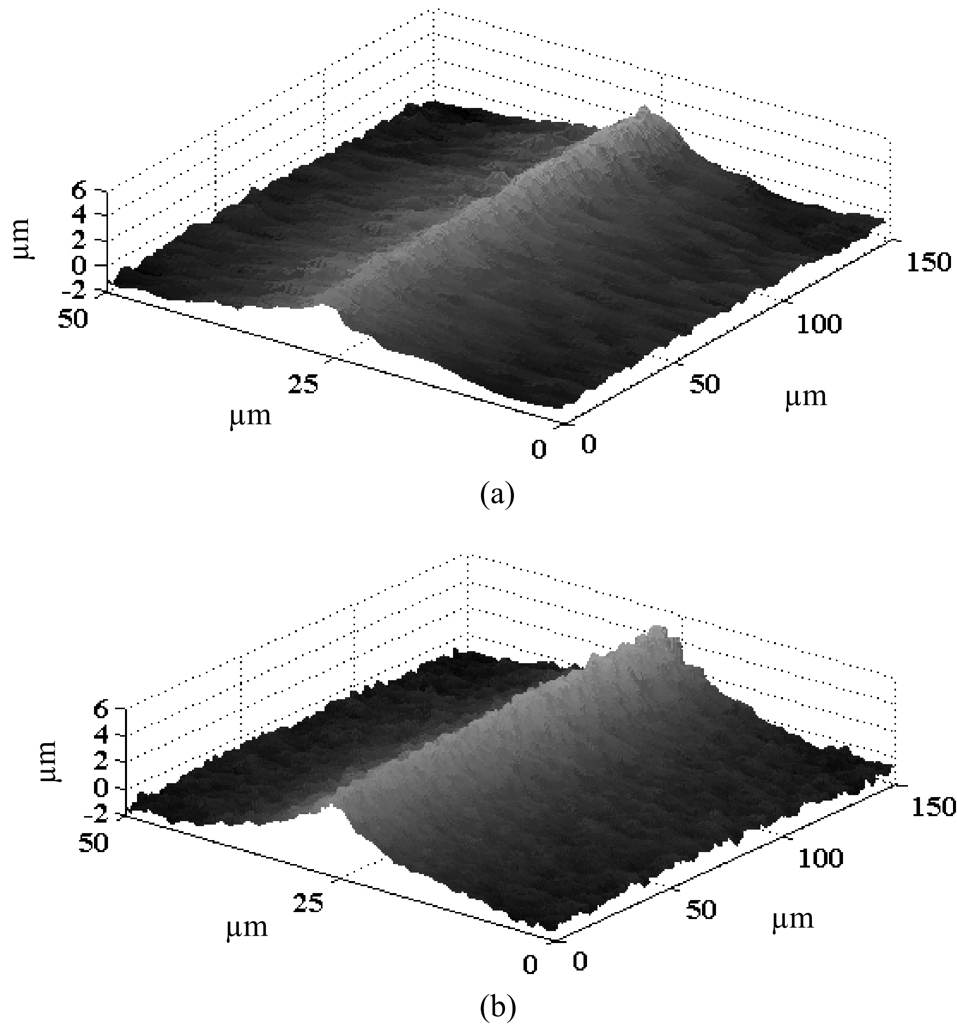

Fig. 5.24 (a) 3-D underneath profile obtained by proposed system; (b) 3-D underneath profile obtained by WYKO NT1100

central area under the micro-cantilever. To verify the results of substrate obtained with the proposed method, the obstructed substrate surface was measured by a commercial optical profiler WYKO NT1100 after the micro-cantilever was manually removed to expose the surface of interest and the results are shown in Fig. 5.24 (b). The results with a similar ridge verify the prediction of the substrate surface based on the fabrication technique. Figure 5.25 shows a cross-section of the profile at 125 µm from the fixed end of the cantilever obtained by the proposed method (solid line) and that obtained by the profiler. A maximum discrepancy of 25% is observed at the peak,

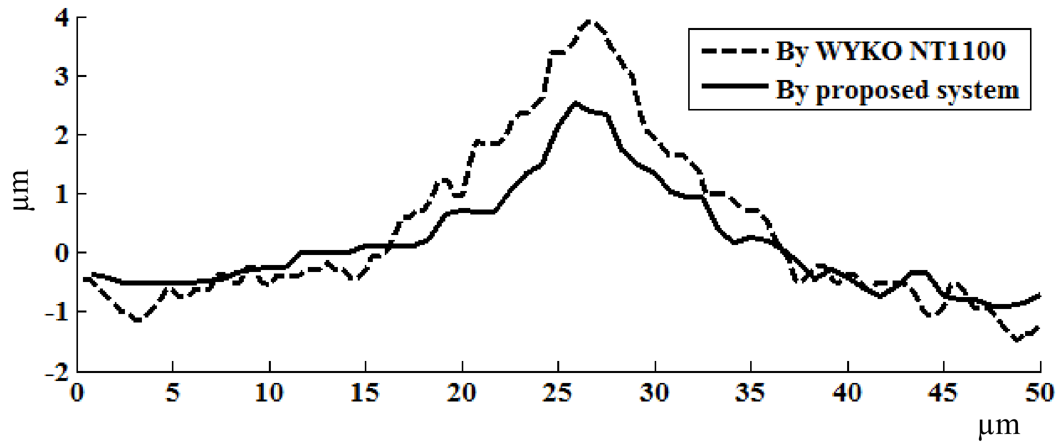

Fig. 5.25 A comparison of cross-sections of the underneath surface at 125 μm from the fixed end of the micro-cantilever

while the average discrepancy is 10%. The discrepancy is caused by a weak illumination at the peak region causing a low fringe contrast and hence inaccuracy in the processing of the fringe patterns. Subsequent process to remove the micro-cantilever in order to facilitate measurement by the commercial profiler also introduced inadvertent damage to the substrate surface, thus introducing additional inaccuracy. The experimental results show that the proposed method is effective to measure the top surface, the coating thickness and obstructed surface as well with high accuracy in one scanning time. The obstructed surface cannot be measured without damage using the profiler. However, the proposed method achieved non-destructive measurement of such a structure.

5.4 Surface quality evaluation

A standard roughness sample manufactured by end milling with an arithmetical mean roughness R_a of 0.4 μm and a ten-point mean roughness R_z of 1.92 μm specified by the manufacturer was evaluated using the proposed set-up. Figure 5.26 (a) shows a

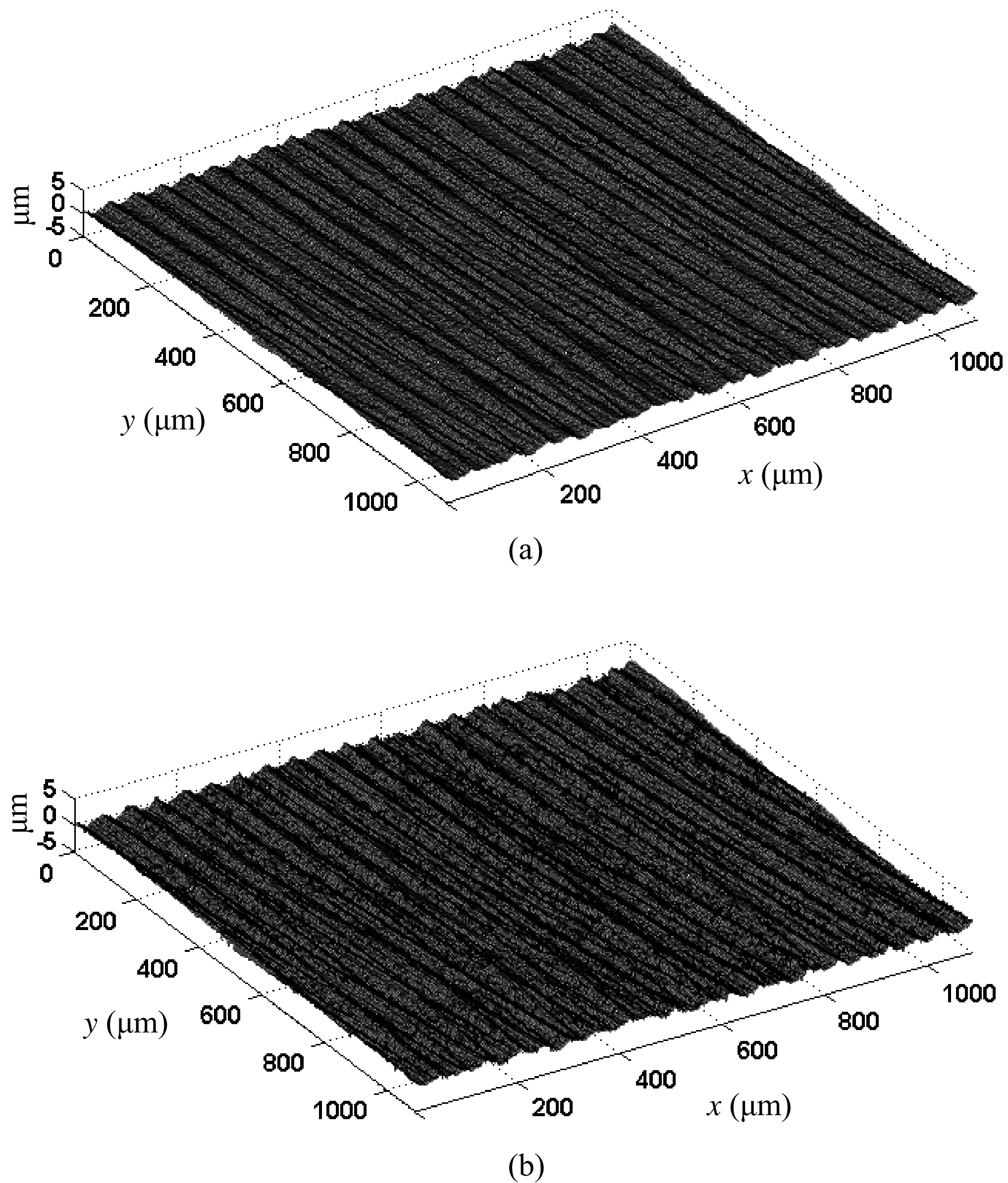

Fig. 5.26 (a) A 3-D surface reconstructed by CWT; (b) a 3-D surface reconstructed by envelope method

3-D plot of the surface reconstructed using the CWT method, while Fig. 5.26 (b) shows the surface profile using the envelope method based on Fourier transform. A cross-section of the surface at y = 542.5 μm is shown in Fig. 5.27. The arithmetical mean roughness (R_a) obtained by the CWT method is 0.41 μm, while that obtained by the envelope method is 0.43 μm. The discrepancy between the CWT method and

the specified value is 2.5%, while that of the envelope method is 7.5%. The ten-point mean roughness (R_z) calculated by CWT is 2.17 μm while that by the envelope-based method is 2.36 μm. The discrepancy between the CWT method and the specified value is 13%, while that of the envelope method is 23%. The CWT method utilizes the phase of a local fringe peak to determine the zero-OPD location and is not affected by the noise with frequencies close to the signal frequency because CWT can identify a single frequency of the signal, while the envelope method uses a global envelope to

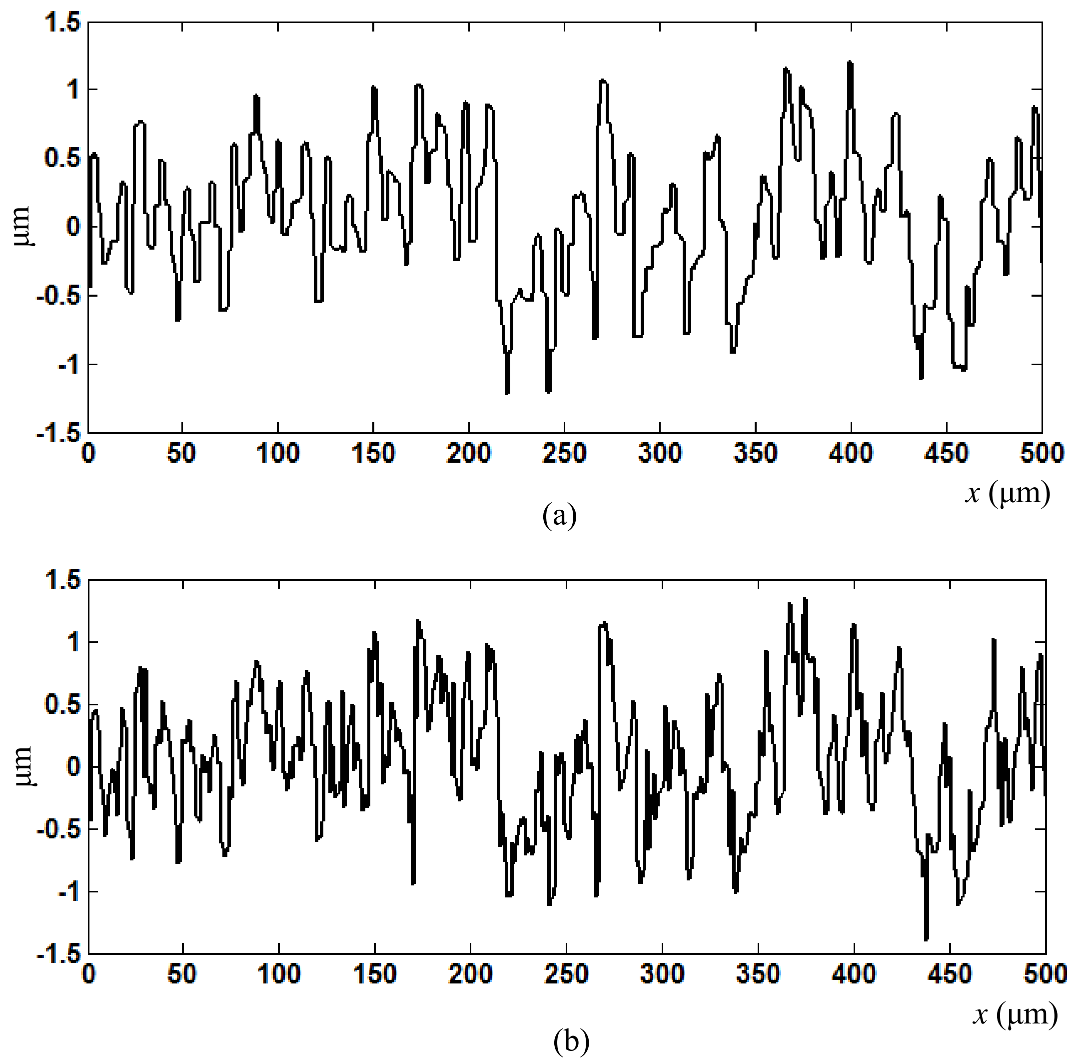

Fig. 5.27 (a) A cross-section of the surface by CWT; (b) a cross-section of the surface by envelope method

indentify the zero-OPD position and is affected by the noise with frequency close to signal frequency due to the filter window size in Fourier transform used in the envelope method. Thus, the CWT method gave better results than the envelope method. The discrepancy between the arithmetical mean roughness and the specified standard value is less than that between the ten-point mean roughness and the specified standard value. This might be caused by the selection of the sampling line over which the roughness was evaluated. Since the arithmetical mean roughness is the mean value of the variations along the whole sampling length, it is more stable in the whole surface. However, the ten-point mean roughness is calculated only from five peaks and five valleys over the sampling length, and hence its value depends more on the selection of the sampling line. Thus, the experimental result of R_a is very close to the standard value, while that of R_z is slightly away from the standard value. Another standard sample, which is produced using plane lapping with an arithmetical mean roughness R_a of 0.1 μm specified by manufacturer was also studied. The measured roughness values using the CWT and envelope methods are respectively 0.11 μm and 0.13 μm. The discrepancy between the CWT method and the specified value is 10%, while that of the envelope method is 30%. The CWT method gave a better result than the envelope method. This is consistent with the previous results. It is noted that the second result presents bigger discrepancy from the standard value than the first sample. This is because the specimen roughness is close to the noise level and hence the noise effect is more predominant.

A standard silicon carbide mirror (Veeco serial No.: RM04364) was measured

using the proposed system. The specified root mean square (RMS) value of the mirror surface is given as 0.125 nm by the manufacturer. A 3-D surface profile is plotted as shown in Fig. 5.28 (a). Since the test mirror surface is very flat, it could be considered as an ideal mirror surface, and hence the variation of the surface in Fig. 5.28 (a) could be regarded as the system noise of the measurement system. For comparison, another 3-D plot obtained using the envelope method is shown in Fig. 5.28 (b). Figure 5.29 shows a cross-section of the results. It is seen from the plot that the CWT method

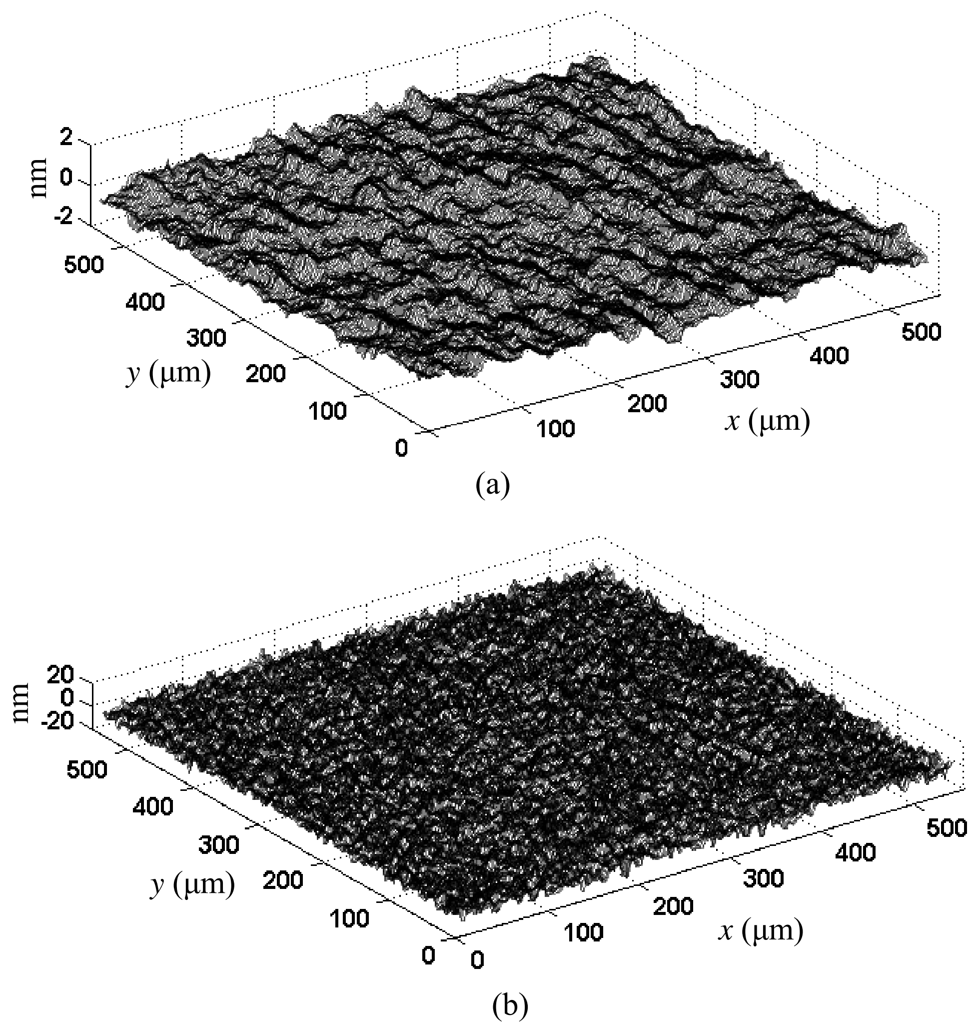

Fig. 5.28 (a) A 3-D plot of a mirror surface using CWT; (b) a 3-D plot of a mirror surface using envelope method

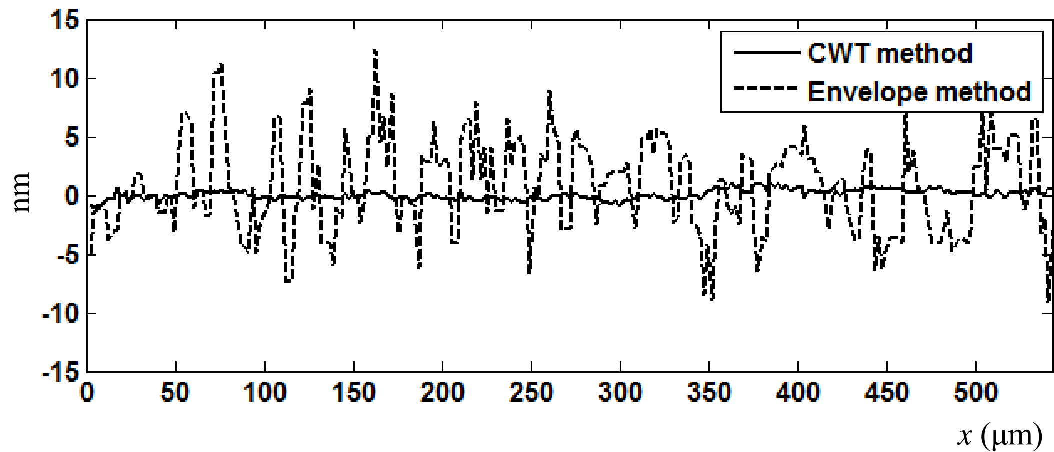

Fig. 5.29 Cross section of a standard mirror surface at y = 271.25 µm

produces much less system noise than the envelope method. The RMS value of the test surface obtained by the CWT method based on 10 measurements is 0.34 ± 0.11 nm, while that obtained by the envelope method is 4.04 ± 0.10 nm. It is seen that the CWT method could produce more accurate results and give a system noise of 0.34 ± 0.11 nm. This is because the CWT method uses a local fringe peak to improve the accuracy of identification of zero-OPD with less noise effect benefiting from the property of CWT. With a system noise of 0.34 ± 0.11 nm, variation of a surface of 0.45 nm is not able to be sensed by the system. Hence, this value could be considered as the resolution of the measurement system (smallest detectable variation).

5.5 Measurement uncertainty analysis

The accuracy of the proposed system is further evaluated with a measurement uncertainty analysis. The measurement using vertical scanning white light interferometry is essentially based on a surface height measurement. The samples of step height in section 5.1 were used in the measurement uncertainty analysis. A step

standard shown in Fig. 5.1 (a) is scanned and evaluated by the use of the proposed measurement system. From the results obtained, a measurement uncertainty analysis was conducted based on ISO guidelines (International Organization for Standardization, 1995). The uncertainty budget is classified as types A and B. Type A uncertainty is obtained from a series of measurements on the repeatability of the system. Based on a series of measurement n = 10, uncertainty due to random noise is classified as type A and is less than 1.1 nm.

The other parameters involve type B uncertainty. The mean wavelength of the light source was calibrated as $\lambda_0 = 625.3\,\text{nm} \pm 1.4\,\text{nm}$. Thus, assuming a rectangular distribution, the distributed standard uncertainty due to variations of the mean wavelength is given by $u_{(\lambda)} = 1.4/\sqrt{3} \times \pi / 4\pi = 0.2$ nm. The error due to the CCD camera is given by 0.02 fringes (Quan et al, 1997). Hence, the corresponding standard uncertainty using a rectangular distribution is evaluated as $u_{(N)} = 0.02/\sqrt{3} \times \lambda_0 / 2 = 4$ nm. The repeatability of the PZT stage is given by 0.02%. Using a rectangular distribution, the standard uncertainty due to the PZT stage is $u_{(P)} = 0.02\%/\sqrt{3} \times h = 0.012\% \times h$ nm (h is the relative surface height). The misalignment error introduced by collimation of the illumination in the experimental arrangement is less than 1°. Hence, the resulting Abbe error is calculated as $u_{(A)} = h \times (1 - \cos 1^\circ) = 0.00015 \times h$ nm. The phase difference φ uncertainty is contributed by the algorithm. It is obtained using an ideal signal given by

$$I(z) = 120 + 80 \times \exp\left[-\left(\frac{z - z_0}{l_c} \right)^2 \right] \cos\left[\frac{4\pi}{\lambda_0}(z - z_0) \right] \tag{5.3}$$

where z is the scan position and z_0 is the position of zero-OPD with constant values of $z_0 = 5$ μm, $l_c = 1$ μm and $\lambda_0 = 625.3$ nm. Prescribed phase values are retrieved using the CWT method, and the difference between the retrieved and the proscribed phase values is shown in Fig. 5.30. The mean value of the phase difference as shown

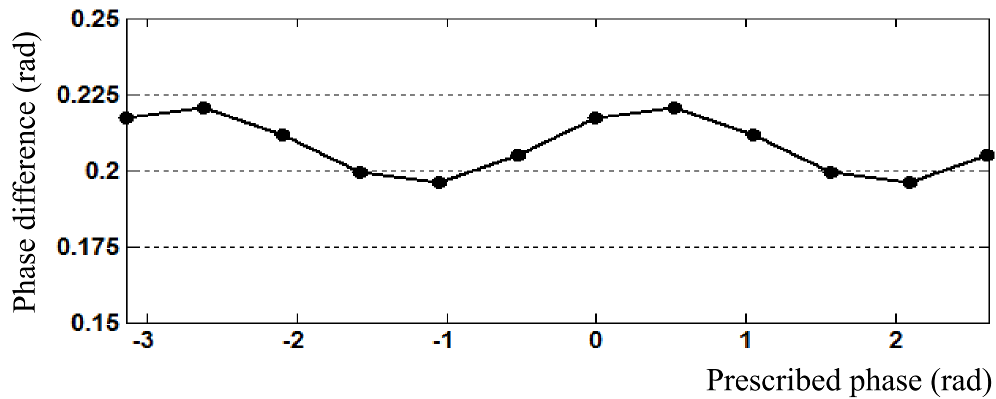

Fig. 5.30 Difference between the retrieved and prescribed phase values

in Fig. 5.30 is 0.2082 rad with a standard deviation of 0.0027 rad. Assuming a rectangular distribution, based on Eq. (3.27) the standard uncertainty is given by $u_{(\varphi)} = 0.0027/\sqrt{3} \times \lambda_0 / 4 = 0.08$ nm.

The main sources of uncertainty in the system and their contribution to the combined measurement uncertainty are shown in Table 5.2. According to ISO guidelines, the combined standard uncertainty of the measurement is given by

$$u_c(h) = u_{c1}(h) + u_{c2}(h) \tag{5.4}$$

where $u_{c1}(h) = \left(\sum_i u_i^2(h)\right)^{1/2}$ indicates the relative standard uncertainty and $u_{c2}(h) = \left(\sum_j u_j^2(h)\right)^{1/2}$ indicates the absolute standard uncertainty, $u_i(h)$ and $u_j(h)$ are respectively components of relative and absolute standard uncertainty. The combined standard uncertainty of the measurement is obtained as $u_c(h) = 0.02\% \times h + 4$ nm. The effective degree of freedom of the combined standard uncertainty is given by $DOF = u_c(h) / [u_i(h)/(n-1)] > 109$. For a level of confidence of approximately 95%, coverage factor *k* = 2, the expanded measurement uncertainty of the system is given by $U(h) = ku_c(h) = \pm(0.04\% \times h + 8)$ nm. Hence, the expanded measurement uncertainty of the step height as shown in Fig. 5.1 (a) is given by $U = \pm(0.04\% \times 1796.1 + 8) = \pm 8.72$ nm and the average step height is 1796 ± 9 nm.

The measurement uncertainty of the step height shown in Fig. 5.1 (b) was also studied. The uncertainty type B does not change since the measurement was carried out using the same system. Based on 10 time measurements, type A uncertainty is less than 2.7 nm. The combined standard uncertainty of the measurement is obtained as $u_c(h) = 0.02\% \times h + 4.8$ nm. The effective degree of freedom of the combined standard uncertainty is given by $DOF = u_c(h) / [u_i(h)/(n-1)] > 18$. For a level of confidence of approximately 95%, coverage factor *k* = 2, the expanded measurement uncertainty of the system is given by $U(h) = ku_c(h) = \pm(0.04\% \times h + 9.6)$ nm. The expanded measurement uncertainty of the step height as shown in Fig. 5.1 (b) is given by $U = \pm(0.04\% \times 23501.3 + 9.6) = \pm 19$ nm and the average step height is 23501 ± 19 nm.

Table 5.2 A summary of standard uncertainty components

Source of uncertainty	Type	Uncertainty value	Probability distribution	Coverage factor	Standard uncertainty $u_i(H)$	DOF
Short-term measurement repeatability	A	0.00211μm	Normal	1	1.1 nm	10
Wavelength tolerance	B	1.4 nm	Rectangular	$\sqrt{3}$	0.2 nm	7
Fringe fraction	B	0.02 fringe	Rectangular	$\sqrt{3}$	4 nm	∞
Uncertainty due to PZT stepping	B	0.02%	Rectangular	$\sqrt{3}$	0.012%	∞
Uncertainty due to phase calculation	B	0.0027 rad	Rectangular	$\sqrt{3}$	0.08 nm	11
Misalignment induced error	B	1°	Normal	1	$0.00015 \times H$ nm	∞
Combined uncertainty	-	-	Normal	-	$(0.02\% \times H + 4)$ nm	> 109
Expanded uncertainty	-	-	Normal	2	$(0.04\% \times H + 8)$ nm	∞

The lamellar grating was also investigated in uncertainty analysis. The type A uncertainty is given by 0.002 μm based on 14 time measurements. The combined standard uncertainty of the measurement is obtained as $u_c(h) = 0.02\% \times h + 0.0045$ μm. The effective degree of freedom of the combined standard uncertainty is given by $DOF = u_c(h) / [u_i(h)/(n-1)] > 28$. For a level of confidence of approximately 95%, coverage factor k = 2, the expanded measurement uncertainty of the system is given by $U(h) = ku_c(h) = \pm(0.04\% \times h + 0.009)$ μm. The expanded measurement uncertainty of the height between points A and B as shown in Fig. 5.4 is given by $U = \pm(0.04\% \times 19.337 + 0.009) = \pm 0.017$ μm and the average step height is 19.34 ±

0.02 μm.

5.6 Color fringe analysis

In the simulation, a prescribed step was generated using software and Fig. 5.31 (a) shows a 3-D plot of the prescribed step reconstructed from computer-generated fringe patterns (channel R, G and B) with random noise of 10 percent of maximum intensity. The prescribed height of the step is 10 nm. Results obtained from a channel (R) are also shown in Fig. 5.31 (b). Results reconstructed by phase-crossing (Pawlowdki et al, 2005) are shown in Fig. 5.31 (c). It is seen that the results obtained by the proposed method show a better definition of the profile with less noise. A cross-section of the profile in Fig. 5.31 is shown in Fig. 5.32 and it is seen that the proposed method shows a clear reconstructed step height well. The measured mean step height is 9.92 nm compared with the prescribed step height of 10 nm. The discrepancy between the measured value and the prescribed value is 0.8%, while gray fringe analysis show a discrepancy of 5% and the phase-crossing method shows that of 3%. Since more information of fringe patterns were employed in color fringe analysis than in gray fringe analysis, the proposed method gives a better performance in the data processing. Phase-crossing method utilized two channels to identify zero-OPD position, while the proposed method employed a third channel, with which the measurement accuracy was improved. The influence of noise level on the measured mean step height is also shown in Fig. 5.33. It can be seen that the mean step height is not significantly affected by the noise level. This is because the mean of random noise is

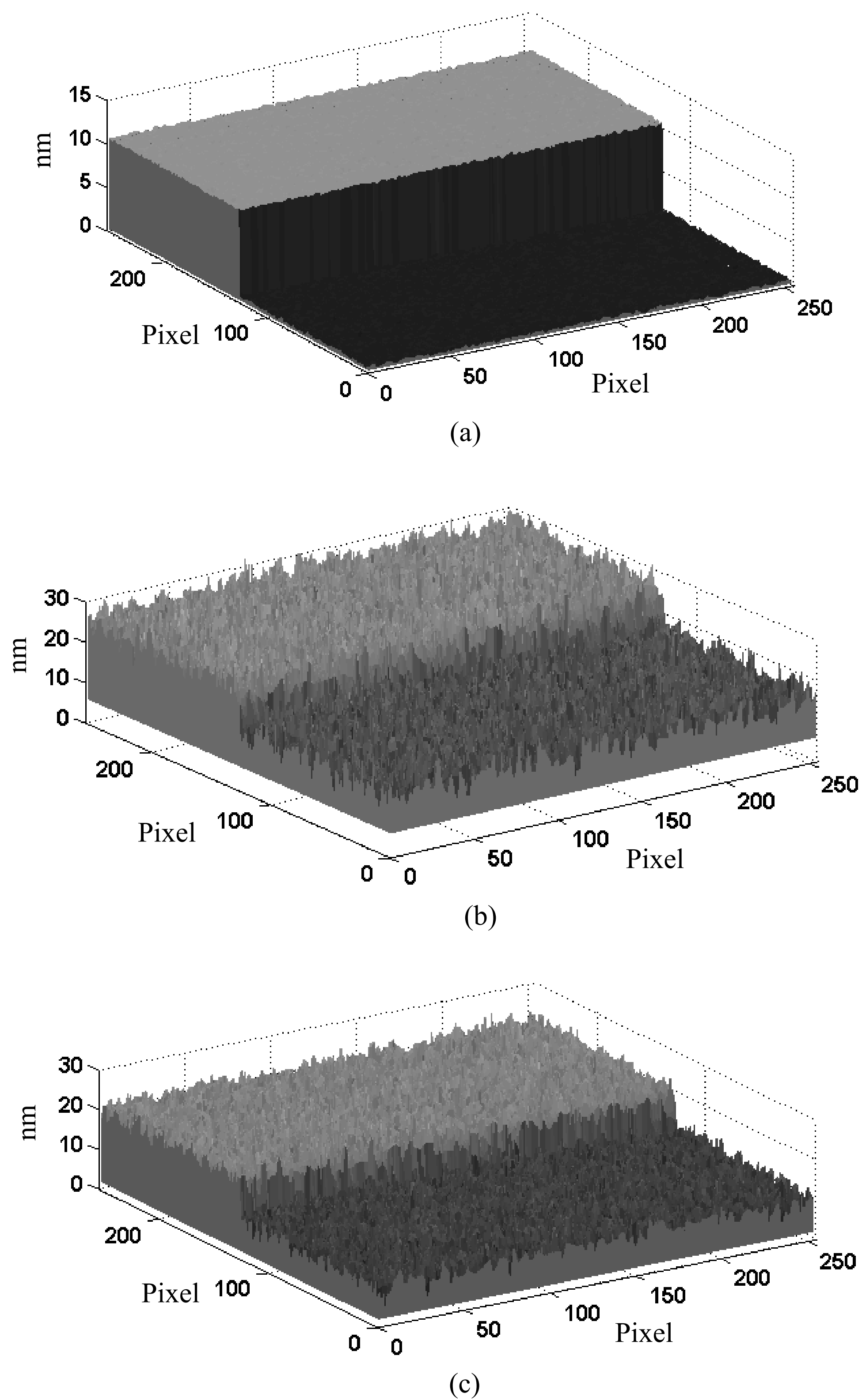

Fig. 5.31 (a) 3-D plot by proposed method; (b) 3-D plot by gray fringe analysis; (c) 3-D plot by phase-crossing method

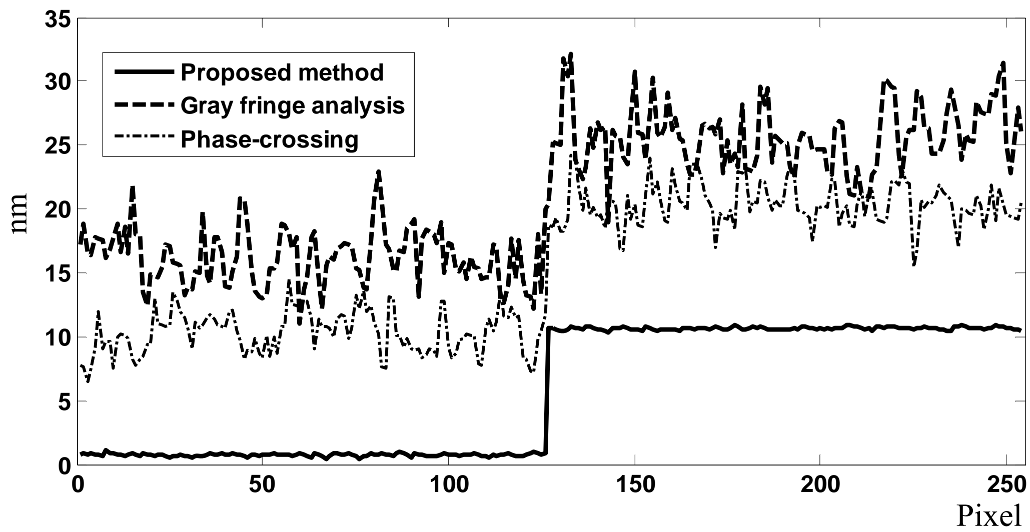

Fig. 5.32 Cross-section of reconstructed step profile

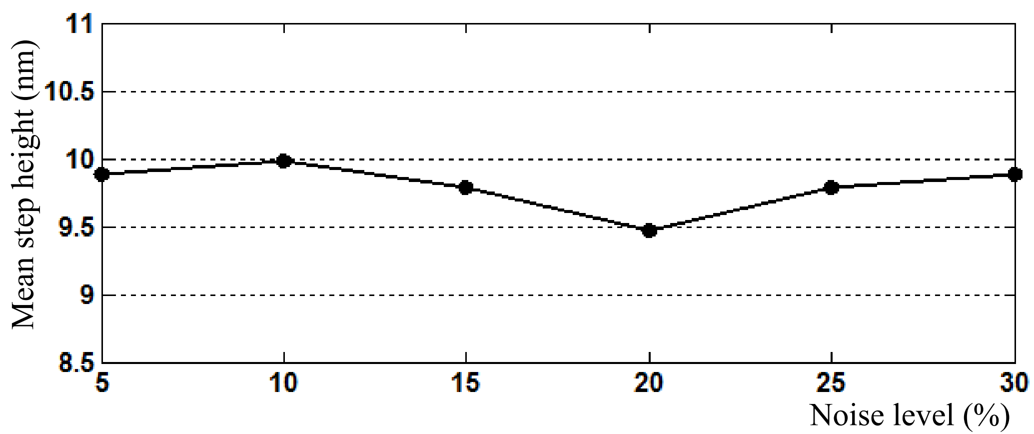

Fig. 5.33 Influence of noise level on mean step height

approximately taken zero in the computation, and hence the noise level does not have much influence on the mean step height. Because different sets of random noise was applied to different sets of fringe patterns to produce different noise levels, the means of random noise for different sets of fringe patterns are slightly different, which might cause the decrease and increase trend around noise level of 20% in Fig. 5.33. Figure 5.34 shows a standard deviation of the surface variation in terms of the noise level. It can be seen that the standard deviation increases linearly with the noise level.

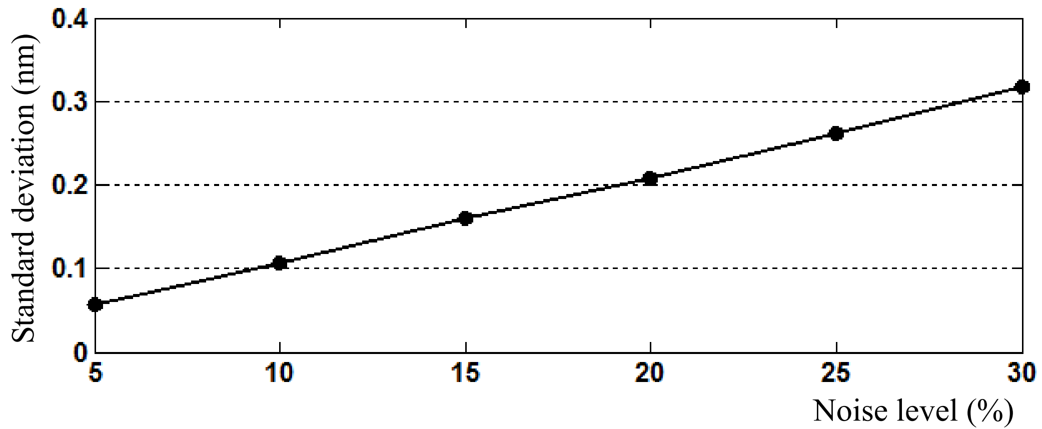

Fig. 5.34 Influence of noise level on standard deviation of surface variation

However, a standard deviation of 0.32 nm is still achieved at a high noise level using the proposed method. Hence, the proposed algorithm is feasible for analyzing a color fringe pattern obtained using vertical scanning white light interferometry for 3-D surface profiling.

5.7 Discussion on time consumption of algorithms

As a complex Morlet wavelet was chosen as the mother wavelet of CWT, the CWT coefficients of a signal $s(t)$ is given by

$$W(a,b) = \frac{1}{\sqrt{a}} \int_{-\infty}^{\infty} s(t) \exp\left[-\frac{(t-b)^2}{2a^2} \right] \exp\left[-j\frac{\omega_0}{a}(t-b) \right] dt \tag{5.5}$$

In the algorithms proposed for white light interference fringe analysis, the CWT was firstly applied to the intensity response of an arbitrary point on a test object. The ridge of the CWT coefficients was identified and then the mean wavelength was calibrated using the scaling parameter a_0 on the ridge. After the calibration, the CWT

coefficients for the intensity responses of the rest of the points on a test object is given by

$$W(a_0,b)=\frac{1}{\sqrt{a_0}}\int_{-\infty}^{\infty}s(t)\exp\left[-\frac{(t-b)^2}{2a_0{}^2}\right]\exp\left[-j\frac{\omega_0}{a_0}(t-b)\right]dt \qquad (5.6)$$

and then simplified as

$$W(b)=\frac{1}{\sqrt{a_0}}\int_{-\infty}^{\infty}s(t)\exp[-C(t-b)(t-b)]\exp[-j\omega_c(t-b)]dt \qquad (5.7)$$

For comparison, the envelope method based on Fourier transform consists of Fourier transform

$$F(\omega)=\frac{1}{\sqrt{2\pi}}\int_{-\infty}^{\infty}s(t)\exp(-j\omega t)dt \qquad (5.8)$$

and its inverse transform

$$s(t)=\frac{1}{\sqrt{2\pi}}\int_{-\infty}^{\infty}F(\omega)\exp(j\omega t)d\omega \qquad (5.9)$$

It can be seen that for the same length (N) of signal data the CWT-based algorithm implement $3N$ subtract operations and $3N$ multiply operations more for each

coefficient than the envelope method based on Fourier transform. In addition, the CWT-based algorithm has a wavelength self-calibration routine, while the envelope method does not. In the self-calibration, 30 increments were applied to the scaling parameter a to search the signal frequency. That means the CWT-based method has 30 computations of Eq. (5.7) more. These extra computations may cause different extra time consumptions for different arithmetic logic unit (ALU) of different computers. Using the computer (Dell 2.66GHz with 512MB memory) used in the work, the CWT-based algorithm needed 2-3 times computation time more than the envelope method.

CHAPTER SIX

CONCLUSIONS AND RECOMMENDATIONS

6.1 Concluding remarks

A new algorithm based on CWT was developed for monochrome fringe analysis in vertical scanning white light interferometry. Peaks of intensity response are identified based on the modulus of CWT coefficients on the ridge in the time-scale plane. The novelty of the technique lies in the identification of zero-OPD position using the phase of the peak retrieved by the CWT method. The main advantage of the method is the denoising and automatic frequency selection of the wavelet method which is more effective for analyzing noisy fringe patterns and its non-dependency on the wavelength of the reflected light beam thus leading to improvement of resolution and accuracy in the measurement. In addition, frequency auto-selection of the CWT method enables accurate applications of white light interferometric measurement to surfaces with absorptive material to the spectrum. The method is able to achieve a resolution of better than 0.5 nm with sacrifice of the computation time.

A new algorithm based on CWT for color fringe analysis was also proposed for analysis of white light interferograms. Three channels (R, G and B) are used in the data analysis for reconstruction of 3-D profiles of micro-components. A new technique based on the absolute values of phase difference between three channels was also developed for zero-order fringe identification. This method which is based on phase retrieval results in more accurate results compared with methods based on

coherence envelope retrieval. Simulations conducted show that this method is feasible for analyzing a color fringe pattern obtained using vertical scanning white light interferometry for 3-D surface profiling.

A unique 3-D measurement system based on a conventional microscope is also developed. The system can readily be interchanged between Michelson and Mirau set-up for different applications. With a high-precision PZT nano-positioning stage, a vertical scanning accuracy of 1 nm can be achieved.

Dual-layer structures were also investigated using the system. The system is able to provide whole-field information of a dual-layer structure including 3-D surface profiles and layer thickness. In addition, the surface roughness was also investigated. The results indicate that the technique has a good potential for measurement in the range of several microns to hundreds of microns with nanometer resolution. The successful measurement of the dual-layer structures indicates that the proposed method may similarly be applied to multiple-layer structures, which are widely used in MEMS.

Using the proposed special illumination arrangement, a surface obstructed by an opaque structure can be inspected. A 3-D profile of an obstructed substrate was detected using the proposed system with an accuracy of sub-micron. This shows the potential for non-destructive inspection of an obstructed surface in micro-components. The application however has its inherent limitation in that the aspect ratio of the micro-structure to be measured is limited by the numerical aperture of the illumination system.

6.2 Recommendations for future work

In this thesis, a new algorithm combining color fringe pattern analysis with CWT was developed. However, due to the limitation of equipment, no experiments were carried out to verify the algorithm, though simulations were conducted. Therefore, experimental work should be implemented in the future. For color fringe analysis, a 3-CCD color camera should be employed to record fringe patterns instead of a single-CCD color camera.

In the work, dual-layer structures were inspected using the proposed method. Theoretically, this method is also applicable to multi-layer structures. Thus, inspection of multi-layer structures could be a part of the future work. In addition, if a penetrative light, like infrared light, was used as an illumination source, inspection of opaque layers would be possible.

The current method could only obtain physical thicknesses of a layered structure if the refractive index is known. Possible future work includes determination of structure thickness independent on the refractive index. A combination of spectrum analysis with white light interferometry is a possible approach for this problem, since spectrum analysis can obtain the refractive index, which is used to determine the thickness in white light interferometry.

REFERENCES

1. Abbate, A., C.M. DeCusatis and P.K. Das., Wavelets and subbands: fundamentals and applications, Boston: Birkhäuser, 2001.

2. Alexander, B.F., 3D shape measurement by active triangulation using an array of coded light stripes, Proc. SPIE, 850, pp199-205. 1987.

3. Balasubramanian, N., Optical system for surface topography measurement, US Patent #4, 340, 306 July 1982.

4. Berger, E., W. Linden, V. Dose, M.W. Ruprecht and A.W. Koch, Approach for the evaluation of speckle deformation measurement by application of the wavelet transformation, Appl. Opt., 36(29), pp7455-7460. 1997.

5. Born, M. and E. Wolf, Principles of Optics, 6th edition, Pergamon Press, pp316-323. 1980.

6. Bosseboeuf, A. and S. Petitgrand, Characterization of the static and dynamic behaviour of M(O)EMS by optical techniques: status and trends, J. Micromech. MicroEng., 13, ppS23-S33. 2003.

7. Bowe, B. and V. Toal, A white light interferometer for surface profiling, Proc. of the Applied Optics Division Conference of the Institute of Physics Reading, pp16-19. 1996.

8. Caber, P.J., Interferometric profiler for rough surface, Appl. Opt., 32(19), pp3438-3441. 1993.

9. Caspi, D., N. Kiryati and J. Shamir, Range imaging with adaptive color structured light, IEEE Trans. Pattern Anal. Mach. Intell., 20(5), pp470-480. 1998.

10. Chen, F., G.M. Brown, and M. Song, Overview of three-dimensional shape measurement using optical methods, Opt. Eng., 39, pp10-20. 2000.

11. Chen, H.J., J. Zhang, D.J. Lv and J. Fang, 3-D shape measurement by composite pattern projection and hybrid processing, Optics Express, 15(19), pp12318-12330. 2007.

12. Chen, W.J., P. Bu, S. Zheng and X. Su, Study on Fourier transforms profilometry based on bi-color projecting, Optics & Laser Technology, 39, pp821-827. 2007.

13. Cheng, Y. and J.C. Wyant, Two-wavelength phase shifting interferometry, Appl. Opt., 23(24), pp4539-4543. 1984.

14. Cheng, Y. and J.C. Wyant, Multi-wavelength phase-shifting interferometry, Appl. Opt., 24(6), pp804-807. 1985.

15. Cherbuliez, M., P. Jacquot and X.V. Lega, Wavelet processing of interferometric sinal and fringe patterns, Proc. SPIE, 9813, pp692-702. 1999.

16. Chim, S.S.C. and G. S. Kino, Three-dimensional image realization in interference microscopy, Appl. Opt., 31(14), pp2550-2553. 1992.

17. Creath, K., Phase-shifting speckle interferometry, Appl. Opt., 24(18), pp3053-3058. 1985.

18. Daubechies, I. Ten lectures on wavelets, Society for Industrial and Applied Machenics, Philadelphia, 1992.

19. Davidson, M., K. Kaufman and I. Mazor, The coherence probe microscope, Solid State Technol., 30, pp57-59. 1987.

20. Dawson, T.G. and T.R. Kurfess, Qualification of tool wear using white light interferometry and three-dimensional computational metrology, International J. of Machine Tools & Manufacture, 45, pp591-596. 2005.

21. Deck, L., and P. Groot, High-speed noncontact profiler based on scanning white-light interferometry, Appl. Opt., 33(31), pp7334-7338. 1994.

22. Desse, J.-M., Three-color differential interferometry, Appl. Opt., 36(28), pp7150-7156. 1997.

23. Desse, J.-M., F. Albe and J.-L. Tribillon, Real-time color holographic interferometry, Appl. Opt., 41(25), pp5326-5333. 2002.

24. Desse, J.-M., P. Picart and P. Tankam, Digital three-color holographic interferometry for flow analysis, Optics Express, 16(8), pp5471-5480. 2008.

25. Djinovic, Z., M. Tomic and A. Vujanic, Nanometer scale measurement of wear rate and vibration by fiber-optic white light interferometry, Sensors and Actuators A, 123-124, pp92-98. 2005.

26. Fang, Q. and S. Zheng, Linearly coded profilometry, Appl. Opt., 36, pp2401-2407. 1997.

27. Federico, A. and G.H. Kaufmann, Eveluation of the continuous wavelet transform method for the phase measurement of electronic speckle pattern interferometry fringes, Opt. Eng., 41(12), pp3209-3216. 2002.

28. Fu, Y., C.J. Tay, C. Quan and L.J. Chen, Temporal wavelet analysis for deformation and velocity measurement in speckle interferometry, Opt. Eng., 43(11), pp2780-2787. 2004.

29. Fujita, K., O. Nakamura, T. Kaneko, M. Oyamada, T. Takamstsu and S. Kawata, Confocal mutliphoton excitation microscope with microlens and pinhole arrays, Coptics Communication, 174, pp7-12. 2000.

30. Fukatsu, H. and K. Yanagi, Development of an optical stylus displacement sensor for surface profiling intruments, Microsyst. Technol., 11, pp582-589. 2005.

31. Gdeisat, M.A., D.R. Burton and M.J. Lalor, Spatial carrier pattern demodulation by use of a two-dimensional continuous wavelet transform, Appl. Opt., 45(34), pp8722-8732. 2006.

32. Geng, Z., Rainbow three-dimensional camera: new concept of high-speed three-dimensional vision systems, Opt. Eng., 35(2), pp376-383. 1996.

33. Groot, P. and L. Deck, Three-dimensional imaging by sub-Nyqusit sampling of white-light interferograms, Optics Letters, 18(17), pp1462-1464. 1993.

34. Groot, P. and L. Deck, Surface profiling by analysis of white-light interferograms in the spatial frequency domain, J. of Modern Optics, 42, pp389-401. 1995.

35. Groot, P., X.C. Lega, J. Kramer and M. Turzhitsky, Determination of fringe order in white-light interference microscopy, Appl. Opt., 41(22), pp4571-4578. 2002.

36. Groot, P. and X.C. Lega, Vavle cone measurement using white light interference microscopy in a spherical measurement geometry, Opt. Eng., 42(5), pp1232-1237. 2003.

37. Hariharan, P. and M. Roy, White-light phase-stepping interferometry: measurement of the fractional interference order, J. of Modern Optics, 42(11), p2357-2360. 1995.

38. Häusler, G. and D. Ritter, Parallel three-dimensional sensing by color-coded triangulation, Appl. Opt., 32, pp7164-7169. 1993.

39. Hecht, E., Optics, 4th Edition, Addison-Wesley, 2002.

40. Hirabayashi, A., H. Ogawa and K. Kitagawa, Fast surface profiler by white light interferometry by use of a new algorithm based on sampling theory, Appl. Opt., 41(23), pp4876-4883. 2002.

41. Hissmann, M. and F.A. Hamprecht, Bayesian surface estimation for white light interferometry, Opt. Eng., 44(1), pp015601. 2005.

42. Hu, C.-H. and Y.-W. Qin, Digital color encoding and its application to the moiré technique, Appl. Opt., 36(16), pp3682-3685. 1997.

43. Huang, P.S., Q.Y. Hu, F. Jin and F.P. Chiang, Color-encoded digital fringe projection technique for high-speed three dimensional surface contouring, Opt. Eng., 38(6), pp1065-1071. 1999.

44. Huang, P.S., C.P. Zhang and F.P. Chiang, High-speed 3-D shape measurement based on digital projection. Opt. Eng., 42, pp163-168. 2003.

45. Hwang, Y.-M., S.-W. Yoon, J.-H. Kim, S. Kim and H.-J. Pahk, Thin-film thickness profile measurement using wavelet transform in wavelength-scanning interferometry, Optics and Lasers in Engineering, 46, pp179-184. 2008.

46. International Organization for standardization. Guide to the Expression of Uncertainty in Measurement. Geneva: ISO 1995.

47. Jing, Y., J. Luo, X. Yi and X. Gu, Design and evaluation of PZT thin-film micro-actuator for hard disk drives, Sensors and Actuators A, 116, pp329-335. 2004.

48. Kadooka, K., K. Kunoo, N. Uda, K. Ono and T. Nagayasu, Strain analysis for moiré interferometry using the two-dimensional continuous wavelet transform, Experimental Mechanics, 43(1), pp45-51. 2003.

49. Kakino, Y., A. Matsubara, I. Yamaji, K. Matuda, H. Nakagawa, T. Hirogaki and Y. Kita, In-situ measurement of grinding wheel surface topography (1st report) –

development of measuring system using laser stylus, Interternational Journal of the Japan Society for Precision Engineering, 31(4), pp273-277. 1997.

50. Kino, G.S. and S.S.C. Chim, Mirau correlation microscope, Appl. Opt., 29(26), pp3775-3783. 1990.

51. Koyuncu, I., J. Brant, A. Lüttge and M.R. Wiesner, A comparison of vertical scanning interferometry (VSI) and atomic force microscope (AFM) for characterizing membrane surface topography, J. of Membrane Science, 278, pp410-417. 2006.

52. Kuwamura, S and I. Yamaguchi, Wave-length scanning profilometry for real-time surface shape measurement, Appl. Opt., 36(19), pp4473-4482. 1997.

53. Larkin, K.G., Efficient nonlinear algorithm for envelope detection in white light interferometry, Journal of the Optical Society of America A, 13(4), pp832-843. 1996.

54. Lee, B.S. and T.C. Strand, Profilometry with a coherence scanning microscope, Appl. Opt., 29(26), pp3784-3788. 1990.

55. Li, J.F., X.Y. Su and L.R. Gou, An improved Fourier transform profilmetry for automatic measurement of 3-D object shapes, Opt. Eng., 29, pp1439-1444. 1990.

56. Li, X., Wavelet transform for detection of partial fringe pattern induced by defects in nondestructive testing of holographic interferometry and electronic speckle pattern interferometry, Opt. Eng., 39(10), pp2821-2827. 2000.

57. Livnat, A., O. Kafri and G. Erez, Hills and valleys analysis in optical mapping and its application to moiré contouring, Appl. Opt., 19, pp3396-3400. 1980.

58. Malacara, D., M. Servín and Z. Malacara, Interferogram analysis for optical testing, New York: Marcel Dekker, 1998.

59. Mallat, S., A wavelet tour of signal processing, 2nd edition, San Diego: Academic Press, 1997.

60. Massig, J.H., M. Pressler, A.R. Wegener and G. Gaida, Real-time confocal laser scan microscope for examination and diagnosis of eye in vivo, Appl. Opt., 33(4), pp690-694. 1994.

61. Mignot J. and C. Gorechi, Measurement of surface roughness: comparison between a defect-of-focus optical technique and the classical stylus technique,

Wear, 87, pp39-49. 1983.

62. Moench, W. and H. Zappe, Fabrication and testing of micro-lens arrays by all-liquid techniques, J. Opt. A: Pure Appl. Opt., 6, pp330-337. 2004.

63. Montgometry, P.C., D. Montaner, O. Manzardo, M. Flury and H.P. Herzig, The metrology of a miniature FT spectrometer MOEMS device using white light scanning interference microscopy, Thin Solid Film, 450, pp79-93. 2004.

64. O'Mahony, C., M. Hill, M. Brunet, R. Duane and A. Mathewson, Characterization of micromechanical structures using white-light interferometry, Meas. Sci. Technol., 14, pp1807-1814. 2003.

65. Odegard, J.E., G.H. Kaufmann and A. Davila, Wavelet-based methods for speckle noise reduction in tv holography fringes, Proc. Of the Applied Optics Divisional Conference of the Institute of Physics, pp251-256. 1996.

66. Olszak, A., Lateral scanning white-light interferometer, Appl. Optics. 39, pp3906-3913. 2000.

67. Olszak, A. and J. Schmit, High-stability white-light interferometry with reference signal for real-time correction of scanning errors, Opt. Eng., 42(1), pp54-59. 2003.

68. Park, M., and S. Kim, Direct quadratic polynomial fitting for fringe peak detection of white light scanning interferograms, Opt. Eng., 39, pp952-959. 2000.

69. Pawlowski, M.E., Y. Sakano, Y. Miyamoto and M. Takeda, Phase-crossing algorithm for white light fringe analysis, Optics Communications, 160, pp68-72. 2005.

70. Poilâne, C., Thickness measurement of nontransparent free films by double-side white light interferometry: calibration and experiments, Review of Scientific Instruments, 77, pp055102. 2006.

71. Polhemus, C., Two-wavelength interferometry, Appl. Opt., 12(9), pp2071-2074. 1973.

72. Quan, C., C.J. Tay, H.M. Shang and P.J. Bryanston-Cross, Contour measurement by fibre optic fringe projection and Fourier transform analysis, Optics Communications, 119, pp479-483. 1995.

73. Quan C., C.J. Tay, S.H. Wang, H.M. Shang and C.K. Chan, Study on

deformation of a microphone membrane using multiple-wavelength interferometry, Optics Communications, 197, pp279-287. 2001.

74. Quan, C., X.Y. He, C.F. Wang, C.J. Tay and H.M. Shang, Shape measurement of small objects with phase shifting, Optics Communications, 189, pp21-29. 2001.

75. Quan, C., C.J. Tay and Y.H. Huang, 3-D deformation measurement using fringe projection and digital image correlation, Optik, 115(4), pp164-168. 2004.

76. Quan, C., C.J. Tay and L. Chen, Fringe-density estimation by continuous wavelet transform, Appl. Opt., 44(12), pp2359-2365. 2005.

77. Quan, C., S.H. Wang, C.J. Tay and I. Reading, Study on the use of white light interferometry for multifiber-end surface profile measurement, Optical Engineering, 45, pp055603. 2006.

78. Recknagel and Notni, Analysis of white light interferograms using wavelet methods, Optics Communications, 148, pp122-128. 1997.

79. Roy, M., P. Svshn, L. Cherel and C.J.R. Sheppard, Geometric phase-shifting for low-coherence interference microscopy, Optics and Laser in Engineering, 37, pp631-641. 2002.

80. Ruiz, P.D., Y. Zhou, J.M. Huntley and R.D. Wildman, Depth-resolved whole-field displacement measurement using wavelength interferometry, J. Opt. A: Pure Appl. Opt., 6, pp679-683. 2004.

81. Salvi, J., J. Batlle and E. Mouaddib, A robust-coded pattern projection for dynamic 3D scene measurement, Pattern Recognition Letters, 19, pp1055-1065. 19988.

82. Sandoz, P., An algorithm for profilometry by white-light phase-shifting interferometry, J. of Modern Optics, 43(8), pp1545-1554. 1996.

83. Sandoz, P., Wavelet transform as a processing tool in white-light interferometry, Optics Letters, 22(14), pp1065-1067. 1997.

84. Sandoz, P., R. Devillers and A. Plata, Unambiguous profilometry by fringe-order identification in white-light phase-shifting interferometry, J. of Modern Optics, 44(3), pp519-534. 1997.

85. Schmitt, J.M., Optical coherence tomography (OCT): a review, IEEE J. of Selected Topics in Quantum Electronics, 5(4), pp1205-1215. 1999.

86. Scott, C.C., A. Luttge and K.A. Athanasiou, Development and validation of vertical scanning white light interferometry as a novel method for acquiring chondrocyte geometry, J. of Biomedical Materials Research Part A, 72A(1), pp83-90. 2004.

87. Shakher, C., R. Kumar, S.K. Singh and S.A. Kzami, Application of wavelet filtering for vibration analysis using digital speckle pattern interferometry, Opt. Eng., 41(1), pp176-180. 2002.

88. Sheppard C.J.R. and T. Wilson, The theory of the direct-view confocal microscope, Journal of Microscopy-Oxford, 124, pp107-117. 1981.

89. Shiou, F.-J. and M.-J. Chen, intermittent process measurement of a freeform surface profile with a circular triangulation laser probe on a machining centre, Int. J. Adv. Manuf. Technol., 21, pp365-376. 2003.

90. Shiou, F.-J. and J.-S. Gao, Effect of slice thickness on the profile accuracy of model maker rapid prototyping measured by a circular triangulation laser probe, Int. J. Adv. Manuf. Technol., 22, pp796-804. 2003.

91. Sirnivasan, V.H., C. Liu and M. Halioua, Automated phase measuring profilometry of 3D diffuse objects, Appl. Opt., 23, pp3105-3108. 1984.

92. Sitnik, R., M. Kujawinska and J. Woznicki, Digital fringe projection system for large volume 360-deg shape measurement, Opt. Eng., 41(2), pp443-449. 2002.

93. Sjödahl, M. and P. Synnergren, Measurement of shape by using projected random pattern and temporal digital speckle photography, Appl. Opt., 38, pp1990-1997. 1999.

94. Su, W.-H., Color-encoded fringe projection for 3D shape measurement, Optics Express, 15(20), pp13167-13181. 2007.

95. Suematsu, M. and M. Takeda, Wavelength-shift interferometry for distance measurement using the Fourier transform technique for fringe analysis, Appl. Opt., 30(28), pp4046-4055. 1991.

96. Takeda, M., H. Ina and S. Kobayashi, Fourier-transform method of fringe-pattern analysis for computer-based topography and interferometry, J. Opt. Soc. Am., 72(1), pp156-160. 1982.

97. Takeda, M and K. Mutoh, Fourier transform profilemetry for the automatic measurement of 3-D object shapes, 22(24), pp3977-3982. 1983.

98. Tay, C.J., C. Quan, Y. Fu and Y. Huang, Instantaneous velocity displacement and contour measurement by use of shadow moiré and temporal wavelet analysis, Appl. Opt., 43(21), pp4164-4171. 2004.

99. Tiziani, H.J. and H.M. Uhde, 3-dimensional analysis by a microlens-array confocal arrangement, Appl. Opt., 33, pp567-572. 1994.

100. Tiziani, H.J., B. Franze and P. Haible, Wavelength-shift speckle interferometry for absolute profilometry using a mode-hop free external cavity diode laser, Journal of Modern Optics, 44(8), pp1485-1496. 1997.

101. Vallance R.R., C.J. Morgan, S.M. Shreve and E.R. Marsh, Micro-tool characterization using scanning white light interferometry, J. Micromech. Microeng., 14, pp1234-1243. 2004.

102. Viswanathan, V.K., I. Liberman, G. Lawrence and B.D. Seery, Optical analysis of laser systems using interferometry, Appl. Opt., 19(11), pp1870-1873. 1980.

103. Walkins, L.R., S.M. Tan and T.H. Barnes, Determination of interferometer phase distributions by use of wavelets, Optics Letters, 24(13), pp905-907. 1999.

104. Wang, S.H., C. Quan, C.J. Tay, I. Reading and Z.P. Fang, Measurement of a fiber-end surface profile using phase-shifting laser interferometry, Appl. Opt., 43(1), pp49-56. 2004.

105. Watanabe, Y. and I. Yamaguchi, Digital transformation for separation measurement of thickness and refractive indices of layered objects by use of a wavelength-scanning heterodyne interference confocal microscope, Appl. Opt. 41(22), pp4497-4502. 2002.

106. Wilson, T., and C. Sheppard, Theory and practice of scanning optical microscopy [M], London: Academic Press INC (London) Ltd. 1984.

107. Windecker, R. and H. J. Tiziani, Optical roughness measurements using extended white-light interferometry, Optical Engineering, 38(6), pp1081-1087. 1999.

108. Windecher R., M. Fleischer and H. J. Tiziani, White-light interferometry with an extended zoom range, J. of Modern Optics, 46(7), pp1123-1135. 1999.

109. Wyant, J.C., Testing aspherics using two-wavelength holography, Appl. Opt., 10(9), pp2113-2118. 1971.

110. Wyant, J.C. and K. Creath, Advances in interferometric optical profiling, Int. J.

Mach. Tools Manufact., 32, pp5-10. 1992.

111. Yamamoto, A. and I. Yamaguchi, Profilometry of sloped plane surfaces by wavelength scanning interferometry, Optical Review, 9(3), pp112-121. 2002.

112. Zhong, J. and J. Weng, Spatial carrier-fringe pattern analysis by means of wavelet transform: wavelet transform profilometry, Appl. Opt., 43(26), pp4993-4998. 2004.

113. Zhou, J., Wavelet-aided spatial carrier fringe pattern analysis for 3-D shape measurement, Opt. Eng., 44(11), pp113602. 2005.

APPENDICES

Appendix A Imaging recording program by Microsoft Visual C++ 6.0

This program controls both image grabber card and PZT stage controller to work in cooperation. The following head files and resource code files are included in the program. "E816_DLL.h" and "PIPZT_Dlg.h" are for the PZT stage controller, while the other four included files are for image grabber.

```
#include "E816_DLL.h"
#include "PIPZT_Dlg.h"
#include "Bmp256.h"
#include "Imgcard.h"

#include "Bmp256.cpp"
#include "Imgcard.cpp"

//Initialize PZT positioning stage controller
void CIIView::OnPipztInitial()
{
      BOOL *PztSvo= new BOOL(true);
      double *PztPosition = new double(10);    //Initial PZT position 10 microns

      PiID = E816_InterfaceSetupDlg(NULL);          //Get the ID of PZT Controller

      E816_SVO(PiID, "A", PztSvo); //Computer-controlled close-loop ON

      E816_AVG(PiID, 32);    //Set number of average

      E816_MOV(PiID, "A", PztPosition); //To initial PZT position
}

//Initialize image grabber card
void CIIView::OnMilInitgray()
{
      if(Mcard.Init(false, "M_CCIR", GetSafeHwnd()))
```

```
        GetMainFrame()->NewFile("Grab image", Mcard.BufSizeX, Mcard.BufSizeY);
}

//Main function of scanning and capturing
void CIIView::OnMilPipzt()
{
    CFileDialog                          fd(false,NULL,NULL,OFN_OVERWRITEPROMPT,"Bmp
files(*.bmp)|*.bmp|All files (*.*)|*.*||",NULL );
    PIPZT_Dlg dlg;
    int n=0, digit0=10, w=bim.Getw(), h=bim.Geth();
    CString str;
    bool IsSave;
    valarray<char> fname;

    if(dlg.DoModal()==IDCANCEL) return;
    if(dlg.m_Increment*dlg.m_StepN/1000>240+dlg.m_BackDist)
    {
        if(MessageBox("Out of range", NULL, MB_OK|MB_ICONQUESTION)==IDOK)
return;
    }

    double *increment=new double(dlg.m_Increment/1000); //Scanning increment
    double *backdis=new double(dlg.m_BackDist*(-1)); //Backing distance

    if(MessageBox("Save    the    process    to    hard    disk",    NULL,
MB_YESNO|MB_ICONQUESTION)==IDYES)
    {
        IsSave=true;
        if(fd.DoModal()==IDCANCEL) return;
    }
    else IsSave=false;
    fname.resize(fd.GetPathName().GetLength()+23, char(0));
    while(digit0<=dlg.m_StepN) digit0*=10;
    MessageBox("Press OK to begin.\n\nPress Esc or click the screen to stop.");

    if (!E816_MVR(PiID, "A", backdis)) return; //Go to starting position
    if(dlg.m_TimInterval>0) Sleep(dlg.m_TimInterval); //Settling timing

    while(n<=dlg.m_StepN && !StopFunction()) // If step is N, N+1 frames are recorded.
    {
        MdigGrab(Mcard.Dig, Mcard.Img);    //Capture image
        if(IsSave)
        {
            str.Format("%d", digit0+n);
```

```
                str=fd.GetPathName()+str.Right(str.GetLength()-1)+".bmp";
                strcpy(&fname[0], LPCTSTR(str));
                MbufExport(&fname[0], M_BMP, Mcard.Img);    //Save image
            }
            if(!E816_MVR(PiID, "A", increment)) return;     //Scan one step
            if(dlg.m_TimInterval>0) Sleep(dlg.m_TimInterval); //Settling timing
            n++;
        }

        double *iniP=new double(10);
        E816_MOV(PiID, "A", iniP);          //Back to initial position
        if(!Mcard.IsRGB) MbufGet(Mcard.Img, bim.Getv());
        MessageBox("Process complete.");
}

//Close PZT controller
void CIIView::OnPipztClose()
{
        BOOL *PztSvo = new BOOL(FALSE);

        E816_SVO(PiID, "A", PztSvo); //Off computer-controlled close-loop
        E816_CloseConnection(PiID);    //Close the connection to PZT controller
}

//Close image grabber card
void CIIView::OnMilClose()
{
        Mcard.Close();
}
```

Appendix B Subroutine of gray fringe processing

This subroutine is to retrieve the surface height of a test object from the white light interferometric fringe patterns, which are recorded as gray images. The calculated 2-D array of the surface heights is stored in the file 'gHarray.asc' in ASCII codes.

```
% This function is to get the profile of the surface with continuous
% wavelet transform and Get the peak with 3-point Gaussian fitting

% CWT_surface_phase(fullpath,startN,endN,steplength,width,height,index,x,y)

% fullpath:        the full file path;
% startN:          the first image number;
% endN:            the last image number;
% steplength:      increment of the vertical scanning;
% width:           the width of the image;
% height:          the height of the image.
% index;           index==0 means using one frequency to scan the signal; index==1
%                  means using more than one frequency to scan the signal.
% (x, y):          the point to be used to determine the frequency of the signal.

function CWT_surface_phase(fullpath,startN,endN,steplength,width,height,index,x,y)

% Load the image from the hard disk
for k=1:(endN-startN+1)
    clear imageN;     %clear the memory
    imageN=int2str(k+startN-1);
    if k+startN-1<10
        filename=strcat(fullpath,'T0000',imageN,'.bmp');
    elseif k+startN-1<100
        filename=strcat(fullpath,'T000',imageN,'.bmp');
    elseif k+startN-1<1000
        filename=strcat(fullpath,'T00',imageN,'.bmp');
    elseif k+startN-1<10000
        filename=strcat(fullpath,'T0',imageN,'.bmp');
    else
        filename=strcat(fullpath,'T',imageN,'.bmp');
    end

    pic(k,:,:)=imread(filename);          %Read the image
```

```
end

% to find the scaling corresponding to the interferograms
for k=1:(endN-startN+1)
        value(k)=double(pic(k,y,x));
end

% to implement data extension
interdata(1:200)=value(1);
interdata(endN-startN+2+200:endN-startN+1+400)=value(endN-startN+1);
interdata(201:endN-startN+1+200)=value;

% to carry out Wavelet transform
wavedata=cwt(interdata,1:0.1:30,'cmor2-1');

% to get the valuable transformed data by data truncation
for k=1:(30-1)/0.1+1
        vdata(k,:)=wavedata(k,201:endN-startN+1+200);
end

% to get the modulus of the transformed data
mdata=abs(vdata);

% to find the scaling for maximum corrrelation
[temmax,temindex]=max(mdata);
[mmax,mp]=max(temmax);                          % mp is the position of maximum of the signal
mscale=temindex(mp)
wavleng=2*steplength*(1+(mscale-1)*0.1)      % the mean wavelength of the light source

%To find the peak of the signal (surface height)
for x=1:width
        for y=1:height
                for k=1:(endN-startN+1)
                        value(k)=double(pic(k,y,x));
                end

                % to extend the data vector to eliminate the border effect of wavelet transform
                clear interdata        % interdata is the extended signal for wavelet transform
                interdata(1:200)=value(1);
                interdata(endN-startN+2+200:endN-startN+1+400)=value(endN-startN+1);
                interdata(201:endN-startN+1+200)=value;

                % to carry out wavelet transform
                if index==0      % using the same frequency to scan the signal
```

```
            scal=1+(mscale-1)*0.1;
            wavedata=cwt(interdata,scal,'cmor2-1');
            wtdata=abs(wavedata);
            vdata=wavedata(201:endN-startN+1+200);
            mdata=abs(vdata);
            [tem pp]=max(mdata);
        elseif index==1
            scal=(mscale-1)*0.1-5:0.1:(mscale-1)*0.1+5;
            wavedata=cwt(interdata,scal,'cmor2-1');

            % to find the frequency of interested
            wtdata=abs(wavedata(:,201:endN-startN+1+200));
            [temmax,temindex]=max(wtdata);
            [mmax,mp]=max(temmax);
            ii=temindex(mp);

            % to get the valuable transformed data
            vdata=wavedata(ii,201:endN-startN+1+200);
            % to get the modulus of the transformed data
            mdata=abs(vdata);
           % to get the peak position of 'mdata'
           [tem pp]=max(mdata);                    % pp is the peak of the signa

           mmscale=temindex(mp);
          wavleng=2*steplength*(1+(mscale-1)*0.1-5+(mmscale-1)*0.1);
       else
           pp=1;
       end

        % write the peak pisition into the peak position matrix 'peakp'
        peakp(y,x)=pp;
        % to get the phase of the peak
        ph(y,x)=atan2(imag(vdata(pp)),real(vdata(pp)));
        % to get the peak position using phase information
        gpeakp(y,x)=peakp(y,x)*steplength-ph(y,x)*wavleng/4/pi;
    end
end

gHarray=gpeakp/1000;
save gHarray.asc gHarray -ASCII;
```

Appendix C Subroutine of color fringe processing

This subroutine is to retrieve the surface height of a test object from the white light interferometric fringe patterns, which are recorded as color images. The calculated 2-D array of the surface heights is stored in the file 'hRGB_cwt.asc' in ASCII codes. This subroutine is written for the simulation described in Table 4.2. Hence, for simplicity a single scaling parameter *a* is used to implement CWT in the analysis of simulated fringe patterns.

```
% This function is to get the profile of the surface with phase cross
% method based on CWT (Complex Morlet)

% PhRGBFFT(fullpath,startN,endN,steplength,width,height,s_size)

% fullpath:       the full file path;
% startN:         the first image number;
% endN:           the last image number;
% steplength:     the scanning step length;
% width:          the width of the image;
% height:         the height of the image.
% s_size:         the sampling size.

Function PhRGBCWT(fullpath,startN,endN,steplength,width,height, s_size)

% Load the image from the hard disk
for k=1:(endN-startN+1)
    clear imageN;    %clear the memory
    imageN=int2str(k+startN-1);
    if k+startN-1<10
        filenameR=strcat(fullpath,'\R\T0000',imageN,'.bmp');
        filenameG=strcat(fullpath,'\G\T0000',imageN,'.bmp');
        filenameB=strcat(fullpath,'\B\T0000',imageN,'.bmp');
    elseif k+startN-1<100
        filenameR=strcat(fullpath,'\R\T000',imageN,'.bmp');
        filenameG=strcat(fullpath,'\G\T000',imageN,'.bmp');
        filenameB=strcat(fullpath,'\B\T000',imageN,'.bmp');
    elseif k+startN-1<1000
        filenameR=strcat(fullpath,'\R\T00',imageN,'.bmp');
```

```
            filenameG=strcat(fullpath,'\G\T00',imageN,'.bmp');
            filenameB=strcat(fullpath,'\B\T00',imageN,'.bmp');
        elseif k+startN-1<10000
            filenameR=strcat(fullpath,'\R\T0',imageN,'.bmp');
            filenameG=strcat(fullpath,'\G\T0',imageN,'.bmp');
            filenameB=strcat(fullpath,'\B\T0',imageN,'.bmp');
        else
            filenameR=strcat(fullpath,'\R\T',imageN,'.bmp');
            filenameG=strcat(fullpath,'\G\T',imageN,'.bmp');
            filenameB=strcat(fullpath,'\B\T',imageN,'.bmp');
        end
        %Read the image
        picR(k,:,:)=imread(filenameR);
        picG(k,:,:)=imread(filenameG);
        picB(k,:,:)=imread(filenameB);
end

% Calculate height based on RGB channels using CWT
for x=1:width
    for y=1:height
        [mm II]=max(picR(:,y,x));
        IR=double(picR(:,y,x));
        IG=double(picG(:,y,x));
        IB=double(picB(:,y,x));

        % calculate the phase of R component
        CR=cwt(IR,15.5,'cmor2-1');
        CR=CR(II-s_size/2:II+s_size/2-1);
        for k=1:s_size
            phR(k)=atan2(imag(CR(k)),real(CR(k)));
        end

        % calculate the phase of G component
        CG=cwt(IG,13.5,'cmor2-1');
        CG=CG(II-s_size/2:II+s_size/2-1);
        for k=1:s_size
            phG(k)=atan2(imag(CG(k)),real(CG(k)));
        end

        % calculate the phase of B component
        CB=cwt(IB,12,'cmor2-1');
        CB=CB(II-s_size/2:II+s_size/2-1);
        for k=1:s_size
            phB(k)=atan2(imag(CB(k)),real(CB(k)));
```

```
end

% To get three points for line fitting
[mm I]=min(abs(phR-phG));

% R component
if abs(phR(I)-phR(I-1))>pi
    yR=phR(I:I+2);
    xR=steplength*(I:I+2);
elseif abs(phR(I)-phR(I+1))>pi
    yR=phR(I-2:I);
    xR=steplength*(I-2:I);
else
    yR=phR(I-1:I+1);
    xR=steplength*(I-1:I+1);
end
[aR bR]=linefit(xR,yR);                % fit the line y=aR*x+bR

% G component
if abs(phG(I)-phG(I-1))>pi
    yG=phG(I:I+2);
    xG=steplength*(I:I+2);
elseif abs(phG(I)-phG(I+1))>pi
    yG=phG(I-2:I);
    xG=steplength*(I-2:I);
else
    yG=phG(I-1:I+1);
    xG=steplength*(I-1:I+1);
end
[aG bG]=linefit(xG,yG);                 % fit the line y=aG*x+bG

% B component
if abs(phB(I)-phB(I-1))>pi
    yB=phB(I:I+2);
    xB=steplength*(I:I+2);
elseif abs(phB(I)-phB(I+1))>pi
    yB=phB(I-2:I);
    xB=steplength*(I-2:I);
else
    yB=phB(I-1:I+1);
    xB=steplength*(I-1:I+1);
end
[aB bB]=linefit(xB,yB);                % fit the line y=aB*x+bB
```

```
        % To calculate the height of point (x,y)
        hRGB(x,y)=steplength*II-(aR*bR+aG*bG+aB*bB)/(aR*aR+aG*aG+aB*aB);
    end
end

save hRGB_cwt.asc hRGB -ASCII;
meshz(hRGB)
```

Appendix D Interferometry objectives

Table A.1 Key parameters of interferometry objectives

Objective model	N.A.	W.D. (mm)	Focal length (mm)	Physical depth of focus (µm)
CF Plan EPI TI 5×	0.13	9.3	40	48.5
CF Plan EPI DI 10×	0.3	7.4	19.8	3.03
CF Plan EPI DI 20×	0.4	4.7	9.96	1.71

N.A. – Numerical Aperture

W.D. – Working Distance

Appendix E List of publications

1. M. Li, C. Quan and C.J. Tay, Continuous wavelet transform for micro-component profile measurement using vertical scanning interferometry, Optics & Laser Technology, 40, pp920-929. 2008.

2. C.J. Tay, C. Quan and M. Li, Investigation of a dual-layer structure by the use of vertical scanning interferometry, Optics and Lasers in Engineering, 45, pp907-913. 2007.

3. C. Quan, C.J. Tay and M. Li, Inspection of a micro-cantilever's opened and concealed profile using integrated vertical scanning interferometry, Optics Communications, 265, pp359-365. 2006.

4. M. Li, C. Quan, C.J. Tay, I. Reading and S.H. Wang, Measurement of transparent coating thickness by the use of white light interferometry, Proc. of SPIE, vol. 5852, pp401-406. 2004.

5. M. Li, C. Quan and C.J. Tay, White light interferometry for surface quality inspection of a micro-cantilever, Presented in International Congress on Experimental Mechanics 2005, New Delhi, India. 12th-14th 2005.